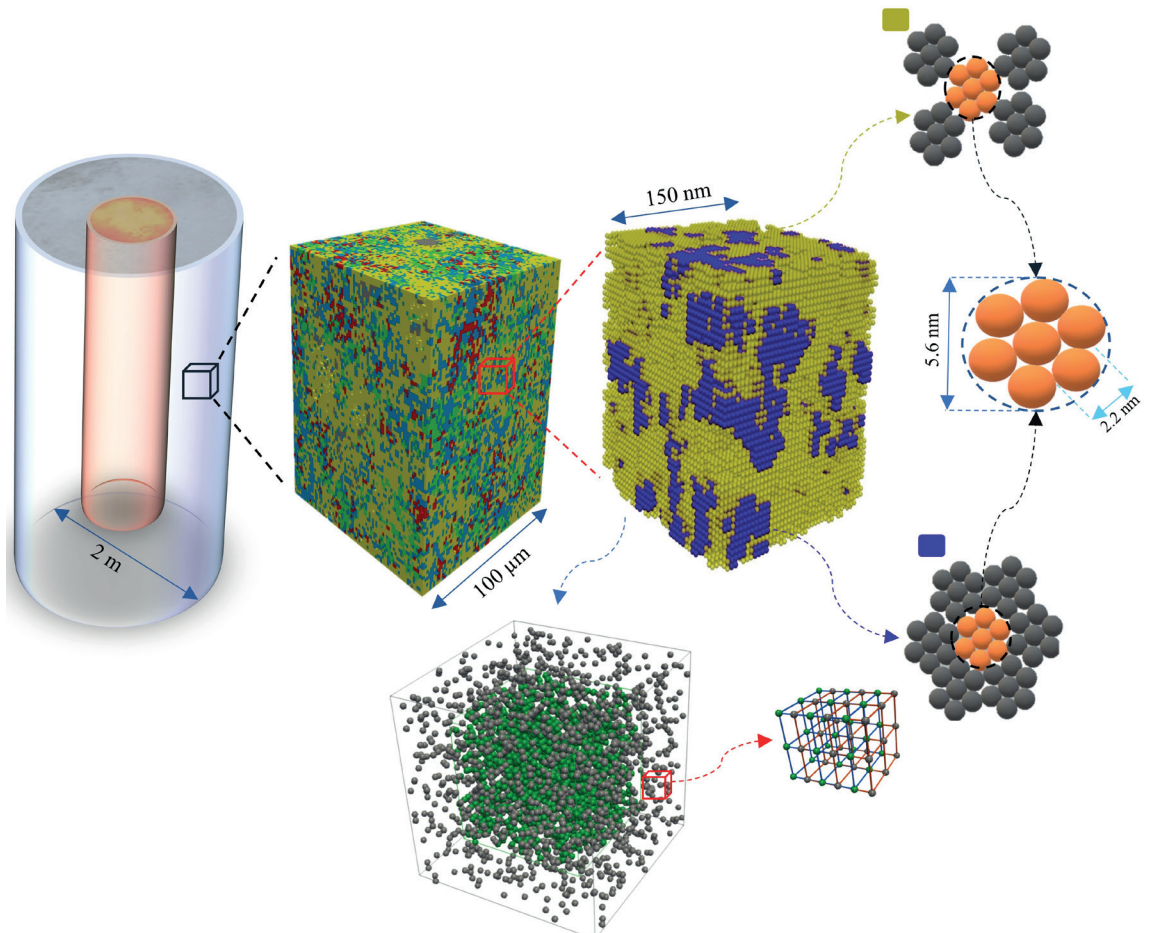


# A Multiscale Approach to Model Thermo-Hydro-Mechanical Behaviour of nonreinforced Concrete

Saeid Babaei



Promotoren **prof. dr. Bart Craeye** | **prof. dr. Gunther Steenackers**

Proefschrift voorgedragen tot het behalen van de graad van doctor in de toegepaste ingenieurswetenschappen  
Faculteit Toegepaste Ingenieurswetenschappen | Antwerpen, 2021



Faculty of Applied Engineering  
Bouwkunde

# A Multiscale Approach to Model Thermo- Hydro-Mechanical Behaviour of non- reinforced Concrete

Thesis submitted in fulfilment of the requirements for the degree of  
Doctor in Applied Engineering (Doctor in Toegepaste Ingenieurswetenschappen)  
at University of Antwerp

**Saeid Babaei**

Supervisors  
Prof. Dr. Bart Craeye  
Prof. Dr. Gunther Steenackers

Antwerp 2021



Jury

**Chairman**

Prof. Dr. Wim Van den bergh, University of Antwerp, EMIB research group

**Supervisors**

Prof. Dr. Bart Craeye, University of Antwerp, EMIB research group

Prof. Dr. Gunther Steenackers, University of Antwerp, Op3Mech research group

**Members**

Prof. Dr. ir. Geert De Schutter, Ghent University, Department of Structural Engineering and Building Materials

Prof. Dr. G. (Guang) Ye, TU Delft, Faculty of Civil Engineering and Geosciences

Prof. Dr. Farid Benboudjema, Ecole normale supérieure Paris-Saclay

Dr. Suresh Seetharam, Belgian Nuclear Research Centre (SCK•CEN)

**Secretary**

Prof. Dr. Ing. Johan Blom, University of Antwerp, EMIB Research Group

**Contact**

Saeid Babaei

University of Antwerp

Faculty of Applied Engineering

© 2021 Saeid Babaei

All rights reserved.

No part of this book may be reproduced in any form, by print, photoprint, microfilm or any other means, without permission from the author.

Out beyond ideas of wrongdoing and  
rightdoing, there is a field. I'll meet you  
there. Rumi

## English

Cementitious materials are the main pillar of modern construction and urbanization. With their endless practical applications and diversity of utilization from small village houses to skyscrapers, power plants and even nuclear waste disposal structures, they can be seen everywhere. The main driver for this study was to investigate the thermo-hydro-mechanical (THM) behaviour of cementitious engineered barriers, in particular, the barrier for high level nuclear waste containers considered in the Belgian deep geological disposal program.

The principal objective of this study is to investigate the THM behavior of concrete within a multiscale framework. More importantly, to be able to predict fundamental properties of concrete based on its composition to enable optimization of its design. This, however, cannot be achieved without an in-depth study of phenomena and parameters, which are affecting the macro-behavior of the concrete. Since such barriers are exposed to thermal loading emanating from decay of the high level waste, a range of coupled processes usually referred to as THM processes are involved in their performance. Therefore, this thesis proposes a stepwise, multi-component and multiscale framework to model THM behavior of cementitious materials starting from microstructural modelling by representing microstructure of the material based on its chemical composition and reaction condition (curing, age, temperature, etc.). This modelling tool is then coupled with an algorithmic scheme adapted to convert such microstructure to a representative pore network and simulate transport properties. Regarding the mechanical and thermal properties, including elastic modulus, coefficient of thermal expansion and heat conduction

coefficient a micromechanical scheme has been implemented by means of numerical homogenization using Cast3m, where the cement microstructure is once again the main input parameter. Subsequent to the development of such hydro-micromechanical framework (pore network and micromechanical modelling), drying shrinkage was the first aspect to be addressed as an important and a potentially detrimental process for long-term performance of concrete structures. Hereby, the drying shrinkage of cementitious materials is computed using a novel and multi-mechanism drying shrinkage model. This model takes into account three individual mechanisms responsible for drying shrinkage of cementitious materials: capillary force, surface free energy and disjoining pressure. In addition, a detailed stress analysis on microstructural level is carried out, which highlights the importance of such studies.

Finally, a multiscale and microstructure-informed THM simulation of an engineered barrier for high level nuclear waste container is carried out, where the material parameters are derived using the aforementioned framework (hydro-mechanical). The main objective of this application is to identify spatial regions of the engineered barrier that are prone to crack formation and propagation due to evolving thermal load and its consequences to hydro-mechanical behaviour of the barrier.

## Dutch

Cementgebonden materialen zijn de belangrijkste pijler van moderne bouw en verstedelijking. Met hun eindeloze praktische toepassingen en diversiteit in gebruik, van kleine dorpshuizen tot wolkenkrabbers, energiecentrales en zelfs structuren voor de verwijdering van nucleair afval, zijn ze overal te zien. De belangrijkste drijfveer voor deze studie was het onderzoeken van het thermo-hydrmechanische (THM) gedrag van cementgebonden barrières, in het bijzonder de barrière voor containers met hoog radioactief afval die in het Belgische programma voor diepe geologische berging worden overwogen.

Het hoofddoel van deze studie is om het THM-gedrag van beton binnen een multischaalkader te onderzoeken. Wat nog belangrijker is, om de fundamentele eigenschappen van beton te kunnen voorspellen op basis van de samenstelling, zodat het ontwerp kan worden geoptimaliseerd. Dit kan echter niet worden bereikt zonder een diepgaande studie van verschijnselen en parameters die het macrogedrag van het beton beïnvloeden. Aangezien dergelijke barrières worden blootgesteld aan thermische belasting die voortkomt uit het verval van het hoogactief afval, zijn een reeks gekoppelde processen die gewoonlijk THM-processen worden genoemd, bij hun prestaties betrokken. Daarom stelt dit proefschrift een stapsgewijs, meercomponenten- en multischaalkader voor om het THM-gedrag van cementachtige materialen te modelleren, uitgaande van microstructurele modellering door de microstructuur van het materiaal weer te geven op basis van zijn chemische samenstelling en reactieconditie (uitharding, leeftijd, temperatuur, enz.). Deze modelleringstool wordt vervolgens gekoppeld aan een algoritmisch schema dat is aangepast om een dergelijke microstructuur om te zetten in een representatief porienetwerk en transporteigenschappen te simuleren. Met betrekking tot de mechanische en thermische eigenschappen, waaronder elastische modulus, thermische uitzettingscoëfficiënt en warmtegeleidingscoëfficiënt, is een micromechanisch schema geïmplementeerd door middel van numerieke homogenisatie met behulp van Cast3m, waarbij de cementmicrostructuur opnieuw de belangrijkste invoerparameter is. Na de ontwikkeling van een dergelijk hydromicromechanisch raamwerk (porienetwerk en micromechanische modellering), was krimp tijdens drogen het eerste aspect dat moest worden aangepakt als een belangrijk en potentieel schadelijk proces voor de prestaties van betonconstructies op lange termijn. Hierbij wordt de droogkrimp van cementachtige materialen berekend met behulp van een nieuw

en multi-mechanisme droogkrimmodel. Dit model houdt rekening met drie individuele mechanismen die verantwoordelijk zijn voor het drogen van krimp van cementachtige materialen: capillaire kracht, vrije energie aan het oppervlak en ontkoppelde druk. Daarnaast wordt een gedetailleerde stressanalyse op microstructureel niveau uitgevoerd, die het belang van dergelijke studies onderstreept.

Ten slotte wordt een multischaal en microstructuur-geïnformeerde THM-simulatie van een technische barrière voor een container voor hoogactief kernafval uitgevoerd, waarbij de materiaalparameters worden afgeleid met behulp van het bovengenoemde raamwerk (hydromechanisch). Het hoofddoel van deze toepassing is om ruimtelijke gebieden van de gebouwde barrière te identificeren die vatbaar zijn voor scheurvorming en voortplanting als gevolg van de zich ontwikkelende thermische belasting en de gevolgen daarvan voor het hydromechanische gedrag van de barrière.

# Acknowledgements

---

The research presented in this doctoral thesis has been carried out from 2017 to 2021 at the Belgian nuclear research centre (SCK-CEN) and Faculty of Applied Engineering at University of Antwerp, Belgium. It was made possible through the financial support from of the Belgian nuclear research centre (SCK-CEN) which is gratefully acknowledged.

I would like to thank my family. My parents, and my siblings for all the sacrifices they made in life for me and all the valuable lessons they thought me. Maman joon, Baba joon, Dash Mohamad, Dash Reza, Abjee Somayeh.

Also, my friends from home, Peyman, Hamid, Reza, Ghasem, Meysam, and Amir Fereydoon.

There were two Saeids involved in this journey, the one that started it and the one that is writing these last few words. The list of people who helped me throughout this journey and I should thank is extended. To mention a few...

I wish to thank, first my mentors and my supervisors. Suresh who was always available and willing to spend time helping me with conceptualizing the work and sharing insights and teaching me the unteachable during our countless discussions. I wish to thank him for his kind care and enthusiasm for knowledge. Arnaud who helped me with the arrangement of the thesis.

Bart with being a great and sincere human being who's also charismatic, pragmatic and thoughtful saved my work from pitfalls and helped me to structure the work into this thesis, not only with the PhD but also with personal matters he was always available and helpful. I wish to thank him for his great supervision and support all along the way, working with him was simply the best part of this journey and I have great respect for him.

Jury members including, Prof. Farid Benboudjema who accepted me as a visitor to his lab and gave me a once in a lifetime chance to learn the professionalism, and originality as he is rightfully the one to learn these skills from. I wish to thank him for this chance, his patient help and supervision which resulted in two chapters of this thesis. I also would like to thank Prof. Túlio Honório for his help and advice during my visit at Ecole normale supérieure Paris-Saclay.

Other Jury members, Prof. Geert De Schutte and Prof. Dr. G. (Guang) Ye despite their busy agenda kindly accepted to review my work and helped me improve it by their constructive comments and discussions.

I also would like to thank SCK-CEN Academy first for awarding me with scholarship and secondly for their persistent support and help, I would like to express my gratitude specially to Dr. Michèle Coeck the head of the Academy who has been always kindly helpful and supportive from the very first day when I did not have a place to seat in the building to the very last step of helping in holding the public defence. I have learnt a lot from Academy's programs.

I also would like to thank Dr. Christophe Bruggeman and Dr. Diederik Jacques the head of EGA and W&D expert groups in SCK-CEN for their kind support and help during my PhD project. I also would like to thank other researchers and colleagues in SCK-CEN who helped me. To mention a few, Tri Quoc Phung, Janez, Luarent, Ghabriel, Anna, Yulia, Claudia, Daniele, Giada, Domenico, Harsh, Alberto,... and the list goes on. So, thank you Boeretangers.

It was not all in the office that I made friends, I made two of my best friends forever outside the office, Dr. Sumit Srivastava and Dr. Yin Chao who certainly will have to pay for the two Drs they received here. They helped me to grow, learn and see things differently. During our countless discussions and also trips they thought me things which would otherwise take lives to learn (well it took me four years). Chao also met Dr. Dan Chen in Belgium and they engaged later on in China, she also became part of the team.

And finally, Rosa, there are no words to describe how thankful I am to have you by my side. You were with me during my ups and down and helped me go through this journey. I have enjoyed every moment of being with you and you should know that I could not have done it without you Tesorino. Signora Dora also played an important role with preparing the most delicious meals that fade the hardship away.

Antwerp, March 2021

Saeid Babaei

# List of Symbols

---

## Chapter 2

$\beta$	Shape factor of Weibull distribution function (-)
$\eta$	Scale parameter of Weibull distribution function (-)
$\gamma$	The location parameter of Weibull distribution function (-)
$\varphi_{gel}$	C-S-H gel porosity (-)
$\varphi_{HD}$	High density (HD) C-S-H porosity (-)
$V_{HD}$	Volume fraction of HD C-S-H (-)
$\varphi_{LD}$	Low density (LD) C-S-H porosity (-)
$V_{LD}$	Volume fraction of LD C-S-H (-)
$V_{gel}$	Volume fraction of C-S-H gel pores (-)
$V_{CSH}$	Volume fraction of C-S-H (-)
$R_{throat}$	Radius of the throat (m)
$R_{np}$	Radius of neighbouring pore (m)
$R_a$	Radius of element 'a' (either pore or throat) (m)
$L_{throat}$	Length of the throat (m)
$\alpha$	Scale factor (-)
$\omega$	Scale factor (-)
$P_c$	Capillary pressure (Pa)
$\sigma$	The surface tension (N/m)
$\theta$	The contact angle (°)
$r$	The pore radius (m)

$RH$	Relative humidity (-)
$t$	The thickness of adsorbed water (m)
$R_v$	The gas constant of water vapour (J/kg/K)
$T$	The temperature (K)
$h_m$	Local relative humidity (-)
$S_l$	Degree of saturation (-)

### Chapter 3

$w_d$	Water content (weight) (kg)
$K_b$	The effective bulk modulus (Pa)
$K_s$	The effective bulk modulus of solid skeleton (Pa)
$\varphi_c$	The capillary porosity (-)
$h$	Relative humidity (-)
$\varepsilon_{v,r}$	Volumetric drying shrinkage strain ( $\text{m}^3/\text{m}^3$ )
$\varepsilon_{vc}$	Volumetric drying shrinkage strain due to capillary force ( $\text{m}^3/\text{m}^3$ )
$\varepsilon_{vs}$	Volumetric drying shrinkage strain due to surface free energy ( $\text{m}^3/\text{m}^3$ )
$\varepsilon_{ds}$	Volumetric drying shrinkage strain due to disjoining pressure ( $\text{m}^3/\text{m}^3$ )
$u_a$	Pore air pressure (Pa)
$u_w$	Pore water pressure (Pa)
$\chi$	The Bishop's effective stress parameter (-)
$S_l$	Degree of saturation (-)
$R$	The gas constant (J/K·mol)
$M$	The molar mass of water (g/mol)
$v_w$	The specific volume of water ( $\text{m}^3/\text{kg}$ )
$\sigma$	The surface area of emptied pores per volume of porous material ( $\text{m}^2/\text{m}^3$ )
$\gamma$	The surface free energy of solid (N/m)

$\gamma_0$	The surface tension at $h_0$ (N/m)
$h_0$	Reference relative humidity (-)
$\theta$	The volumetric water content of the surface adsorbed water (-)
$\beta'$	The coefficient of compressibility under sustained stress (Pa <sup>-1</sup> )
$k$	Constant of proportionality (-)
$V_s$	The volume of the adsorbent (m <sup>3</sup> )
$V_p$	The volume of cement paste (m <sup>3</sup> )
$\varphi_t$	The total porosity of the paste (-)
$\varepsilon_{v,irr}$	Irreversible drying shrinkage (m <sup>3</sup> / m <sup>3</sup> )
$V_{LD\ C-S-H}$	Volume fraction of LD C-S-H (-)
$V_{C-S-H}$	Volume fraction of C-S-H (-)

#### Chapter 4

$Q$	The flow rate (m <sup>3</sup> /s)
$A$	The network cross section area (m <sup>2</sup> )
$L$	Length of the network (m)
$\mu$	The dynamic viscosity (Pa.s)
$\Delta P$	The pressure difference across the two opposing sides (Pa)
$K_l$	The permeability of the network (m <sup>2</sup> )
$R_c$	Hydraulic resistance (m <sup>3</sup> / Pa.s)
$q_c$	The flow rate (m <sup>3</sup> /s)
$I_p$	The specific polar moment of cross-sectional inertia (m <sup>4</sup> )
$R_{i,j}$	Hydraulic resistance between $i$ and $j$ (m <sup>3</sup> / Pa.s)

#### Chapter 5

$\sigma$	Cauchy's stress tensor
----------	------------------------

$\mathbf{D}^{\text{eff}}$	Effective stiffness tensor
$\boldsymbol{\epsilon}_{el}$	Elastic small strain tensor
$\boldsymbol{\epsilon}_{\text{Tot}}$	Total strain tensor
$\alpha$	Coefficient of thermal expansion (CTE) ( $1/^{\circ}\text{C}$ )
$T$	Temperature (K)
$\mathbf{I}$	The identity matrix
$V$	Volume ( $\text{m}^3$ )

## Chapter 6

$Q$	Heat flux ( $\text{W}/\text{m}^2$ )
$q_h$	Heat source (W)
$\rho$	Density ( $\text{kg}/\text{m}^3$ )
$C_t$	Specific heat capacity ( $\text{kJ}/(\text{kg}\cdot^{\circ}\text{C})$ )
$\lambda_t$	The thermal conductivity ( $\text{W}/(\text{m}\cdot^{\circ}\text{C})$ )
$T$	Temperature (K)
$T_{env}$	Ambient temperature (K)
$h_t$	Heat convection factor ( $\text{W}/(\text{m}\cdot^{\circ}\text{C})$ )
$\epsilon_{th}$	Thermal expansion strain ( $\text{m}^3/\text{m}^3$ )
$k_{th}$	Thermal expansion coefficient ( $1/^{\circ}\text{C}$ )
$m$	mass (kg)
$S_x$	The degree of saturation (-)
$D$	The effective diffusivity ( $\text{m}^2/\text{s}$ )
$p_c$	Capillary pressure (Pa)
$a_{mu}$	Van Genuchten's model parameter (-)
$b_{mu}$	Van Genuchten's model parameter (-)
$\mu_l$	Viscosity of the water ( $\text{m}^2/\text{s}$ )

<b>D</b>	Material's stiffness tensor
$\varepsilon_T$	Total strain ( $m^3/m^3$ )
$\varepsilon_{sh}$	Shrinkage strain ( $m^3/m^3$ )
$k_{sh}$	Shrinkage coefficient (-)
$\varphi_c$	Creep coefficient (-)
$\varphi_{bc}$	basic creep coefficient (-)
$\varphi_{dc}$	drying creep coefficient (-)
$\varphi_{bc0}$	Specific basic creep (-)
$\varphi_{th}$	Thermal creep coefficient (-)
$\tilde{\varepsilon}$	Equivalent strain in Mazars damage model (-)
k	The threshold of damage growth (Pa)
$f_t$	The material in uniaxial tensile strength (Pa)
$E_0$	Elastic modulus (Pa)
$d_t$	Damage variables in tension (-)
$d_c$	Damage variables in compression (-)

# Contents

---

Abstract	5
Acknowledgment	9
List of symbols	11
1 Introduction and outline.....	19
1.1 Background.....	19
1.2 Aims of thesis .....	23
1.3 Scope and limitations.....	24
1.4 Outline of thesis.....	25
2 A Multiscale Framework to Estimate Water Sorption Isotherms for OPC-based Materials .....	30
2.1 Introduction .....	30
2.1 Multiscale framework.....	34
2.1.1 Particle packing model: nm scale .....	36
2.2 Microstructural cement hydration kinetics model: $\mu\text{m}$ scale.....	39
2.3 Missing pore size distribution: nm to $\mu\text{m}$ scale .....	41
2.4 Pore network model.....	41
2.5 Validation .....	51
2.5.1 Influence of capillary pores .....	56
2.5.2 Wsi predictions .....	58
2.6 Conclusions .....	62
3 An Analytical Framework for Estimating Drying Shrinkage Strain of OPC Based Hardened Cement Paste.....	65
3.1 Introduction .....	65
3.2 Analytical framework.....	69
3.2.1 Desorption isotherm from a multiscale approach .....	72
3.2.2 Effective bulk modulus from analytical homogenization .....	72
3.2.3 Drying shrinkage .....	75

3.2.4	Shrinkage strain due to capillary forces ( $0.45 < h < 1$ ).....	77
3.2.5	Shrinkage strain due to solid surface tension ( $0 < h < 1$ ) .....	78
3.2.6	Shrinkage strain due to disjoining pressure ( $0 < h < 0.45$ ).....	79
3.2.7	Other models for drying shrinkage strain .....	79
3.3	Validation .....	80
3.3.1	Cement hydration kinetics .....	84
3.3.2	Water desorption isotherms .....	87
3.3.3	Effective bulk modulus.....	88
3.3.4	Drying shrinkage strain .....	90
3.4	Conclusions .....	100
3.5	Appendix A .....	102
3.5.1	Equivalent pore pressure concept – Coussy .....	102
3.5.2	Effective bulk modulus concept – Vlahinic et al.....	102
4	Permeability of hardened cement paste using the pore network model.....	104
4.1	Introduction .....	104
4.2	Multiscale pore network .....	107
4.3	Permeability calculations.....	109
4.3.1	General principle .....	109
4.3.2	Intrinsic permeability.....	110
4.3.3	Unsaturated permeability.....	113
4.4	Results and validation.....	115
4.4.1	Intrinsic permeability.....	119
4.4.2	Unsaturated permeability.....	125
4.5	Conclusions .....	127
5	Micromechanical analysis of mechanical and hydro-mechanical properties .....	129
5.1	Introduction .....	129
5.2	Methodology.....	130
5.2.1	Mechanical properties of hardened cement paste .....	130
5.2.2	Coefficient of thermal expansion.....	133
5.2.3	Drying shrinkage strain .....	133
5.3	Validation and discussion .....	136
5.3.1	Cement Composition .....	136

5.3.2	Mechanical properties.....	137
5.3.3	Coefficient of thermal expansion.....	139
5.3.4	Drying shrinkage .....	141
5.4	Conclusions .....	153
6	A Multiscale Approach to Model Thermo-Hydro-Mechanical Behaviour of non-reinforced Concrete .....	154
6.1	Introduction .....	154
6.2	Description of the simulation .....	157
6.2.1	Geometry .....	157
6.2.2	Initial conditions.....	158
6.2.3	Boundary conditions.....	158
6.2.4	THM governing equations.....	159
6.2.5	Properties.....	170
6.3	Results and discussion .....	175
6.3.1	Thermal loading and drying shrinkage – temperature field.....	175
6.3.2	Thermal loading and drying shrinkage – moisture field.....	176
6.3.3	Thermal loading and drying shrinkage – elastic behaviour.....	179
6.3.4	Thermal loading and drying shrinkage, including creep and damage	182
6.3.5	Thermal stresses vs drying shrinkage stresses – elastic interpolation	186
6.4	Conclusions .....	187
7	Conclusions and future perspectives .....	191
7.1	General conclusions.....	191
7.2	Future perspectives .....	194
8	References .....	199

# 1 Introduction and outline

---

## 1.1 Background

# Chapter 1

Cementitious materials are the main pillar of modern construction and urbanization. With their endless practical applications and diversity of utilization from small village houses to skyscrapers, power plants and even nuclear waste disposal structures, which is where the idea of this thesis initiated, cementitious materials can be seen everywhere.

The integrity of non-reinforced concrete structures at early stages of construction depends on many factors. One of these is the formation of cracks, which may be crucial in some applications. One particular application is the deep geological disposal where a multi-barrier concept is considered. Indeed, the reference solution for long-term radioactive waste management currently being studied foresees to condition B&C wastes in disposal packages, also called “Monoliths B” and “Supercontainers” respectively, that are intended to be disposed in the geological repository. Those conditioning operations are planned to be performed in two dedicated surface facilities, usually called the “post-conditioning facilities” for B&C wastes. Monoliths B and Supercontainers will then be emplaced in the geological disposal facility (GDF), respectively in the B-zone and in the C-zone of the GDF. (ONDRAF/ NIRAS RD&D plan 2013).

The Supercontainer is a prefabricated concrete container that surrounds the Primary Waste Packages (PWPs) for category C waste as seen in Figure 1-1

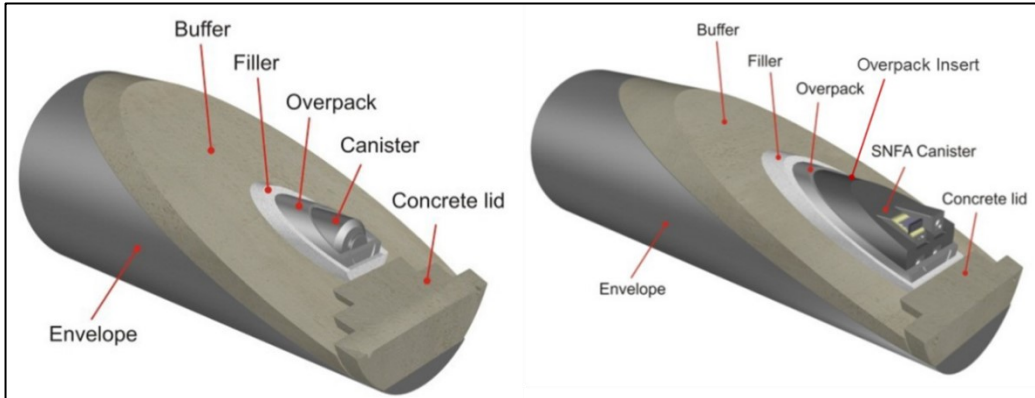


Figure 1-1. Supercontainer components RD&D Plan ONDRAF/ NIRAS 2013 (category C-waste) adapted from[1]

The Supercontainer consists of the following components:

- A carbon steel overpack that contains the PWPs (CSD-V or SNFA encapsulated in a canister);
- A cylindrical buffer consisting of a concrete container and a concrete lid;
- A cementitious filler between the overpack and the concrete buffer, that fills the annular gap between the overpack and the pre-cast buffer component during fabrication of a Supercontainer;
- A stainless steel sheet wrapping the concrete buffer.

The Supercontainer packages are disposed in disposal galleries where a concrete lining guarantees the stability of these ones. A cement backfill fills the gap between the concrete lining and the Supercontainer. Figure 1-2 presents a cross-

section of the Supercontainer inside the backfilled disposal galleries. An extensive study on construction practicability of Supercontainers has been conducted in [4] where a half scale test of the real structure is constructed and

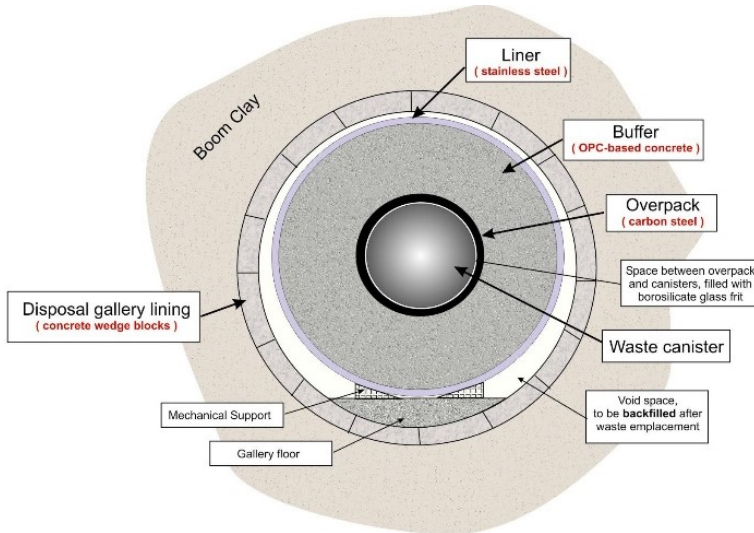


Figure 1-2. Cross-section of Supercontainer adapted from [1]

studied.

Given the conceptual plan design, it is worth noting that the C waste (high-level/long life radioactive waste) emit large amount of heat which will significantly increase the temperature in the Supercontainer leading to thermo-hydro-mechanical (THM) perturbations. It has been anticipated that the temperature in Supercontainer containing vitrified high-level waste (VHLW) could increase up to more than  $90^{\circ}$  at the interface between the filler and the buffer [5]. The presence of such thermal gradient intensifies the chance of cracking.

The mechanism responsible for crack formation in non-reinforced concrete is highly complex involving a number of coupled processes. These depend upon the cement composition, water to cement ratio, moisture, temperature and aggregate fractions, and internal or external loading. The problem is challenging and falls under a broad class of studies referred to as thermo-hydro-mechanical problems (THM). In particular, the moisture field plays a crucial role in the

stress-strain behaviour of the material under thermal transients. Inclusion of the moisture field invokes several important processes such as drying shrinkage and creep induced by moisture transport, conduction, convection, etc.

From the perspective of mathematical models, the most commonly used approach to address the above problem is via a continuum approach, which considers concrete as a homogeneous medium. To mention some of the remarkable works done in this area [6-11].

Parameters for such models are obtained by means of laboratory and in-situ experiments and via inverse analysis. The main problem with the continuum approach is that the underlying physical and chemical processes are not explicitly considered. As a result, this approach might lead to inaccurate results compared to observed data. Concrete is a heterogeneous material consisting of aggregates, interface transition zones, air pockets and bulk cement paste. Most physical and chemical processes manifest themselves at the scale of bulk cement paste while their root cause originates from lower scales. In particular, established technical approach to model mechanical properties of concrete such as shrinkage or creep, which are provided in standard codes and generally used in practice to estimate behavior and performance of concrete. These models are calibrated against each set of experiments using empirical coefficients. There are major drawbacks with such modelling approaches, firstly these models need to be calibrated against each set of experiments with specific material design, secondly the reported values are in an average sense cross sectional property, and not suitable for use in finite element analysis where material point data is necessary at every Gaussian point. Moreover, the processes are decoupled in such calculations, so any change in the contributing parameters to THM behavior, for example, curing, temperature, relative humidity changes, etc., demand a new set of calibration against experiments [12-15].

Therefore, these drawbacks confirm the need for more predictive approaches where material design optimization and a physics-based model are part of the modelling framework. This however is already attempted by many researchers for specific composition types and material attributes e.g. hydration reaction, mechanical properties, retention curve, etc. [3, 16-18] These modelling approaches have been relatively successful [2, 19, 20] to account for a single property or phenomena. To mention a few, [21-24], have proposed different models to capture THM behavior of OPC based materials but a coherent coupling of processes and scales are missing in their work, i.e. the constitute laws are either derived and applied solely from macro scale observations, no direct coupling of microstructure is present in their modelling approach, mechanism responsible for shrinkage at different scales is not well defined, the transport properties and pore space is not accounted for and finally they do not aim to be predictive, meaning that calibration still remains a key attribute in their modelling approach.

## **1.2 Aims of thesis**

The overarching objective of this study is to investigate the THM behavior of concrete within a multiscale framework. More importantly, to be able to predict fundamental properties of concrete based on its composition to enable optimization of its design is one of the main aims of this work. This, however, cannot be achieved without an in-depth study of phenomena and parameters, which are affecting the macro-behavior of the concrete. Therefore, a fully coupled framework in which, material properties are derived using a multiscale modelling technique right from material composition and its microstructure is a great added value to the field of concrete technology. Such framework can

significantly facilitate the material optimization and lower the time for possible experiments and finally result in a more refined and reliable design. In this regards, A hierarchical multi-scale, multiphysics framework guided by microstructure description is established to deliver following objectives:

- A microstructure-informed pore network modelling framework where transport properties such as water retention curve and water permeability are estimated
- A multiscale drying shrinkage model where drying shrinkage strain is directly computed from cement mix composition
- A micromechanical model to compute mechanical properties such as elastic modulus and coefficient of thermal expansion at two level of cement paste and concrete.
- A preliminary attempt for THM analysis for Supercontainer using material parameters derived from developed framework in this study in order to investigate firstly the evolution of Supercontainer under thermal loading and secondly examine its damage and cracking potential.

### **1.3 Scope and limitations**

The literature in field of concrete technology is truly vast, consequently the number of published works and proposed models is huge. Although it is aimed to review this field, it is not feasible to cover the entire research area and certainly many other models than those cited herein have been proposed over the years. The focus of the reviewed researches was on models that give a material point description of concrete and study concrete more in a theoretical manner than engineering and empirical fashion. The limitation of the models proposed here can be summarized as follows:

- Throughout the thesis it is assumed that C-S-H gel consists of two distinct types of low and high density gel.
- The developed pore network has been developed with assumption of a constant connectivity or coordination number assigned as six for all the pore classes.
- The shape of pores and throats are assumed to be spherical and cylindrical respectively.
- The mechanical properties of solid skeleton and bulk porous structure are assumed to be constant over the course of drying.
- The pore network and the drying shrinkage model are only tested with OPC-based materials and blended systems are not tested.
- The presence of interfacial transition zone (ITZ) in upscaling the drying shrinkage and mechanical properties from cement paste level to concrete level is neglected.
- In THM modelling of Supercontainer the hydration reaction of filler and the lid is neglected.

## 1.4 Outline of thesis

This thesis consists of two scientific papers (chapter 2 and chapter 3) and three independent chapters. The first paper proposes a new framework to estimate water sorption isotherm (WSI) via a multiscale approach, which integrates particle packing, cement hydration kinetics and pore network models. Thus no experimental data concerning pore size distribution or WSI (except for geometrical parameter) is needed as inputs other than the composition of the material, known microstructural features of high density (HD) and low density (LD) C-S-H phases for OPC based materials and cement hydration kinetics

model, which is usually calibrated with hydration experiments. The capability of the framework is demonstrated by comparing the model predictions with a number of experimental desorption WSI. Desorption WSI has been the focus because the ultimate goal of the first chapter is oriented towards drying shrinkage problems within the context of unsaturated poroelasticity.

Chapter 2 presents a new analytical framework that relies on minimal inputs and combines a number of existing techniques to estimate reversible drying shrinkage strain of OPC-based materials. This includes a multiscale framework for estimating water (de)sorption isotherm (WSI) from Chapter 1, an analytical homogenization technique to estimate bulk modulus, and a multi-mechanism based drying shrinkage formulation. The minimal inputs needed are the cement composition, microstructural information and mechanical properties of hydrated phases of hardened cement paste. A pore network model that forms the core module of the multiscale WSI provides a quantitative basis for the drying shrinkage formulation. The unique feature of the framework is that only two calibration parameters are involved: (i) a geometric parameter used in the pore network model, and (ii) a constant in the disjoining pressure relationship, which is set to unity mainly due to a lack of knowledge. Importantly, there is no need to calibrate these parameters for every experiment. Results from the framework are compared against shrinkage data from literature that encompass both virgin materials (samples that have never been dried prior to the test) and non-virgin materials. A reasonably good correspondence has been achieved with respect to the non-virgin materials, whereas, the results for the virgin materials are examined mainly to gain qualitative understanding of the role of the microstructure on irreversible deformation and thus to propose a phenomenological model.

The first two chapters were applicable for stationary conditions, therefore in order to introduce time-dependent modelling capability to the framework

Chapter 4 takes the pore network modelling one step forward by modelling saturated and unsaturated permeability of cementitious materials using a novel algorithmic implementation. This chapter presents a multiscale and largely predictive approach, which can drive the information from microstructure and integrate them into a representative numerical framework to model both intrinsic and unsaturated permeability. This numerical framework consists of different modelling tools discussed in Chapter 2 of this thesis to arrive at a statistically representative pore network, which is used as a basis to carry out moisture transport calculations. The proposed pore network modelling framework is validated against an extensive set of experimental data that includes a very wide range of materials.

Chapter 5 describes a micromechanical framework that is adopted, firstly, to model mechanical properties of cementitious materials such as elastic modulus, Poisson's ratio and coefficient of thermal expansion (CTE), and secondly to examine the effect of drying shrinkage at cement paste and concrete levels. The aim of this analysis is to firstly provide a more informed insight on thermo-mechanical processes on lower scales i.e., microstructure, cement paste and concrete level, and secondly examine our current understanding of drying shrinkage at cement paste and concrete levels. The computational framework starts with a hydration model that is employed to generate a synthetic microstructure that is consistent with cement hydration process, and the resulting microstructure provides geometrical input to a finite element model (FEM) in which mechanical, thermo-mechanical and hydro-mechanical analyses are carried out to determine the aforementioned properties.

Finally, Chapter 6 presents a demonstration on how the multiscale framework developed in chapters 1-5 can be utilized to model THM analysis on structure level. In this regards, a preliminary finite element analysis integrating all the developments of this multi-scale framework is performed at the level of the

structure with the modelling of the second half-scale supercontainer test [4]. This test consists the application of a thermal load inside a concrete cylinder mimic the placement radioactive heat emitting waste effect and the effect of the temperature increase on the concrete in large scale condition. The coupling term existing in the THM analysis is the temperature which alters the transport and mechanical (thermal and drying creep) properties and moisture field which is coupled to mechanical loading in a form of shrinkage strain. In this chapter the evolution of thermal and moisture fields are reported and the resultant stress field is discussed in details. Finally, an isotropic damage model is hired to examine damage probability of the structure during the thermal loading.

The flow of the information and how the developed tools and methods in this PhD study work coherently in order to deliver THM modelling parameters and perform a large scale modelling analysis is illustrated in Figure 1-3 where modelling relies on microstructure as the main source of information and the framework starts with microstructure modelling which provides the input for three main sub-frameworks developed in this study denoted as THM parameter estimation section and it includes, (a) pore network modelling for transport properties, (b) drying shrinkage model and (c) micromechanical modelling for thermo-mechanical modelling. This part of the framework is where the real contribution and added value has been made. Finally, the framework is centralized in an FEM numerical code in order to perform a large scale time dependent THM analysis where Supercontainer is used as reference case study.

# 1. Microstructure Modelling

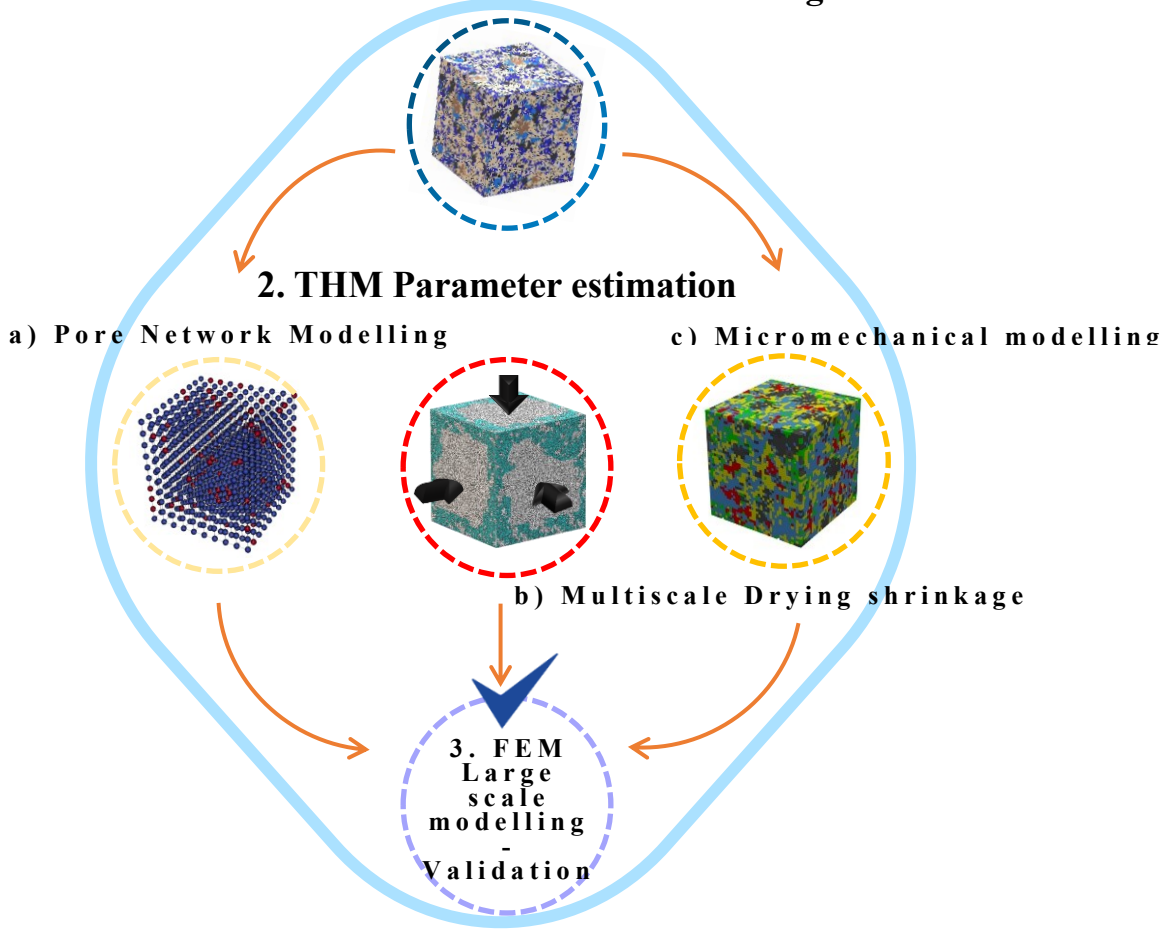


Figure 1-3. The developed workflow for multiscale THM modelling of concrete

## 2 A Multiscale Framework to Estimate Water Sorption Isotherms for OPC-based Materials

---

Based on ‘A multiscale framework to estimate water sorption isotherms for OPC-based materials’

Babaei S., Seetharam S.C., Mühlich U., Dizier A., Steenackers G., Craeye B.

Published in: Cement and concrete composites - ISSN 0958-9465 - 105(2020)  
[doi: 10.1016/J.CEMCONCOMP.2019.103415](https://doi.org/10.1016/J.CEMCONCOMP.2019.103415)

# Chapter 2

### 2.1 Introduction

The importance of water content *vis-à-vis* the durability of cementitious materials is long established [12, 25]. In particular, water sorption isotherm (WSI) is a key material property that is used extensively in the study of moisture transport of unsaturated cementitious materials with a view to gain improved understanding of many durability problems such as drying shrinkage, creep, corrosion, carbonation, freeze-thaw, etc. The mechanisms affecting WSI are highly complex and depend on concrete composition such as cement type and content, water to cement ratio, aggregates, additives and fillers, moisture content and environmental factors such as ambient temperature [26].

A central theme of this study is to explore the possibility of going from the knowledge of mix composition to predicting WSI. Such a framework is of profound importance, for instance, in the study of durability of concrete structures in the existing nuclear power plants. Hence, as far as possible, predictive approach to the determination of WSI is pursued so that any OPC based mixes can be accommodated without the need for an experimental campaign for every mix composition.

The principal approach to obtain WSI is via appropriate experimental techniques such as conventional wetting/drying [27, 28], dynamic vapour sorption [29, 30] and centrifuge experiments [31, 32]. For low permeability materials like cementitious materials, it is often time consuming to determine WSI accurately for the complete range of degree of saturation ( $S_i$ ) [33]. However, once experimental data become available, an analytical model can be fitted in a way that WSI can be predicted for various conditions, for example, different water to cement ratios and porosity. An overview of such analytical models is available in Burgh et al. [34]; a notable work cited in their reference is that of Kumar et al. [35], which explored numerous analytical models to successfully predict WSI for a range of porosity. The accuracy of such models not only depend on their mathematical form but also on access to experimental WSI.

A second approach to predict WSI is to derive it from microstructural information such as pore size distribution and the type of water associated with different pore classes. Kelvin's equation is then used to establish an equilibrium relation between water content and capillary pressure, especially for gel and capillary pores. In this regard, Pinson et al. [36] predicted WSI by classifying water into interlayer, gel, capillary and surface adsorbed water. As a first approximation, they assumed a linear relationship between water content and capillary pressure for the interlayer space, i.e., for relative humidity below 15%. For the gel and capillary pores, they extracted pore size distribution from Barrett-Joyner-Halenda (BJH) method and then combined it with Kelvin's equation to derive WSI. For the empty pores in gel and capillary pores, they also considered the effect of adsorbed water via Langmuir and Brunauer–Emmett–Teller (BET) methods. Burgh et al. [34] proposed a model for WSI that also considers interlayer, gel and capillary pore classes as Pinson et al. [36]. They used a modified form of classic Powers and Brownyard hydration model [37] to capture pore volumes. Then a continuous probability distribution is used with shape and

scale parameters calibrated with experiments to describe the whole pore size distribution range. With the pore size distribution, Kelvin's equation is used to determine the equilibrium relationship between water content and capillary pressure. More recently, Masoero et al. [38] studied the densification of Calcium-Silicate-Hydrate (C-S-H) gel and its effect on WSI during hydration. Their model combines a C-S-H gel description from nanoscale simulations with evolving capillary pore size distributions using a simple hydration model, however only for  $C_3S$ . This information is then coupled with Kelvin's equation to obtain WSI.

An interesting and alternative approach to predict WSI is the pore network model pioneered by Mason [39], which conceptualizes a porous material as a network of pores connected by throats (constrictions or windows) and locally invoking Kelvin's equation. He demonstrated the capability of the network model to predict adsorption-desorption hysteresis using a hypothetical network. It was possible to capture hysteresis because pore blocking is a natural consequence of the network model where pore connectivity is inherently defined. In this regard, Islahuddin and Janssen [40] applied the pore network model to numerically explore WSI of Berea sandstone based on topologically equivalent network obtained from micro-CT scanning.

In conclusion, with the exception of Masoero et al. [38], the first two approaches strongly rely on experimental WSI for calibrating the model parameters before they can be used for predictions. Although, Masoero et al. [38] do not use experimental WSI, their model is demonstrated for  $C_3S$  (Alite) system only. In addition, the first two approaches will need some calibration to incorporate sorption hysteresis unlike the alternative approach. Finally, to the authors' knowledge, the alternative approach, i.e., the pore network model has never been applied to complex microstructures such as cementitious materials. Although the

pore network model is applied for other porous materials, it relies entirely on experimental pore size distribution as a key input.

This study therefore proposes a new framework to estimate WSI via a multiscale approach, which integrates particle packing, cement hydration kinetics and pore network models. Thus, no experimental data concerning pore size distribution or WSI (except for geometrical parameter) is needed as inputs other than the composition of the material, known microstructural features of high density (HD) and low density (LD) C-S-H phases for OPC based materials and cement hydration kinetics model, which is usually calibrated with hydration experiments. The capability of the framework is demonstrated by comparing the model predictions with a number of experimental desorption WSI. Desorption WSI has been the focus because the ultimate goal of the present study is oriented towards drying shrinkage problems within the context of unsaturated poroelasticity.

## 2.1 Multiscale framework

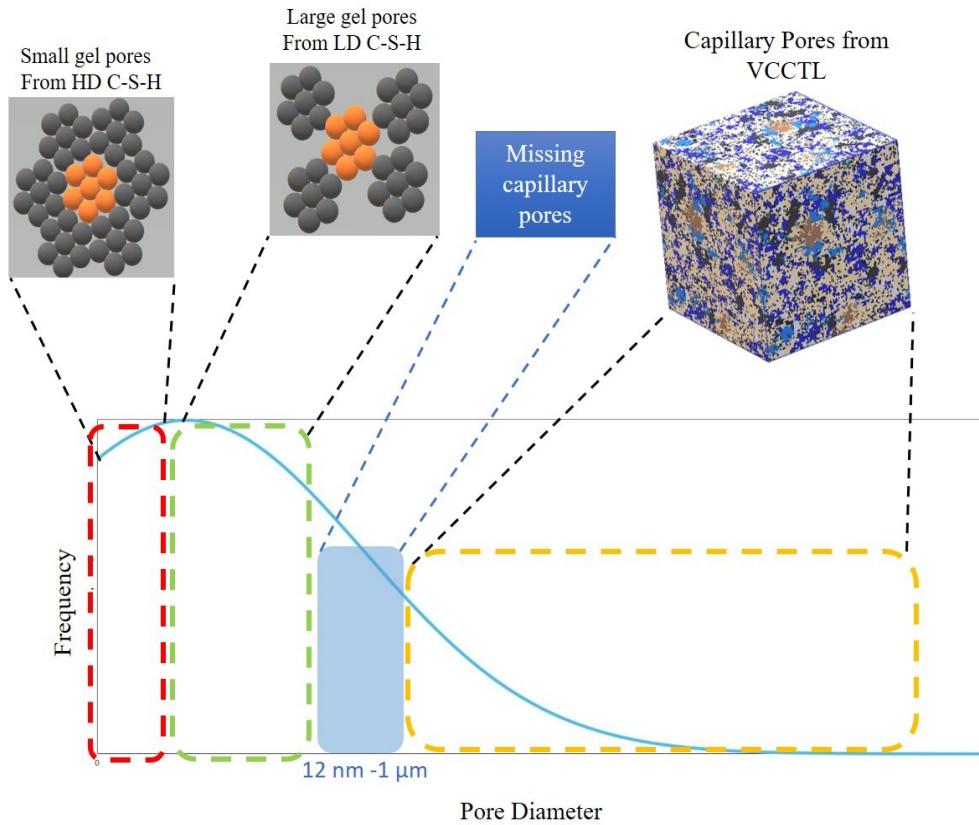


Figure 2-1. Typical pore size distribution of cementitious materials

The proposed multiscale framework for water sorption isotherm integrates three models: (i) cement particle packing, (ii) microstructural cement hydration kinetics, and (iii) pore network. For lower (gel) pore size range, which is characterized by HD and LD C-S-H, the particle packing model computes total porosity and pore size distribution relying on a principal assumption that the variability of HD and LD C-S-H characteristics in terms of particle packing is limited for OPC [41]. Based on fundamental inputs such as cement composition and reaction conditions, the microstructural model computes volume fractions

of various hydrated phases, capillary porosity and pore size distribution but for a higher capillary pore size range ( $> 1 \mu\text{m}$ ), which is primarily dictated by the limitation of resolution of the model used. However, these two models do not cover the mid pore size range (small capillary pores), i.e., between tens of nm to  $1 \mu\text{m}$ , as demonstrated in Figure 2-1. Therefore, an approximation to cover this missing pore size range is proposed (Section 2.3) and justified (Section 2.5). Based on the computed pore size distribution for the full range of pore sizes, the

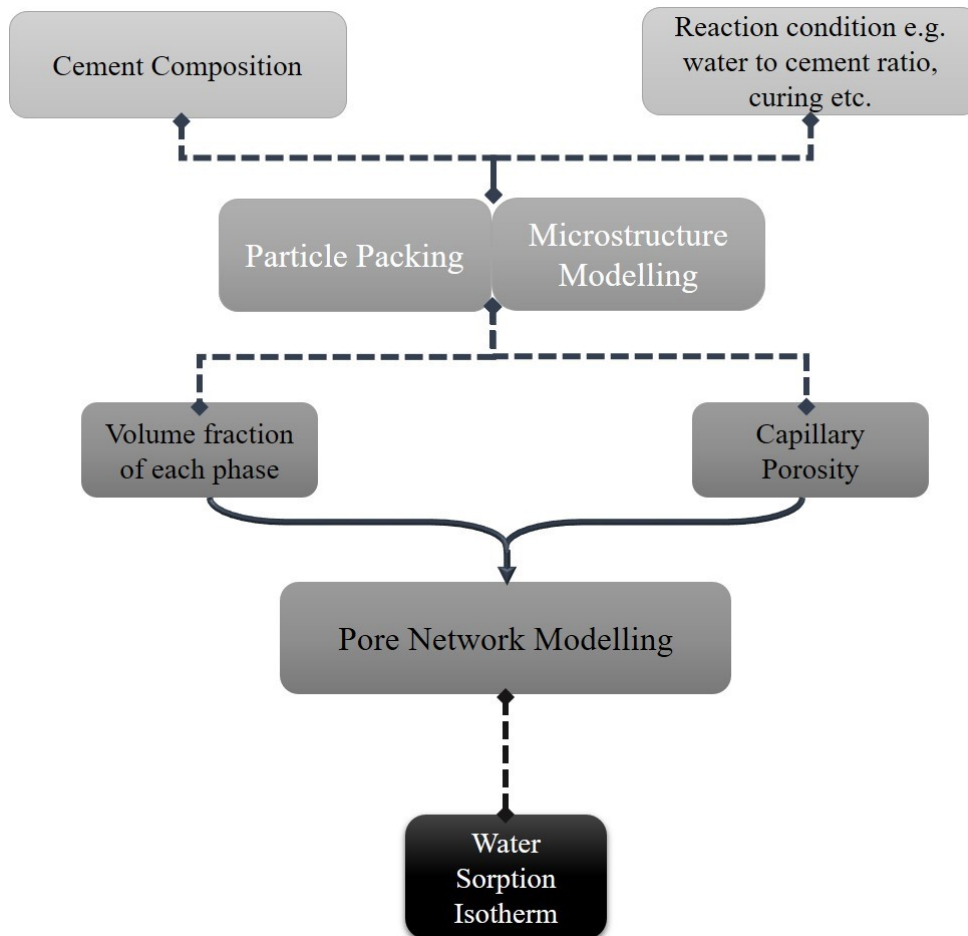


Figure 2-2. Proposed multiscale framework for estimating water sorption isotherm

pore network model computes WSI for a given material composition. These steps are illustrated in Figure 2-2.

### 2.1.1 Particle packing model: nm scale

In order to estimate porosity and pore size distribution of lower (gel) pore size range, a conceptual model that describes the microstructure of C-S-H gel has to be chosen. Various conceptual models such as layered, colloidal and fractal models have been proposed in the recent past [42]. The particle packing model used in this study follows the colloidal model for C-S-H gel proposed by Jennings [43] and illustrated in *Figure 2-3*. This is a self-consistent model with respect to a number of experimental data, for example, specific surface area and density measurements. The term ‘particle’ used in this study equates to the term ‘C-S-H globules’ in the Jennings’s model. These globules (particles) are packed together to form HD and LD C-S-H and the spacing between the globules are referred to as gel pores. Thus, if the packing density for HD and LD C-S-H are known then their respective gel porosities as well as pore size distribution can be geometrically extracted. It is however worth noting that the Jennings’ colloidal model is not the only available conceptual model, different assumption of C-S-H gel structure which is an active field of research can lead to different pore size distribution. Due to computational complexity however, the mono-sized spheres are the only studied geometry in this thesis [44].

However, the pore size distribution of pores larger than the gel pores cannot be estimated with the particle packing model. Some assumptions are made to fill this missing information as discussed in Section 2.3.

The two types of C-S-H phases, namely, HD C-S-H and LD C-S-H are well-characterized [45-47]. The difference between the two C-S-H phases mainly lies in their gel porosity and packing density; the HD C-S-H being characterized by a gel porosity,  $\phi_{HD}$ , of roughly 0.24, and the LD C-S-H being characterized by a gel porosity,  $\phi_{LD}$ , of roughly 0.37. It is worth noting that the corresponding packing densities,  $(1 - \phi_{HD}) = 0.76$  and  $(1 - \phi_{LD}) = 0.63$ , come very close to the maximum packing densities of mono-sized spherical packing. The packing density of HD C-S-H is of striking similarity to the highest possible density of ordered spheres, known as the face-centred cubic lattice, equal to 0.74, and the packing density of the LD C-S-H is of striking similarity to the so-called random close packing (RCP) of 0.64 [44, 48-50].

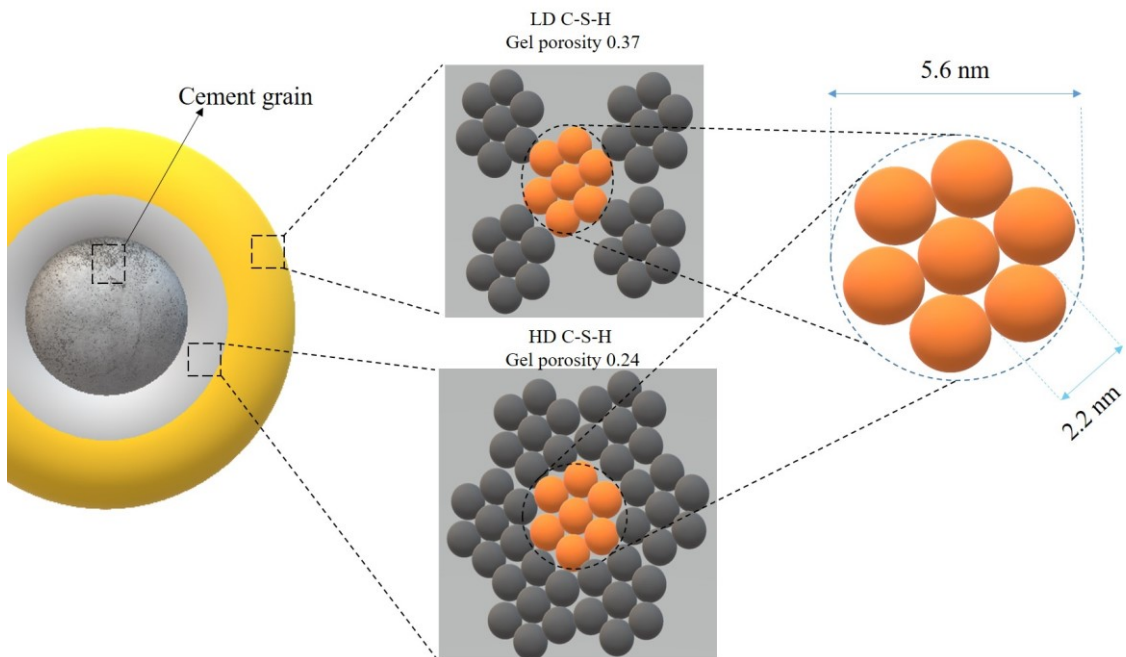


Figure 2-3. Particle packing and globule concept from Jennings model.

The particle packing model used in this study is similar to the work of Fonseca et al. [42] and Liu et al. [2]. The choice for the size of the particles is based on

Jennings's [43] conceptual model, which considers mono-sized particles of size 5.6 nm (*Figure 2-3*). With respect to pore size distribution, a representative volume element (RVE) of size  $150 \times 150 \times 150 \text{ nm}^3$  is chosen after testing three different RVE sizes (100 nm, 150 nm and 200 nm). Liu et al. [2] also arrived at the same RVE size after testing various RVE sizes. So, Initially, a small number of mono-sized particles each of diameter 5.6 nm are randomly distributed in space, and then they are compacted to the maximum extent without overlapping by moving spheres closer to the centre of the RVE. A new set of particles is added and again compacted. This procedure is repeated until the desired packing density is achieved. One additional step that is taken in comparison to the work of Liu et al. [2] is that after compacting, the compacted globules are further discretized into sub-globules made of mono-sized spheres with size of 2.2 nm, so that the water in the interlayer space (space between 2.2 nm spheres) are also accounted to be consistent with the Jennings' colloidal model. With this, the extraction of pore size distribution is carried out. (*Figure 2-3*). The results obtained from this model corresponds well with the model of Liu et al. [2] for HD C-S-H as shown *Figure 2-4*, which is attributed to the fact that the maximum density has to be achieved irrespective of the algorithm used. However, there is some deviation for LD C-S-H, which is attributed to the fact that the required packing density is lower compared to HD C-S-H, which means the results can become sensitive to the particle packing algorithm and pore size distribution extraction method. It is also worth noting that typically 40% of the total volume of RVE of cement paste is comprised of HD and LD C-S-H [12]. Therefore, the particle packing model accounts for majority of the pore size range.

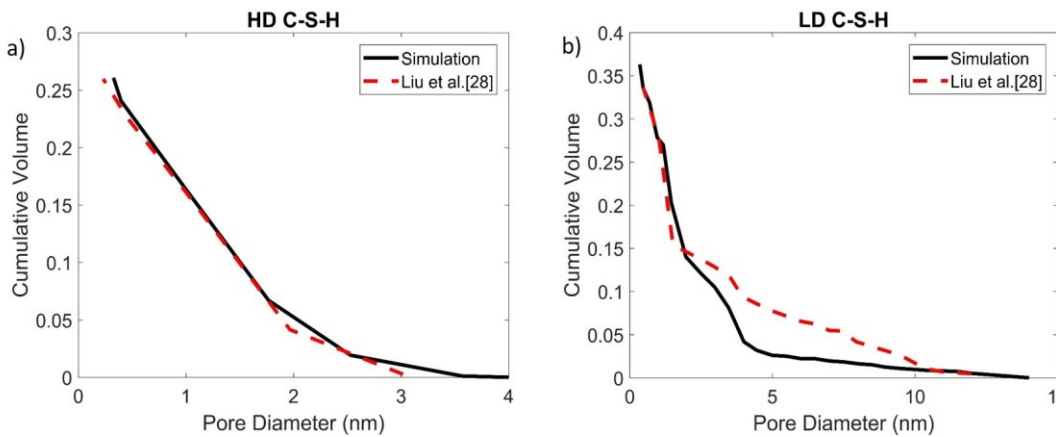


Figure 2-4. Comparison of pore size distribution obtained from the 3D particle packing model used in this study against the 3D particle packing model of Liu et al. [2]: (a) HD C-S-H, and (b) LD C-S-H.

## 2.2 Microstructural cement hydration kinetics model: $\mu\text{m}$ scale

All the existing microstructural models are mainly intended to study microstructural properties such as volume fractions of hydrated phases, porosity, percolation threshold and degree of hydration but not pore size distribution. There are currently no cement hydration kinetics models that can estimate reliable pore size distribution. This is a limitation of this framework. However, as a first approximation, such a hydration kinetics model is still relied upon for estimating pore size distribution.

A comprehensive review of microstructural modelling and in particular cement hydration kinetics models can be found in Thomas et al. [51]. From the latter as well as author's own experience, it is found that Virtual Cement and Concrete Testing Laboratory (VCCTL) suite offers control over wide range of variables

and input parameters and is experimentally better validated compared to other hydration models [52]. Hence, VCCTL is taken forward in this study. In VCCTL, a 3D cement paste microstructure is digitized into a cubic lattice and each volume element or voxel of the cube is assigned to a phase (porosity, C-S-H, CH, etc.). VCCTL simulates the hydration process as an iterative procedure of dissolution, diffusion, and reaction. This iteration evolves the initial lattice cube and forms a reasonable spatial distribution of the anhydrite cement, combined hydration products, and capillary porosity. The minimum voxel size that can be specified is  $1\ \mu\text{m}$ , which also implies that capillary pores below  $1\ \mu\text{m}$  cannot be captured. Hence, only total porosity and pore size distribution of pores greater than  $1\ \mu\text{m}$  can be captured.

Note that one may also consider cement hydration kinetics model that are resolution free or vector-based (e.g. HYMOSTRUC [53]), which have no limitation on the minimum voxel size. However, as shown by Ye [54], the modelled pore size distribution results are not promising. Such resolution free microstructural models are usually used with voxel size larger than  $1\ \mu\text{m}$ , as capturing the hydration and interaction of the cement particles from nano to micro scale is computationally prohibitive. Moreover, such resolution free models read the spaces existing between the reaction products but not the pores within the C-S-H gel as a product of hydration reaction [55]. This in fact justifies the use of particle packing (Section 2.1.1) as a necessary component of the framework to estimate gel pore size distribution.

### 2.3 Missing pore size distribution: nm to $\mu\text{m}$ scale

The missing pore size distribution from biggest gel pores (14 nm based on particle packing) to smallest capillary pore imposed by the hydration model (1  $\mu\text{m}$  by VCCTL) is derived by using the pore size distribution of the capillary pores as a surrogate (Section 2.2). In the absence of any data, this should be treated as a crude approach. The implication of this approximation is discussed in Section 1.1.1. In this approach, a Weibull distribution function is fitted on the capillary pore size distribution obtained from VCCTL, which is available from one  $\mu\text{m}$  to tens of  $\mu\text{m}$ . The Weibull distribution function is defined as:

$$f(x) = \frac{\beta}{\eta} \left(\frac{x-\gamma}{\eta}\right)^{\beta-1} e^{-\left(\frac{x-\gamma}{\eta}\right)^\beta} \quad (2-1)$$

where  $x$  is a pore size,  $\beta$  is the shape factor,  $\eta$  is the scale parameter and  $\gamma$  is the location parameter. Once the Weibull distribution is fitted for the capillary pore size range, the shape is preserved but by manipulating the location and scale parameter the pore size range is stretched to cover a wider range from 14 nm to 1  $\mu\text{m}$ . This missing pore size range is then added to the capillary pore network, ensuring that the calculated capillary porosity is still respected.

### 2.4 Pore network model

The estimation of WSI of cementitious material is carried out using a pore network model with steady state analysis. A pore network is a virtual network of pores and throats, which are connection between the pores [56]. This model can reconstruct WSI on the whole capillary pressure range provided accurate

pore/throat size distribution data as well as topology of the network are available, including appropriate physics given the pore size range of a typical cement paste material.

There are several techniques to characterize the pore space. Imaging techniques such as producing 3D images by mapping the real interior structure of original material are promising but time consuming and expensive. This mapping can be carried out using destructive approach of cutting and stacking serial 2D sections, followed by confocal laser scanning microscopy, non-destructive X-ray microtomography ( $\mu$ CT), and constructing synthetic 3D images from high resolution 2D thin sections using statistical methods or geological process simulation [56, 57]. However, as already described in Sections 2.1.1 and 2.2, in this study, pore space is characterized based on the particle packing and available microstructural modelling tools (VCCTL here).

In this study, the pore space of the cementitious material is characterized by means of three main networks: HD C-S-H, LD C-S-H and capillary porosity. The most important variable to construct a network in this regard is the volume fractions of these three networks. First of all, the volumetric ratio of HD and LD C-S-H network is estimated via Jennings-Tennis's hydration model [58]. Depending on this ratio, the porosity of the whole gel pore space is derived as follows:

$$\varphi_{gel} = \varphi_{HD} \cdot V_{HD} + \varphi_{LD} \cdot V_{LD} \quad (2-2)$$

where  $\varphi_{HD}$  is the porosity of HD C-S-H equal to 0.24 [45],  $V_{HD}$  is the volume fraction of HD C-S-H in C-S-H gel,  $\varphi_{LD}$  is the porosity of LD C-S-H equal to 0.37 [45], and  $V_{LD}$  is the volume fraction of LD C-S-H with  $V_{HD} + V_{LD} = 1$ .

The volume of gel pores is defined as:

$$V_{gel} = V_{CSH} \cdot \varphi_{gel} \quad (2-3)$$

where  $V_{CSH}$  is the volume fraction of C-S-H gel, which is obtained from the hydration model (section 2.2). The volume of capillary pores is also obtained from the hydration model. Once the volume fractions of all the networks are available, a unified network can be generated by merging all these three networks. Each network has its own pore size distribution and size, which comes from the hydration model, particle packing model and aforementioned equations.

#### 2.4.1.1 Geometrical considerations

To ensure that the simulations are reproducible, which means keeping fitting coefficients to a minimum (Eq. (2-4) and (2-5)), and to avoid convergence problem, a cubic network with fixed coordination number is constructed for each phase, i.e., HD C-S-H, LD C-S-H and capillary porosity. The pores and throats of the network can have different geometries such as cubes, triangles, spheres, cylinders, etc. To accelerate the simulation, in this study, the pores are defined as spheres and throats as cylindrical pipes. To construct a cubic network of specific size, in addition to pore size, the connectivity or coordination number and throat sizes and lengths are required. The coordination number is defined as the number of connected throats for each pore. Real porous materials might have different coordination numbers based on their pore structure but to optimize the simulation procedure, the coordination number of the cubic network is taken as six. This means each pore is connected to its six neighbouring pores. *Figure 2-5* demonstrates a few examples of networks with coordination numbers of 6, 12 and 26 for a network with 27 pores.

It is not possible to experimentally obtain throat size distribution as the network of pores and throats are idealization of complex pore network in cementitious materials. Hence, some assumptions have to be made. The first rule to define throat size is to make sure that every throat diameter is smaller than its neighbouring pores. As a first approximation, the throat size,  $R_{throat}$ , is

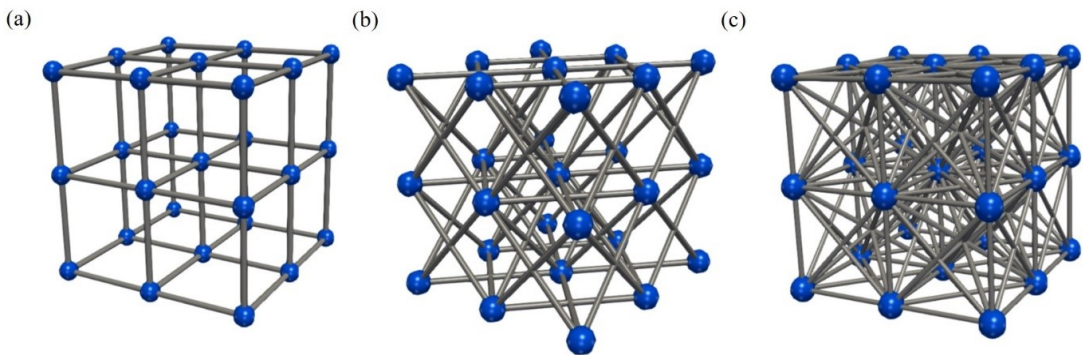


Figure 2-5. Effect of different coordination numbers on a cubic network with 27 pores. a) coordination number = 6, b) coordination number = 12, c) coordination number = 26

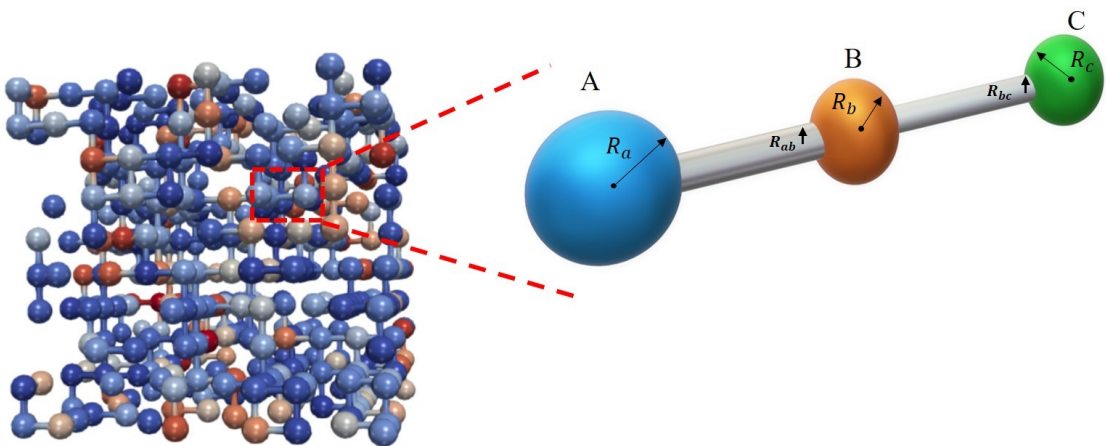


Figure 2-6. The relationship between throat diameter and its neighbouring pores.

arbitrarily defined as a linear function of the radius of neighbouring pores,  $R_{np}$  as follows:

$$R_{throat} = \alpha(\min(R_{np})) \quad (2-4)$$

where  $\alpha$  is a factor whose value should be less than 1. For instance, for a configuration of three pores A, B and C shown in *Figure 2-6* with radius  $R_a \leq R_b \leq R_c$ , the throat size for their connecting throats should be:

$$R_{ab} = \alpha R_a, R_{bc} = \alpha R_b \quad (2-5)$$

It is also worth mentioning that the throat length is also defined using a comparable equation as Eq.(2-5), where the length of the connecting throat between two pores is defined as:

$$L_{throat} = \omega(\max(R_{np})) \quad (2-6)$$

with  $\omega$  being a scaling factor, which should be greater than 1 so that there is no overlapping of pore neighbouring pore bodies. In this study, the following values have been assigned to the coefficients:  $\alpha = 0.3$  and  $\omega = 1 + \alpha$ . The  $\alpha$  value is calibrated with an arbitrary WSI (experimental WSI presented in Section 2.5.2) and is held constant.

The following procedure is adopted to generate the overall pore network geometry:

- a) Assuming that the volume fraction of LD C-S-H is higher than HD C-S-H, the first step in the network construction is to generate an LD C-S-H network as a cubic network of 100 pores on each side of the cube, distributed within a  $200 \times 200 \times 200 \mu\text{m}^3$  RVE. Since capillary pores, which are usually bigger (up to tens of  $\mu\text{m}$ ) than the gel pores, are added

to the same RVE, the RVE dimensions are considered slightly larger than is necessary for solely gel pores.

- b) The second step is to generate the HD C-S-H pores and embed them inside the cubic LD C-S-H network until their volume fraction reaches a certain ratio to LD C-S-H volume fraction estimated from the hydration model (*Figure 2-7(a)*). This is achieved by embedding the HD pores (grey) between the LD pores (green) as illustrated in the inset of *Figure 2-7(a)*. This step should also ensure that the ratio of HD to LD C-S-H as estimated from the Jennings-Tennis's model is respected. It is worth mentioning that during this merging process the coordination number is continuously checked and if necessary, throats are trimmed to meet the coordination number of six for the overall network. Furthermore, note that the HD C-S-H can be as big as the LD C-S-H network or even bigger than the LD C-S-H network depending on its volume fraction. If they are of the same size, it does not matter, which network is constructed first. The sequence should however be reversed in case the HD C-S-H network is larger than the LD C-S-H network. It is worth noting that, by merging these two networks the homogenized C-S-H network will result in a WSI, which falls between the pure HD C-S-H and LD C-S-H networks as illustrated in *Figure 2-8*.
- c) The first two steps yield a homogenized C-S-H gel network into which the capillary pore network is embedded in the third (final) step. The capillary pores are added in a different manner compared to the C-S-H pores. Since in terms of number of pores the capillary pores have the smallest population and to avoid over estimation of ink-bottle effect, these pores are randomly distributed in the network rather than starting from the centre. Hence, as shown in *Figure 2-7(b)*, capillary pores (red) can be spread anywhere in the central region and beyond within the

homogenized C-S-H network (grey and green). If the RVE is sufficiently large then the randomness of the capillary pores should not significantly influence the WSI.

It is important to note that from the point of view of pore network geometry, RVE basically implies that the domain is sufficiently large enough to cover the entire pore size range as well as to ensure that the random distribution of pores do not significantly affect WSI (converged solution). RVE does not necessarily correspond to the actual RVE size because of the idealization involved in the representation of pores and throats.

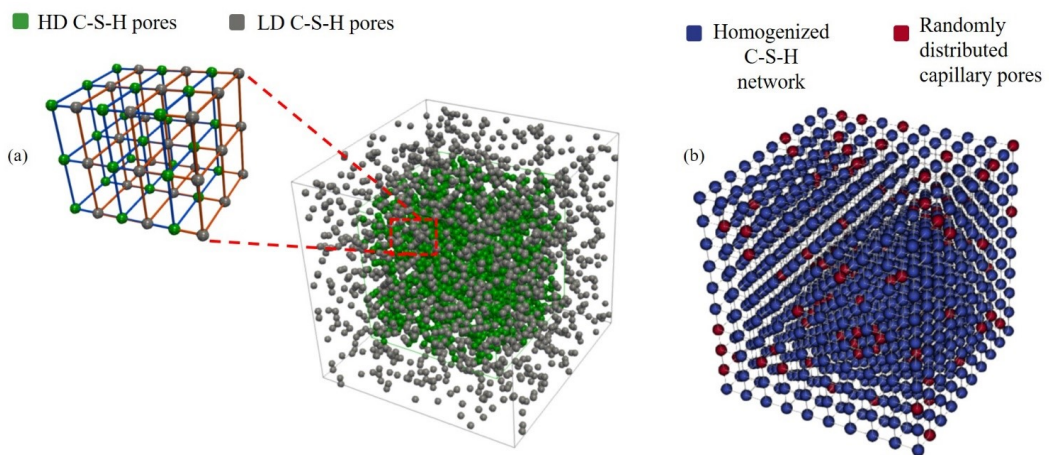


Figure 2-7. Illustration of merging of different networks (throats are shown for better visibility of merging process): (a) Homogenization of C-S-H gel network - merging HD C-S-H pores (green) with LD C-S-H network (grey), (b) Final network including homogenized C-S-H network (Blue) and randomly distributed capillary pores (red).

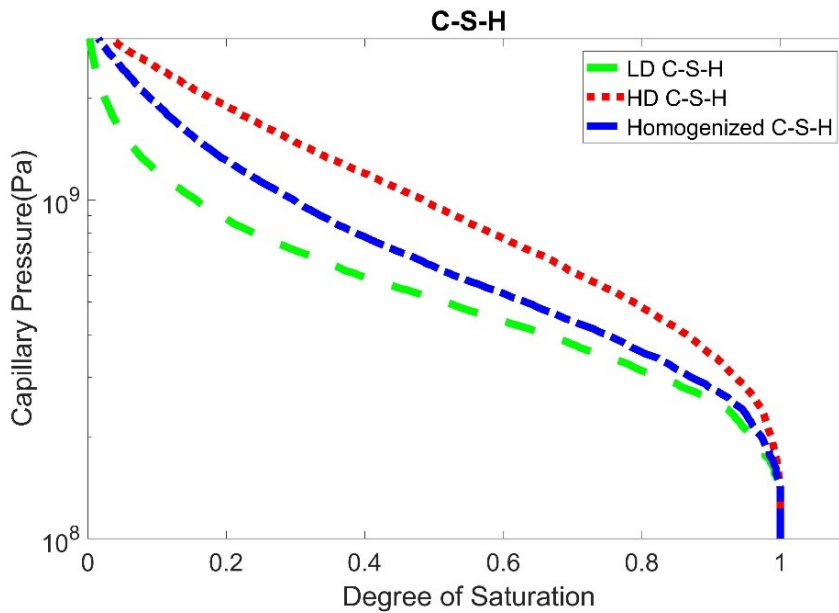


Figure 2-8. Illustration of WSI for HD C-S-H, LD C-S-H and homogenized C-S-H gel.

### 2.4.1.2 Water sorption isotherm

Because of a large variation in pore sizes and their topological arrangement in low permeability materials as is the case with hardened cement paste, a WSI displays hysteresis [59]. In the case of cement paste, this behaviour can be attributed to irreversible processes such as morphological changes in microstructures, cracking or ink-bottle effect. Both adsorption and desorption WSI are of interest to understand the moisture transport behaviour of the material as well as for moisture transport modelling. In this paper, specific attention is paid to estimating desorption isotherms because of its direct relevance to the study of drying shrinkage behaviour and issues. Desorption isotherm also

implies that some sort of invasion algorithm is necessary to mimic desorption of the initially saturated pore network.

In this study, an idealized pore network is generated using an in-house code developed in the SciPy and NumPy environment. The OpenPNM [56] library is then called upon to compute desorption isotherms. The OpenPNM library uses an “invasion percolation” algorithm based on the work of Wilkinson and Willemsen [60]. However, additional considerations concerning adsorbed water are introduced. The invasion of moist air will occur only if the applied capillary pressure (external  $RH$ ) exceeds the entry pressure of a pore/throat, which is calculated using the Young-Laplace’s equation:

$$P_C = \frac{2\sigma \cos(\theta)}{r} \quad (2-7)$$

where  $\sigma$  is the surface tension (N/m),  $\theta$  is the contact angle ( $^\circ$ ), and  $r$  is the pore radius (m) of a given pore/throat, which comes from the pore/throat size distribution. Since water perfectly wets the silicate materials and the presence of surface adsorbed water is taken into account, the contact angle is set to zero in this study [40, 61].

The invasion algorithm works in such a way that the pores with lowest entry pressure is first invaded. The throats that are connected to the invaded pores then become accessible and thus join the invasion front. This procedure is repeated until all the pores/throats are completely invaded. Further details of the algorithmic implementation are available in Gostick et al. [56] and references therein.

The invasion of pores/throats by moist air (external  $RH$ ) does not imply that all the liquid water is completely evacuated from them because water may still be present in the form of absorbed water, which is in equilibrium with the local relative humidity,  $h_m$ . Hillerborg [62] defined absorbed water as sum of adsorbed

and capillary condensation water. He attempted to propose a relationship between  $h_m$  and the radius of curvature of adsorbed water by combining the standard Kelvin and Young-Laplace equations. However, as it was difficult to define the curvature of the adsorbed water surface, as an approximation, only the curvature of adsorbed water was considered, which was determined based on the thickness of adsorbed water,  $t$ , via:

$$t = \frac{0.525 \times 10^{-8} RH}{(1 - RH/h_m)(1 + RH/h_m + 15RH)} \quad (2-8)$$

where  $RH$  is the external relative humidity (boundary condition) and  $h_m$  is defined via:

$$h_m = \exp\left(\frac{-2\sigma}{R_v T(r-t)}\right) \quad (2-9)$$

where  $R_v$  is the gas constant of water vapour (J/kg/K),  $T$  is the temperature (K) and  $r$  is the radii of pores/throats. Note that Eq. (2-8) is a modification of the conventional BET model proposed by Hillerborg [62] to account for changes in  $h_m$ .

To quantify pore wetting/drying mechanism in the pore network model,  $P_c$  is considered as the primary variable. An illustration of simulation of free drying of a cube of cement paste using the pore network model is shown in *Figure 2-9*. In order to mimic real experimental conditions, the pore network is assumed to be initially saturated ( $P_c=0$ ) and a constant boundary condition of  $P_c>0$  (or  $RH<1$ ) is prescribed incrementally over the entire  $RH$  range (0 to 1). This condition initiates drying of pores and throats until thermodynamic equilibrium is reached between the network and the prescribed external  $P_c$  based on the invasion percolation algorithm. The equilibrium  $S_l$  is then computed by taking the ratio of volume of elements of pore network that are still wet and the total

volume of the network. Adsorbed water (if present) in the pores/throats is also accounted for in the calculation of  $S_w$ . Note that the entire computation is purely a steady state analysis for each increment of  $P_c$ .

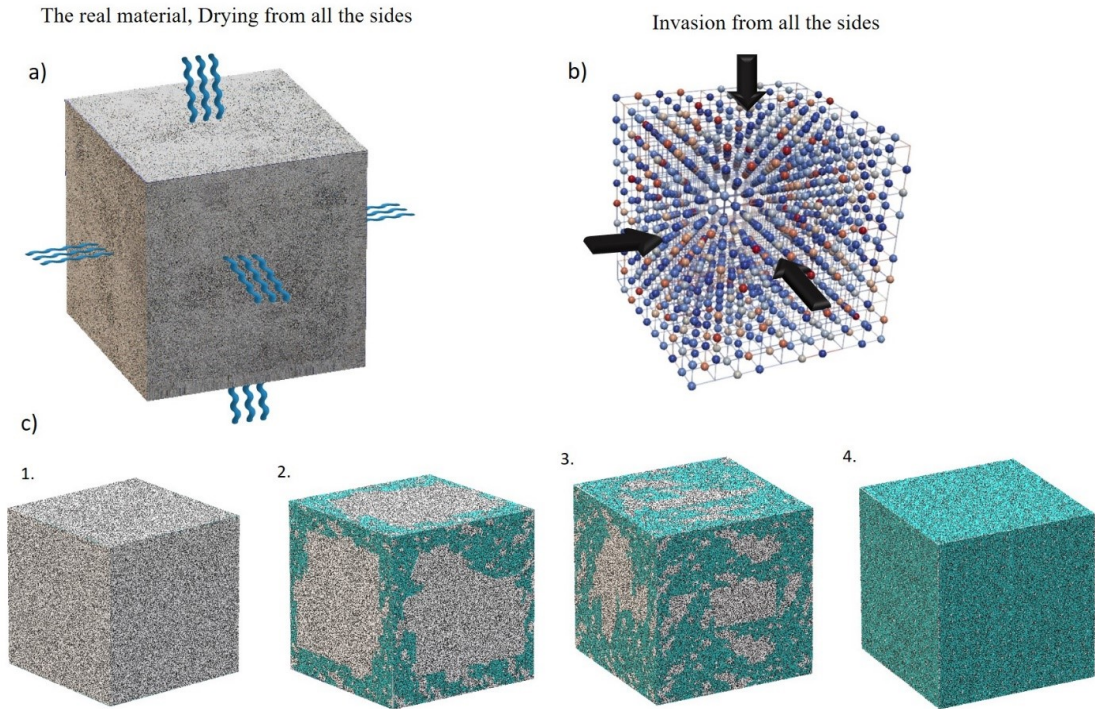


Figure 2-9. An illustration of simulation of free drying: (a) free drying of cement paste, (b) representative pore network invaded from all the sides, (c) sequences of the invasion of moist air into a cubical hardened cement paste from all the sides with random drying paths (from 1 as not invaded to 4 as fully invaded)

## 2.5 Validation

The proposed framework is validated against a wide range of measured desorption isotherms available in literature [33, 63-67]. The chosen datasets include plain cement paste, mortar and concrete to examine the capability of the modelling framework to handle different cementitious materials. The W/C of

these materials varies from 0.34 to 0.8. The mineral composition and a short description on preparation and measurement methods of the studied cases are presented Table 2-1. Further details of the experiments can be found in [33, 63-67].

Recall from Section 2 that the ultimate goal of the present study is oriented towards understanding of drying shrinkage problems within the context of unsaturated poroelasticity (e.g. [24]), where WSI is a key input data. In unsaturated poroelasticity, apart from  $S_l$ , the primary variable is typically capillary pressure instead of relative humidity (RH), which is measured experimentally. Therefore, all experimental RH data used in this study are converted to capillary pressure via Kelvin's equation, which is assumed to be valid irrespective of microstructure or RH.

The hydration model considers appropriate curing conditions, including temperature as reported in *Table 2-2*. In particular, the curing period varies from 56 days to 1 year at which time the rate of change of degree of hydration is expected to be minimal. Accordingly, variations in pore size distribution or porosity is also considered to be minimal and hence neglected beyond the curing period. Similarly, the pore network model considers laboratory temperature reported in Table 2-1 in order to correctly interpret temperature dependent RH changes.

Table 2-1. Materials studied (CP: cement paste; M: Mortar; Co: concrete).

Material	C <sub>3</sub> S	C <sub>2</sub> S	C <sub>3</sub> A	C <sub>4</sub> AF	W/C	Aggregate/Cement	Experimental conditions	Experimental technique
CP1	56.5	18	6.3	11.4	0.45	-	Immersion in limewater for 56 days	Drying progressively for 270 days using ASTM C157, T=25 ± 0.2
CP2	57.28	23.98	3.3	7.6	0.34	-	1 year old specimen without water exchange, vacuum rewetted for drying	Drying controlled by saturated salt solutions, T=21±0.5°C
CP3	44.61	37.14	10.56	7.7	0.35	-	Endogenous curing conditions for 1 year	Drying controlled by saturated salt solutions, T=20°C
CP4	65.84	22.72	3.25	8.19	0.45	-	Same as CP3	Same as CP3

Chapter 2 - A Multiscale Framework to Estimate Water Sorption Isotherms for OPC-based Materials

CP5	17.53	54.67	13.4	14.4	0.5	-	Immersion in limewater for 5 months	Climatic chamber, T=20±1 °C
CP6	17.53	54.67	13.4	14.4	0.8	-	Same CP5	Same CP5
M1	62.74	17.39	7.92	11.95	0.5	3.03	Same as CP3	Same as CP3
M2	17.53	54.67	13.4	14.4	0.5	3	Same as CP5	Same as CP5
M3	17.53	54.67	13.4	14.4	0.8	3	Same as CP5	Same as CP5
Co1	74.27	9.66	0.74	15.33	0.45	4.5	Same as CP3	Same as CP3
Co2	32.43	44.54	12.39	10.55	0.40	4.46	Same as CP3	Same as CP3

Table 2-2. Results from VCCTL and Jennings-Tennis's hydration model (CP: cement paste, Co: concrete, M: Mortar): All % values are rounded.

Material	W/C	C-S-H in cement paste (%)	HD C-S-H in C-S-H gel (%)	LD C-S-H in C-S-H gel (%)	HD C-S-H Porosity (%)	LD C-S-H Porosity (%)	Capillary Porosity (%)
CP1	0.40	51	54	46	7	9	21
CP2	0.34	45	64	36	7	6	10
CP3	0.35	45	70	30	8	5	15
CP4	0.45	44	40	60	4	10	25
CP5	0.5	47	28	72	3	13	37
CP6	0.8	49	22	78	3	14	47
M1	0.5	40	28	72	3	11	25
M2	0.5	44	28	72	3	12	16
M3	0.8	39	28	72	3	10	18
Co1	0.45	40	42	58	4	9	10
Co2	0.40	45	43	57	5	9	14

### 2.5.1 Influence of capillary pores

Recall from Section 2.3 that a crude approach was proposed to account for the missing capillary pore size distribution in the range 14 nm to 1  $\mu\text{m}$ . To justify this approach, the influence of capillary pore size range on WSI is examined in this section with the help of a series of virtual experiments. A network including C-S-H gel pores with evenly distributed HD and LD pores (50% HD C-S-H, 50% LD C-S-H) is generated, following which a capillary network is added. Influence of variation of the mean pore size of the added capillary network and its volume fraction are then studied. The volume fraction of the capillary network varies from 40% of the total porous phase (Eq.2-1) to 70% and four different mean pore sizes are considered: 0.1  $\mu\text{m}$ , 0.5  $\mu\text{m}$ , 1  $\mu\text{m}$  and 10  $\mu\text{m}$ . The predicted WSI for such networks with 40%, 50%, 60% and 70% of volume fraction of capillary porosity is presented in *Figure 2-10*. It is seen that as the volume fraction of capillary porosity increases, the effect of its pore size range becomes slightly more pronounced. For example, the network with 40% capillary pores and mean capillary pore size of 10  $\mu\text{m}$  has a maximum deviation of 6% compared to a network with mean capillary pore size of 0.1  $\mu\text{m}$ . Whereas, the same comparison for a network with 70% capillary pores has 9% deviation. Although the difference of 3% does not seem to be a big deviation, these networks are constructed in an ideal sense where the proportion of HD and LD C-S-H is fixed. In reality, higher porosity means either higher W/C or lower hydration degree and consequently higher percentage of LD than HD C-S-H, which shifts the whole retention curve.

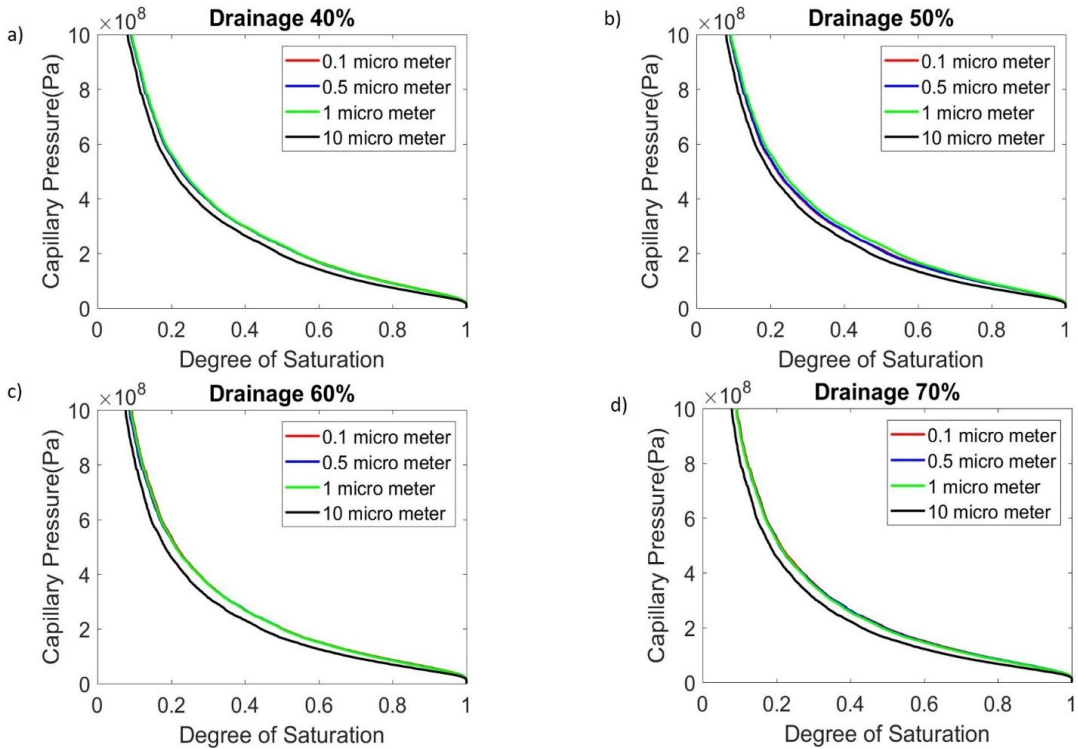


Figure 2-10. Comparison of drainage curves for networks with different volume fraction of capillary pores and four different mean capillary pore sizes. (a) 40% capillary pore, (b) 50% capillary pore, (c) 60% capillary pore, and (d) 70% capillary pore.

However, an important conclusion from Figure 2-10 is that the capillary pore size distribution and capillary pore size range (> 14 nm) do not significantly affect WSI. At least three reasons can be attributed to this insensitivity:

- a) The population of capillary pores are at least two orders of magnitude lower than gel pores to have any pronounced effect. For example, for the material CP5, the calculated volume fraction of C-S-H gel is 47% (of which 72% is LD and 28% is HD C-S-H) and that of capillary porosity is 37% (Table 2-2). The 47% C-S-H gel fraction with aforementioned LD

and HD C-S-H ratios results in 13% of LD C-S-H gel pores and 3% of HD C-S-H gel pores. This distribution results in 1 million LD C-S-H pores and 1.28 million HD C-S-H pores. In contrast, the calculated capillary pores are only 23,552 in the total pore space.

- b) From Eq. (2-10), the relative humidity at which a pore radius of 20 nm ( $T=293$  K) is invaded is 0.95. Whereas, a big capillary pore with a radius of  $10 \mu\text{m}$  is invaded at a relative humidity of 0.99. Because of this narrow range of relative humidity covering the whole range of capillary pores, the invasion sequence is not considerably affected to significantly influence WSI.

$$r_p = -\frac{2\gamma}{\left(\frac{RT}{M}\right) \ln RH} \quad (2-10)$$

- c) In addition, because of the random distribution of capillary pores as well as its smaller population in the overall pore network, the invasion sequence is not considerably affected. For example, not all the capillary pores are exposed to air once the relative humidity reaches 0.95 because some of them are trapped between the gel pores.

Therefore, the crude approach proposed in Section 2.3 to handle the missing pore size distribution in the pore size range of 14 nm to  $1 \mu\text{m}$  is justified, at least for predicting WSI.

### 2.5.2 WSI predictions

Based on the material composition defined in Table 2-1, predicted phase fractions of C-S-H and the porosity of LD C-S-H, HD C-S-H and capillary pores are presented in *Table 2-2*, which form basic inputs for generating pore networks.

The results show that the capillary porosity and volume fraction of LD C-S-H increase with increase in W/C and the volume fraction of HD C-S-H shows opposite trend (*Table 2-2*). The results also show that the capillary porosity of cement paste is larger than that of concrete for the same W/C. All these are qualitatively consistent with the known behaviour of OPC [59].

*Figure 2-11* to *Figure 2-13* show comparisons of experimental WSI against the pore network model results for the materials mentioned in *Table 2-2*. It is seen that for all materials the model provides reasonably good correlation. The accuracy in the lower saturation regime is considerably higher than the rest of the curve, revealing that the C-S-H gel has a reproducible behaviour and its variation is more limited than capillary pores. However, there are some deviations for materials CP2, Co1 and Co2, which may be attributed to uncertainties in the composition of the materials used in the experiments as well as the idealizations and assumptions in the particle packing and pore network model. Nevertheless, it is reasonable to conclude that the particle packing model provides reliable inputs for pore network modelling.

For the materials CP1, CP3, CP5, M2, Co1 and Co2, the model slightly underestimates WSI in the mid-range saturation regime. Part of the reasoning is the same as mentioned above for lower  $S_l$ , but in addition, the reliability of the pore size distribution extracted from the hydration kinetics model is also a major factor. Recall from Section 2.2 that the existing hydration kinetics models are not intended to capture pore size distribution and is admitted only as a first approximation in this study.

Furthermore, note that CP5 and M2 are from the same dataset where a standard for cement type used is reported but XRD information of the chemical composition is not available. Co1 and Co2 are concrete (cement paste + aggregate) and the ability of hydration models to account for the presence of

aggregates is yet to be examined. Finally, CP1 is a one year old sample, which means self-desiccation would have occurred, which is not considered in the present framework. The above issues add further uncertainties, which are

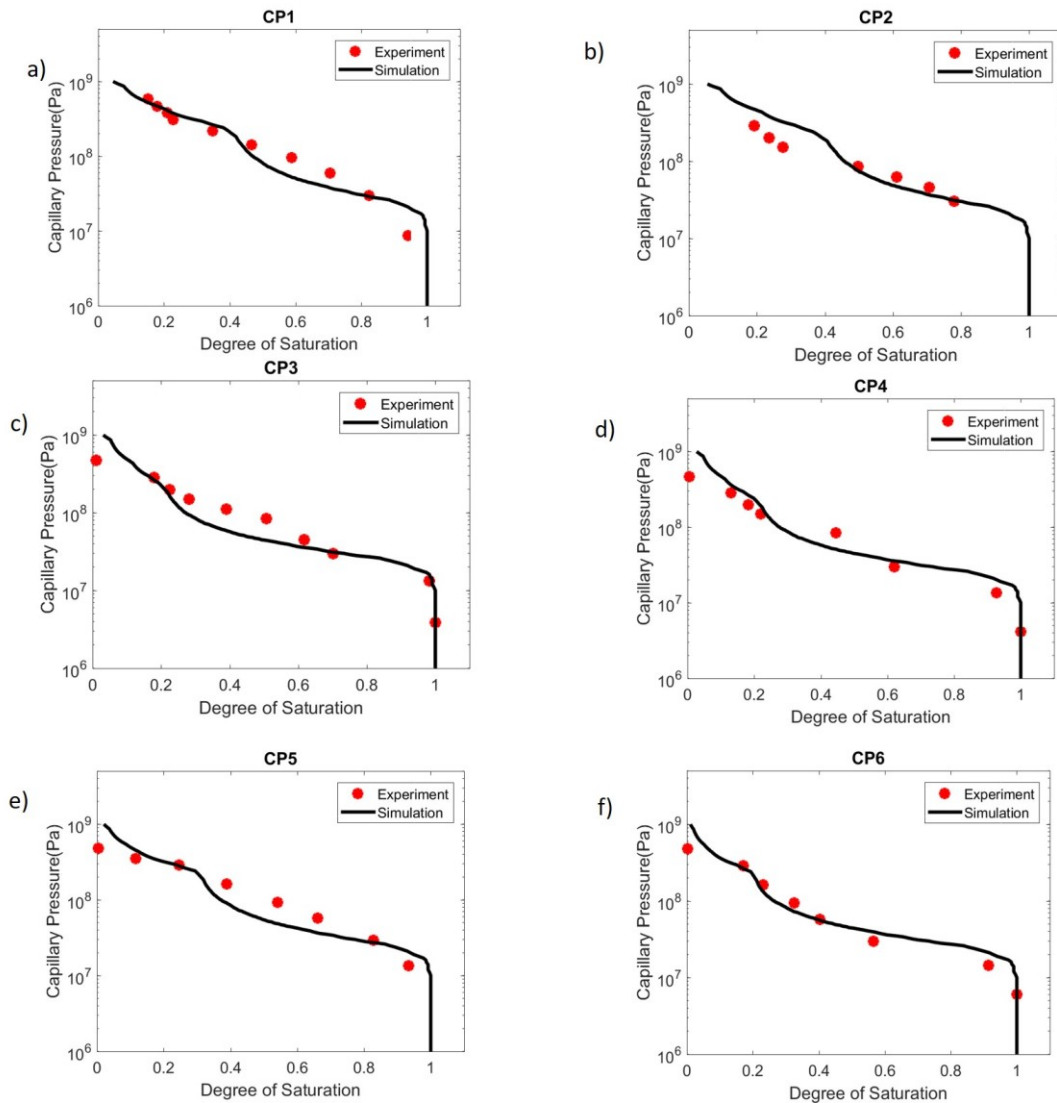


Figure 2-11. Experimental observations vs. simulation using the pore network model. (a) CP1, (b) CP2, (c) CP3, (d) CP4, (e) CP5 and (f) CP6.

reflected in the marginal deviations observed in the predicted WSI.

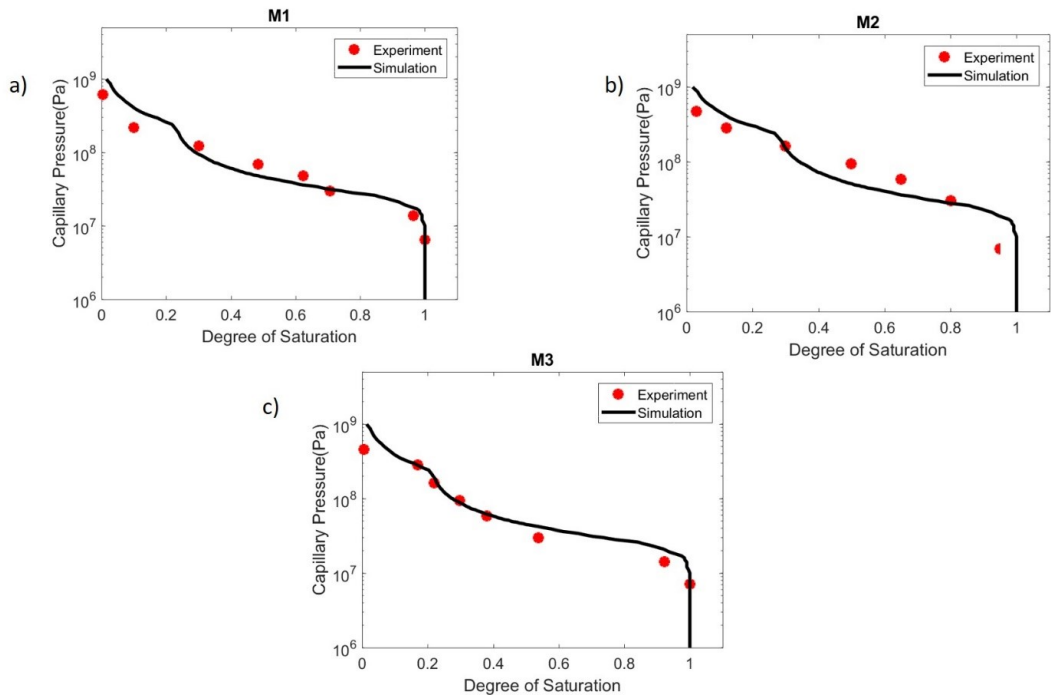


Figure 2-12. Experimental observations vs. simulation using the pore network model. (a) M1, (b) M2, (c) M3.

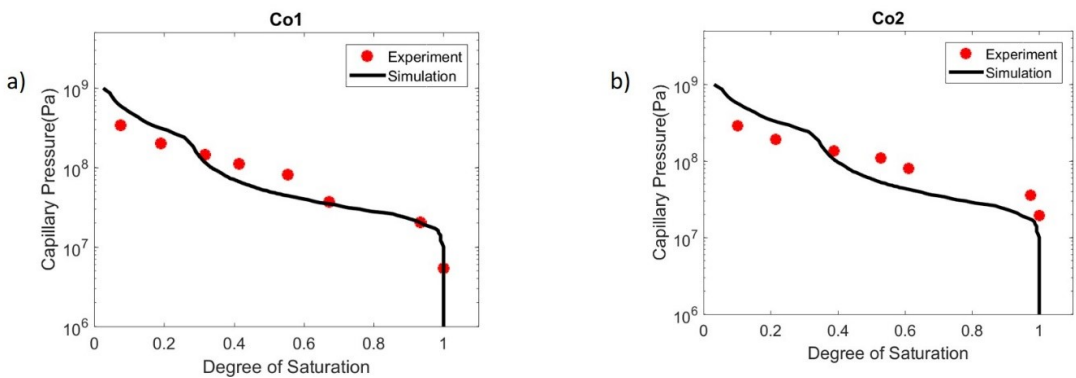


Figure 2-13. Experimental observations vs. simulation using the pore network model. (a) Co1, and (b) Co2.

Table 2-3 shows that  $R^2$  value (coefficient of determination [68]) is 0.85 or above for the studied cases. Given the available tools and assumptions, the overall performance of the multiscale framework is highly encouraging.

Table 2-3.  $R^2$  (coefficient of determination) values for the predicted desorption curves.

<i>Material</i>	$R^2$ value
<i>CP1</i>	0.94
<i>CP2</i>	0.88
<i>CP3</i>	0.92
<i>CP4</i>	0.95
<i>CP5</i>	0.92
<i>CP6</i>	0.95
<i>M1</i>	0.94
<i>M2</i>	0.92
<i>M3</i>	0.94
<i>Co1</i>	0.93
<i>Co2</i>	0.85

## 2.6 Conclusions

A largely predictive multiscale framework for the estimation of WSI is proposed. This is achieved by integrating the following models: (i) particle packing, (ii) cement hydration kinetics, and (iii) pore network. The need for predicting pore size distribution necessitates the use of particle packing and cement hydration models, including Jennings-Tennis's model to obtain additionally the HD-LD C-

S-H ratio. Based on the predicted (complete) pore size distribution of the material, the merging of HD C-S-H, LD C-S-H and capillary pore networks has been proposed, which actually leads to a very large pore network with few millions of pore bodies and throats. Both capillary water and adsorbed water are considered in estimating water content for WSI calculations. The pore network is implemented in the SciPy and NumPy computational environment with recourse to an existing library called OpenPNM, which uses an efficient invasion algorithm. A quasi-static analysis of the network using Kelvin's equation is then invoked in pore bodies and throats to estimate desorption WSI, the latter because the ultimate goal of this study is to address drying shrinkage problem.

The capability of the framework has been demonstrated with eleven independent experiments available from literature. A reasonably good correlation with experimental WSI has been demonstrated for all the experiments, with deviations explained. In fact, the  $R^2$  value is equal to or above 0.85 for any of the comparisons. It is important to note that calibrations primarily stem from the cement hydration kinetics and Jennings-Tennis's model, which are usually based on hydration experiments for OPC based materials. Secondly, for the particle packing model, the knowledge of the particle size and packing density is required, which also comes from experimental investigations. From the pore network model perspective, only one calibration parameter exists, which is related to the throat size, and can be calibrated on any one experimental WSI. This framework therefore allows a greater flexibility to study WSI behaviour of arbitrary OPC based materials. Note that if experimental pore size distribution is available then the pore network model is solely sufficient to estimate WSI. One of the main advantages of using pore network modelling is that it is not only useful for WSI (including hysteresis) but also for estimating liquid permeability and vapour diffusivity of cementitious materials. Hence, the proposed work is a

promising approach to address many hydraulic parameters for moisture transport studies within a single framework.

Finally, it is acknowledged that there are shortcomings in the models used in the proposed framework. For instance, uncertainties associated with the chosen cement hydration kinetics model, the missing pore size distribution because of the limitation of model resolution of the cement hydration kinetics model and the applicability of Jennings-Tennis's model for arbitrary OPC based materials.

### **3 An Analytical Framework for Estimating Drying Shrinkage Strain of OPC Based Hardened Cement Paste**

---

Based on ‘An analytical framework for estimating drying shrinkage strain of OPC based hardened cement paste’

Babaei S., Seetharam S.C., Dizier A., Steenackers G., Craeye B.

Published in: Cement and concrete composites - ISSN 0958-9465 - 115(2021)  
[doi: 10.1016/J.CEMCONCOMP.2020.103833](https://doi.org/10.1016/J.CEMCONCOMP.2020.103833)

#### **3.1 Introduction**

## Chapter 3

For massive civil engineering concrete structures, the drying shrinkage strain is usually neglected because water exchange with the surrounding environment is very slow and mostly its effect such as cracking is limited to a thin outer layer of the structure [15]. Moreover, in massive structures, peak temperature due to heat of hydration remains only for a few days thus limiting any adverse effect on drying rate [69]. However, this may not necessarily be the case in applications related to massive non-reinforced concrete engineered barriers for deep geological disposal of radioactive waste [70, 71]. In particular, the so-called Supercontainer concept currently under consideration in Belgium, encapsulates within a concrete buffer, high-level radioactive waste (HLW) materials that release decay heat over hundreds of years. Depending on the type of waste, temperatures can reach 100 °C at the interface between the HLW canisters and concrete buffer [72], with an increased tendency to initiate a severe drying front at the interface and further into outer layers of the buffer. Therefore, the knowledge of drying shrinkage strain in the entire relative humidity ( $h$ ) range becomes necessary. This is in addition to the contribution from other eigenstrains

such as thermal and creep strains. In such applications, optimum choice of cement formulation at the design phase is essential and hence *a priori* knowledge of drying shrinkage strain would be a valuable input for numerical assessment of thermo-hydro-mechanical (THM) behaviour of structural concrete. Therefore, an approach that allows *a priori* estimation of drying shrinkage strain of hardened cement paste from the knowledge of cement composition and microstructural characteristics of the material paves a way forward for better understanding of the cracking potential of cementitious components or structures. Such an exercise is not limited to the aforementioned application alone but to other situations where drying shrinkage cracking is a problem, which underlines the necessity the importance and renovation of this framework.

The development of predictive models for drying shrinkage strain has significantly advanced in the last half a century (e.g. [13, 73-76]). The basis for most of the advanced approaches rely on the idea of multiple mechanisms operating at different pore scales (Powers [77], Brochard et al. [78], Vandamme et al. [79], Pinson et al., [36] , Luan and Ishida [80], Nguyen et al. [81]) and importantly the approaches are relevant for reversible drying shrinkage strains only. The commonly adopted multiple mechanisms approach was in fact originally put forward by Powers [77], who presented a thermodynamic analysis of volumetric shrinkage strain of hardened cement paste attributable to solid surface tension or surface free energy (Eq. 12 in [75]), disjoining pressure (Eq. 17 [80]) and capillary pressure (Eq. 19 in [21]), but only included qualitative examples of individual volumetric strains. Their thermodynamic analysis essentially relates change in Gibb's free energy to water content in different pore classes via Kelvin's law and involves only one unknown constant in the disjoining pressure equation. A fundamental input is the water content in different pore classes: (de)sorption isotherm is the basis for this type of analysis and all similar approaches discussed further. Furthermore, they argue that the

capillary pressure term represents the combined effect of both disjoining and capillary pressure for capillary pore range, but capillary pressure is not applicable for lower humidity range ( $\sim <0.45$ ), where only disjoining pressure is dominant. In what follows, particular attention is paid to the state of the art multi-mechanisms models for reversible drying shrinkage strain similar to that of Powers [77].

Coussy [75] showed that the capillary pressure alone cannot capture observed total volumetric strain of hardened cement paste and thus introduced an additional interfacial energy term, whose value increases with decrease in  $h$ . However, they conclude that their macroscopic approach of combining capillary pressure and interfacial energy fails to capture the macroscopic strain below relative humidity of 50-40%. Luan and Ishida [80] and Rezvani [21] used a multi-mechanism approach similar to Powers [77], in which they consider contribution of shrinkage strains from capillary pressure and disjoining pressure only. In particular, Luan and Ishida [80] argue that the effect of surface energy is only relevant at very low  $h$  and that the change in disjoining pressure can be regarded as being equivalent to the change in surface energy at complete desorption. They demonstrate excellent agreement with measured uniaxial shrinkage strains for cement paste at two W/C ratios. Pinson et al.[36] also follow similar idea as Powers [77] by proposing three mechanisms operating at three pore classes (capillary, gel and interlayer) to capture total reversible shrinkage strain. Unlike Powers [77] who considers a thermodynamic relationship for the shrinkage contribution due to disjoining pressure, Pinson et al. [36] use a molecular approach plus a calibration factor to capture the shrinkage strain contribution from the interlayer water. They also demonstrate a good agreement with desorption experiment although their approach predicts a transitory swelling upon drying between about 30% and 20% RH. More recently, Nguyen et al. [81] proposed a multi-mechanism drying shrinkage approach

similar to Powers [77]. Starting from Gibb's free energy equation, they derive a three-term equivalent pore pressure equation representing shrinkage contribution from capillary pressure, surface free energy and disjoining pressure, which are then embedded within a poroelastic theory to estimate the shrinkage strain. Note that their equivalent pore pressure is not the same as Coussy [75], where only capillary and interfacial energy is considered. Two calibration factors enter their drying shrinkage equation, one for the surface energy and the other for disjoining pressure and it appears that they need to be calibrated for each material. They show excellent correspondence with experimental results for Portland cement (CEM I) cement for two different W/C ratios of 0.3 and 0.47. Finally, an interesting approach, which does not belong to the afore mentioned multi-mechanism approaches, is that of Vlahinić et al. [24] who proposes a constitutive model for drying of an elastic porous material based on the Bishop [82] effective stress theory. In their approach, instead of pressure averaging, they consider weakening of the solid as a function of drying (degree of saturation). They also show an excellent agreement against a second cycle drying experiment on a 56-day-old cement paste sample. However, their model is valid under conditions where solid surface energy does not play an important role in deformation and where capillary pressure is dominant, in other words,  $h$  values above about 50% for hardened cement paste.

In conclusion, the validity of the multi-mechanism approach and the importance of sorption isotherm is sufficiently justified for drying shrinkage predictions. Keeping in mind the intended objective, which is to estimate drying shrinkage behaviour from cement composition, the study presented in this paper deviates from the aforementioned literatures in the following aspects:

- i. A multiscale water (de)sorption isotherm framework (WSI) is invoked to estimate water content in different pore classes [3].

- ii. An analytical homogenization approach principally based on Christensen [83, 84] is implemented to evaluate both the solid and bulk effective modulus of hardened cement paste (Section 3.2.2).
- iii. A reversible drying shrinkage formulation is adopted comprising the Biot-Bishop's poroelasticity [82, 85], Bangham's relationship [36, 86] and Power's thermodynamic relationship [77].
- iv. The role of microstructure on irreversible shrinkage strain is explored resulting in a phenomenological model that should be seen as a first approximation (Section 3.3.4.2).

The performance of the analytical framework is examined against a wide variety of drying shrinkage tests from literature, where complete data are available.

## 3.2 Analytical framework

An analytical framework for estimating drying shrinkage strain of hardened cement paste is implemented by combining existing approaches/models as follows (Figure 3-1):

- i. An existing cement hydration kinetics model, Virtual Cement and Concrete Testing Laboratory (VCCTL), is used to estimate degree of hydration and volume fractions of Portlandite, C-S-H and capillary porosity based on the initial composition of the material. With the resultant degree of hydration, the volume fractions of high density (HD) and low density (LD) C-S-H is estimated via Jennings-Tennis's hydration model [58]. Depending on the ratio of HD and LD C-S-H, the porosity of the gel pore space is also derived ([3]). These volume fractions are used in estimating effective bulk modulus of the material (step (iii) below).

- ii. A recently developed multiscale framework for estimating water desorption isotherm (WSI) [3] based on an integration of a number of models, which also includes step (i) above. This is the fundamental input necessary for computing drying shrinkage strain of the material for all the mechanisms considered.
- iii. An existing analytical homogenization scheme is invoked to compute effective bulk modulus of the material based on inputs from (i) above. This parameter is an essential input for the unsaturated poromechanics theory to compute drying shrinkage strain due to capillary forces.
- iv. An existing approach to estimate drying shrinkage strain principally based on the multi-mechanism approach proposed by Powers [77], which is based on thermodynamic equilibrium. The basic premise is that the total drying shrinkage strain can be attributed to a number of co-existing forces such as capillary, surface tension and disjoining pressure that operate at different relative humidity ranges, which are directly associated with the underlying pore size heterogeneity.

Of the above, only (iii) and (iv) are described in detail, whereas (i) and (ii) have already been dealt with in [3] but briefly covered in Section 3.3.

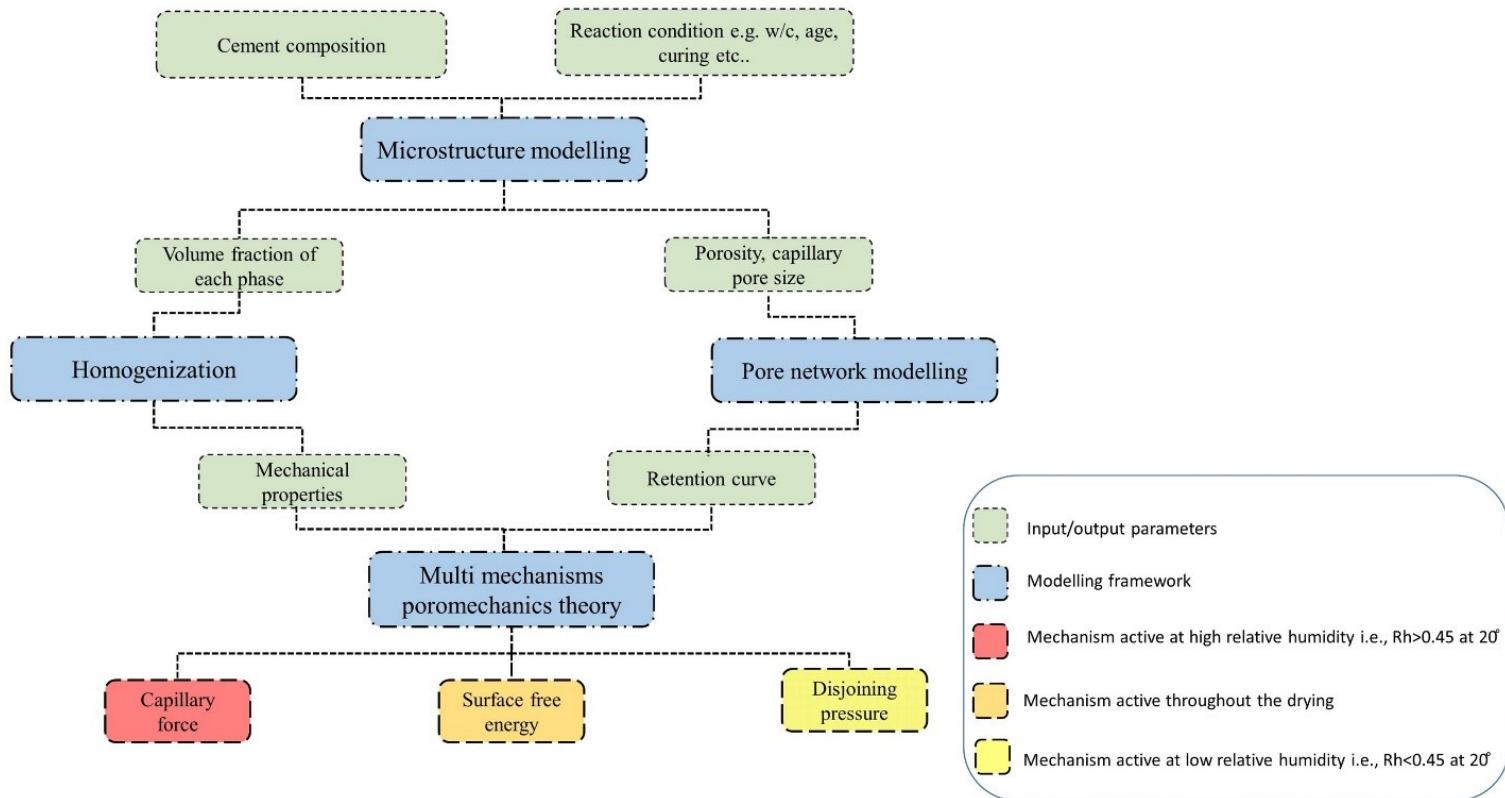


Figure 3-1. Analytical framework for estimating drying shrinkage strain.

### 3.2.1 Desorption isotherm from a multiscale approach

Babaei et al. [3] presented a multiscale framework to estimate desorption isotherm via the integration of the following models: (i) particle packing, (ii) cement hydration kinetics, and (iii) pore network. The first two models provide inputs for constructing pore size distribution as well as volume fractions of various pores, viz., gel (HD C-S-H, LD C-S-H) and capillary pores. The pore network model uses Kelvin's equation to determine distribution of equilibrium water content in the network for different increments of capillary pressure,  $P_c$ , in other words, the desorption isotherm for a given cement paste. For the shrinkage strain due to capillary forces, the desorption isotherm (i.e.  $P_c$  vs.  $S$ ) provides direct input as required by Equation (3-7). For the shrinkage strain due to surface tension, the pore network model not only provides equilibrium volumetric water content ( $\theta$ ) as a function of  $P_c$  (or  $h$ ), but also the volume of empty pores with surface adsorbed water, which is needed to compute  $\sigma$  as surface area of emptied pore per volume of porous material in Equation (3-10). For the disjoining pressure, the pore network model provides equilibrium water content (weight),  $w_d$  in pores smaller than 2.75 nm as a function of  $P_c$  (or  $h$ ) (i.e. for  $h < 0.45$ ) as required by Equation (3-12).

### 3.2.2 Effective bulk modulus from analytical homogenization

The effective bulk modulus of cement paste,  $K_b$ , is estimated using an analytical homogenization approach proposed by Christensen [83, 84] for two-phase material, which is based on Hashin's [87] composite spheres assemblage (CSA)

model. The above can be generalized to a multiphase system as shown in Xi and Jennings [76].

$$K_{s,eff} = K_{s,i} + \frac{s_{i-1,1}[(K_{s,eff})_{i-1} - K_{s,i}]}{1 + (1 - s_{i-1,1}) \frac{(K_{s,eff})_{i-1} - K_{s,i}}{K_{s,i} + \frac{4}{3} G_i}} \quad (3-1)$$

where  $K_{s,i}$  and  $G_i$  are the bulk and shear modulus of different phases, respectively, and  $s$  is the volume fraction defined as:

$$s_{i-1,i} = \frac{\sum_{j=1}^{i-1} f_j}{\sum_{j=1}^i f_j} \quad \text{from } i = 2 \text{ to } i = N - 1 \quad (3-2)$$

$$s_{N-1,N} = 1 - f_N$$

$f_i$  is the volume fraction of phase  $i$  such that:

$$\sum_{j=1}^N f_j = 1 \quad (3-3)$$

The homogenization sequence is illustrated in Figure 3-2. The first step computes effective bulk modulus of C-S-H gel by considering HD C-S-H and LD C-S-H as the two phases. The effect of gel pores in these phases are reflected in their stiffness values. The second step computes the effective bulk modulus of cement paste by considering a three-phase system: homogenized C-S-H gel obtained from the first step, Portlandite plus other crystalline hydration products, and the anhydrous cement grains.

The effective bulk modulus of solid skeleton is calculated using the abovementioned technique but to calculate the bulk modulus of porous structure, i.e. including capillary pores, Hashin and Shtrikman [88] found the effective bulk modulus for two-phase composite where voids are considered as a separate phase as follows:

$$K_b = K_{s,eff} \left( \frac{1 - \varphi_c}{1 + \varphi_c} \right) \quad (3-4)$$

Equation (3-4) was further modified as [77]:

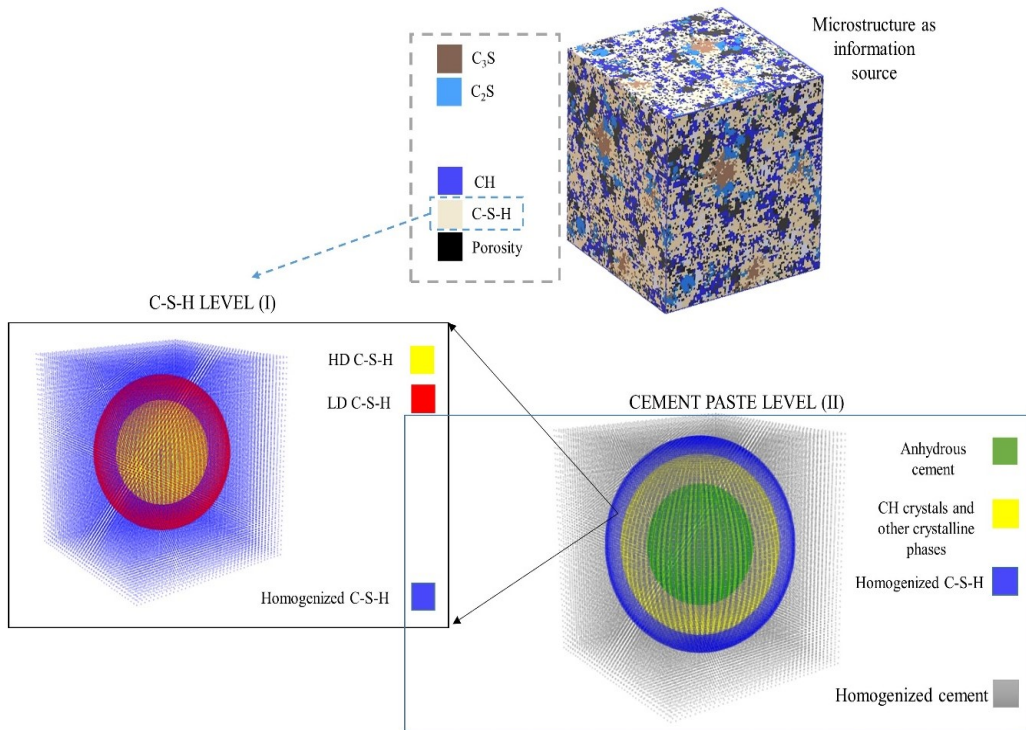


Figure 3-2. Generalized Homogenization method with its different levels.

$$K_b = K_{s,eff} (1 - \varphi_c)^2 \quad (3-5)$$

where  $\varphi_c$  is the capillary porosity.

### 3.2.3 Drying shrinkage

Based on the proposal by Powers [77], the total shrinkage strain in pure OPC material may be attributed to three main mechanisms [77, 89, 90]:

- i. **Capillary forces:** Capillary water in pores are in a state of tension, which results in compressive stress in the solid phase, thus causing shrinkage of the material (Powers [90]). Powers [77] reasoned that capillary water cannot exist at  $h$  lower than approximately 0.45 because at this humidity only pores roughly above 2.6 nm will be de-saturated (or in equilibrium with  $h=0.45$ ) on the basis of Kelvin-Laplace's equation. However, pores below 2.6 nm will be under the influence of strong interfacial forces (see point (iii) below) such that capillary menisci cannot be formed. Hence, the capillary-condensation theory is not valid anymore to estimate the drying shrinkage strain due to capillary forces. Therefore, shrinkage strain due to capillary forces ( $\epsilon_{vc}$ ) is postulated to operate in the relative humidity range 0.45 to 1.
- ii. **Solid surface tension:** Adsorption or desorption of water molecules on the surface of hardened cement microstructure is accompanied by a change in surface tension or equivalently surface free energy of the material. More specifically, there will be a decrease in energy during adsorption and an increase in energy during desorption. It is well documented that this change of energy is accompanied by volumetric strain (e.g. [91-93]). It is possible to relate the change in surface free energy to the change in vapour pressure by means of Gibb's equation ([86], [77] and [91]) and thus to the volumetric strain. Shrinkage strain due to solid surface tension ( $\epsilon_{vs}$ ) is postulated to operate in the entire

relative humidity range of 0 to 1. This assumption is reasonable because at any given humidity there will always be pores that will have adsorbed layer of water in a given representative volume element. Note that both Feldman and Sereda [91] and Pinson et al. [36] also consider it to be operative in the entire relative humidity range. It is however unclear if Powers [77, 89] considered the contribution of surface tension to the drying shrinkage strain above  $h=0.45$ .

- iii. ***Disjoining pressure:*** In the specific case of overlapping interfacial regions such as a thin layer of adsorbed water between two solid surfaces, the difference in the hydrostatic pressure of the adsorbed water in the interlayer and contiguous bulk water from which the adsorbed water phase was formed is referred to as the disjoining pressure [94, 95], and it is a function of thickness of the interlayer, and  $RH$  and temperature of the surrounding environment. For the disjoining pressure to be non-zero, the distance between the two solid surfaces must be less than a certain threshold value. For the case of hardened cement paste, Powers [77] estimated this value to be around 2.6 nm. He also estimated the mean inter-particle distance for the gel pores to be roughly 1.3 nm, which implies that the disjoining pressure can be active in majority of the gel pore space. This also implies that in this pore space, van der Waals attractive forces dominate giving rise to compressive forces between opposite surfaces, which are counter balanced by the disjoining pressure and the compressive stress of the solid phase (Powers, 1968 [89]). Therefore, it is imperative that any loss of water in the pore space due to drying is likely to result in shrinkage of the material. In light of the reasoning in point (i) above, the volumetric shrinkage strain due to

disjoining pressure ( $\varepsilon_{vd}$ ) is postulated to operate in the relative humidity range 0 to 0.45.

In the absence of external load and generally observed small strain (Pinson et al. [36]), the total reversible volumetric drying shrinkage strain ( $\varepsilon_{v,r}$ ) can be mathematically expressed as:

$$\varepsilon_{v,r} = \varepsilon_{vc} + \varepsilon_{vs} + \varepsilon_{vd} \quad (3-6)$$

### 3.2.4 Shrinkage strain due to capillary forces ( $0.45 < h < 1$ )

Assuming pore air pressure ( $u_a$ ) to be significantly smaller than pore water pressure ( $u_w$ ),  $\varepsilon_{vc}$  can be derived from the Bishop's "single effective stress" constitutive equation [82, 96] :

$$\varepsilon_{vc} = \frac{\chi P_c \alpha_B}{K_b} \quad (3-7)$$

$$\alpha_B = \left(1 - \frac{K_b}{K_s}\right) \quad (3-8)$$

$$P_c = (u_a - u_w) = \frac{RT}{M v_w} \ln(h) \quad (3-9)$$

where  $\chi$  is the Bishop's effective stress parameter taken as equal to the degree of water saturation ( $S_l$ ),  $\alpha_B$  is the Biot's coefficient,  $P_c$  is the capillary pressure (Pa),  $K_b$  is the bulk modulus of the skeleton (Pa) and  $K_s$  is the bulk modulus of the solid phase (C-S-H) (Pa),  $R$  is the gas constant (J/mol/K),  $T$  is the temperature (K),  $M$  is the molar mass of water (g/mol),  $v_w$  is the specific volume of water ( $\text{m}^3/\text{kg}$ ).

Especially, within the geomechanical/geotechnical community there are numerous discussions on  $\chi$  as well as applicability of single effective stress approach, which is beyond the scope of this paper. Readers are referred to reviews by Jennings and Burland [97] and Nuth and Laloui [98] concerning the single effective stress approach for partially saturated soils and the difficulties in measuring a unique value of  $\chi$ , and Vlahinic et al. [24] concerning the derivation and interpretation of  $\chi$  from micro-poromechanics. Nevertheless, Eq. (3-7) has been successfully applied by Di Bella et al. [99] and appears to be fairly accurate for second cycle (or reversible part) of drying but only at  $h > 0.5$ .

### 3.2.5 Shrinkage strain due to solid surface tension ( $0 < h < 1$ )

This study is similar to Pinson's [36] approach, which is essentially the Bangham equation [86] that describes volumetric strain from change of surface tension (surface free energy),  $\varepsilon_{vs}$ :

$$\varepsilon_{vs} = \frac{\Delta(\sigma\gamma)}{K_b} \quad (3-10)$$

where  $\sigma$  is the surface area of emptied pores per volume of porous material, which unlike Pinson [36], is directly obtained from the pore network model.  $\gamma$  is the surface free energy of solid that is equal to additional surface tension of pore wall to the adsorbed water [36, 93] layer and it is computed via:

$$\gamma = \gamma_0 - \frac{RT}{M} \int_{h_0}^h \theta \frac{dh}{h} \quad (3-11)$$

where  $\gamma_0$  is the surface tension at  $h_0$ ,  $\theta$  is the volumetric water content of the surface adsorbed water.  $h=1$  is considered as the reference state with the corresponding surface tension set equal to the surface tension of bulk water.

### 3.2.6 Shrinkage strain due to disjoining pressure ( $0 < h < 0.45$ )

Based on a thermodynamic analysis, Powers [77] proposed an expression for the volumetric strain due to the disjoining pressure (Eq. (3-12)):

$$\varepsilon_{vd} = \kappa\beta' \frac{RT}{Mv_w} \int_{h_1}^{h_2} \frac{w_d}{V_s} d\ln(h) \quad (3-12)$$

where  $v_w$  is the molar volume of water,  $\beta'$  is the coefficient of compressibility of the material under sustained stress, which is taken as the inverse of bulk modulus of cement paste,  $K_b$  (Pa), and  $k$  is a constant of proportionality, which is taken as unity as a first approximation and  $w_d$  is water content in pores smaller than 2.75 nm.  $V_s$  is the volume of the adsorbent ( $m^3$ ) defined as:

$$V_s = V_p(1 - \varphi_t) \quad (3-13)$$

where  $V_p$  is the volume of cement paste and  $\varphi_t$  is the total porosity of the paste.

### 3.2.7 Other models for drying shrinkage strain

This study is particularly focused on estimating drying shrinkage strain based on multi-mechanism approach (Section 3.2 to 3.2.6). However, there are other approaches, in particular, the equivalent pore pressure approach of Coussy et al. [75] and effective bulk modulus approach of Vlahinic et al. [24] that captures

these mechanisms in a single framework. These are briefly covered in Appendix-A as the performance of the multi-mechanism approach will be compared with these single framework approaches.

### 3.3 Validation

The analytical framework is validated against a number of available experimental data that encompass total shrinkage strains with and without irreversible strains for various hardened cement pastes [33, 66, 100, 101]. The available experimental shrinkage strain is usually the ultimate shrinkage strain, which is an asymptotic value of the hyperbolic shrinkage strain equation as defined, for example, in ACI-209. Recall from Section 2-3 that the shrinkage strain equations (Equations (3-7), (3-10) and (3-12)) are based on thermodynamic equilibrium, which implies that the calculated strains are equilibrium values for a given  $RH$ , and hence can be directly compared with the experimental ultimate shrinkage strain. The shrinkage data are available for two types of materials: (i) non-virgin samples that were dried and rewetted to yield total shrinkage strains without irreversible strain component (samples CP1 to CP3), and (ii) virgin samples that were cured right after casting and kept saturated to yield total shrinkage strains, which include irreversible strain component (samples CP4 to CP9). Desorption isotherms are also available for these materials [100]. Recall that the drying shrinkage formulation in methodology is only able to estimate reversible shrinkage strain, but not the total shrinkage strain that includes irreversible strain. Nevertheless, the main purpose of comparing the predicted results with the shrinkage experiments of virgin samples is to (i) explore the extent of deviation between the predicted and measured values and (ii) to quantitatively evaluate the role of microstructure on

the irreversibility. The chemical composition, curing condition and experimental techniques of the materials (CP1 to CP9) are presented in Table 3-1.

Table 3-1. Chemical composition of the samples (% mass).

Material code	Material	W/C	C3S	C2S	C3A	C4AF	Curing method	Experimental method	Extent of drying of samples (RH)	Reference
CP1*	CEM II	0.50	0.21	0.53	0.10	0.15	Endogenous curing conditions for 1 year	Drying controlled by saturated salt solutions, T=20°C	0.25	[33]
CP2*	CEM II	0.80	0.21	0.53	0.10	0.15	Endogenous curing conditions for 1 year	Drying controlled by saturated salt solutions, T=20°C	0.30	[33]
CP3*	CEM I	0.45	0.56	0.18	0.06	0.11	Immersion in limewater for 56 days then dried for 270 days and rewetted for 28 days	Drying progressively for 270 days using ASTM C157, T=25 ± 0.2	0.45	[66]
CP4	CEM I	0.55	0.62	0.19	0.07	0.10	Saturated conditions for 91 days (100% RH)	Climate chamber with <i>h</i> control using sodium hydrate solution. T=20°C	0.2	[100, 101]

Chapter 3 - An Analytical Framework for Estimating Drying Shrinkage Strain of OPC Based Hardened Cement Paste

CP5	CEM I	0.40	0.62	0.19	0.07	0.10	same	same	0.2	[100, 101]
CP6	CEM I	0.55	0.42	0.38	0.04	0.12	same	same	0.2	[100, 101]
CP7	CEM I	0.40	0.42	0.38	0.04	0.12	same	same	0.2	[100, 101]
CP8	CEM I	0.55	0.24	0.62	0.02	0.08	same	same	0.2	[100, 101]
CP9	CEM I	0.40	0.24	0.62	0.02	0.08	same	same	0.2	[100, 101]

\* Babaei et al. [3]

### 3.3.1 Cement hydration kinetics

The results obtained from the cement hydration kinetics model, VCCTL [52], are presented in Table 3-2, which includes degree of hydration, volume fractions of Portlandite, C-S-H, and capillary porosity at the end of the respective curing periods.

Table 3-2 also includes the volume fractions of HD and LD C-S-H based on Jennings-Tennis's hydration model. Note that the results for the samples CP1-CP3 were already reported in Babaei et al. [3], but reproduced here for immediate reference. As expected, the models predict higher volume fractions of LD C-S-H, capillary porosity and final degree of hydration for compositions with higher water to cement ratio, which are qualitatively consistent with the known behaviour of OPC [46, 47, 58, 102].

Table 3-2. Results from the cement hydration kinetics model at the end of respective curing periods, including experimental data of shrinkage strains

Material code	W/C	Volume fraction LD-CSH	Volume fraction HD-CSH	Total C-S-H	Capillary porosity	Total porosity	DOH	Portlandite	Unhydrated Clinker	Other products	Limestone	Experimental		
												Ultimate shrinkage (m <sup>3</sup> /m <sup>3</sup> )	Irreversible shrinkage (m <sup>3</sup> /m <sup>3</sup> )	Irreversible/ultimate shrinkage
CP1*	0.50	0.28	0.10	0.38	0.21	0.31	0.85	0.11	0.06	0.04	0.10	-	-	-
												0.00372		
												1		
CP2*	0.80	0.32	0.05	0.37	0.33	0.42	0.95	0.10	0.02	0.02	0.07	-	-	-
												0.00514		
												4		
CP3*	0.45	0.27	0.23	0.50	0.17	0.28	0.82	0.12	0.06	0.05	-	-	-	-
												0.00296		
												0		
CP4	0.55	0.39	0.09	0.48	0.21	0.32	0.88	0.12	0.04	0.04	-	-	-	0.40
												0.00490	0.001709	
												6		

Chapter 3 - An Analytical Framework for Estimating Drying Shrinkage Strain of OPC Based Hardened Cement Paste

CP5	0.4	0.25	0.27	0.52	0.14	0.25	0.78	0.12	0.08	0.03	-	-	-	0.35
	0											0.00410	0.001219	
												6		
CP6	0.5	0.41	0.10	0.51	0.21	0.34	0.88	0.09	0.04	0.02	-	-	-	0.36
	5											0.00521	0.001804	
												0		
CP7	0.4	0.25	0.27	0.52	0.15	0.27	0.78	0.10	0.08	0.03	-	-	-	0.29
	0											0.00425	0.001189	
												5		
CP8	0.5	0.39	0.10	0.49	0.20	0.33	0.88	0.08	0.07	0.03	-	-	-	0.40
	5											0.00628	0.002673	
												2		
CP9	0.4	0.23	0.28	0.51	0.14	0.28	0.78	0.09	0.09	0.03	-	-	-	0.29
	0											0.00436	0.001312	
												6		

### 3.3.2 Water desorption isotherms

Based on the multiscale WSI framework of Babaei et al. [3], desorption isotherms for materials CP1 to CP9 are estimated Figure 3-3, Figure 3-4 and shows a comparison of predicted and experimental results of desorption isotherms for CP1 to CP3 and CP4 to CP9, respectively. Once again note that the results for CP1-CP3 were already discussed in Babaei et al. [3], but reproduced here for immediate reference. For materials CP4 to CP9, it is seen that the predicted

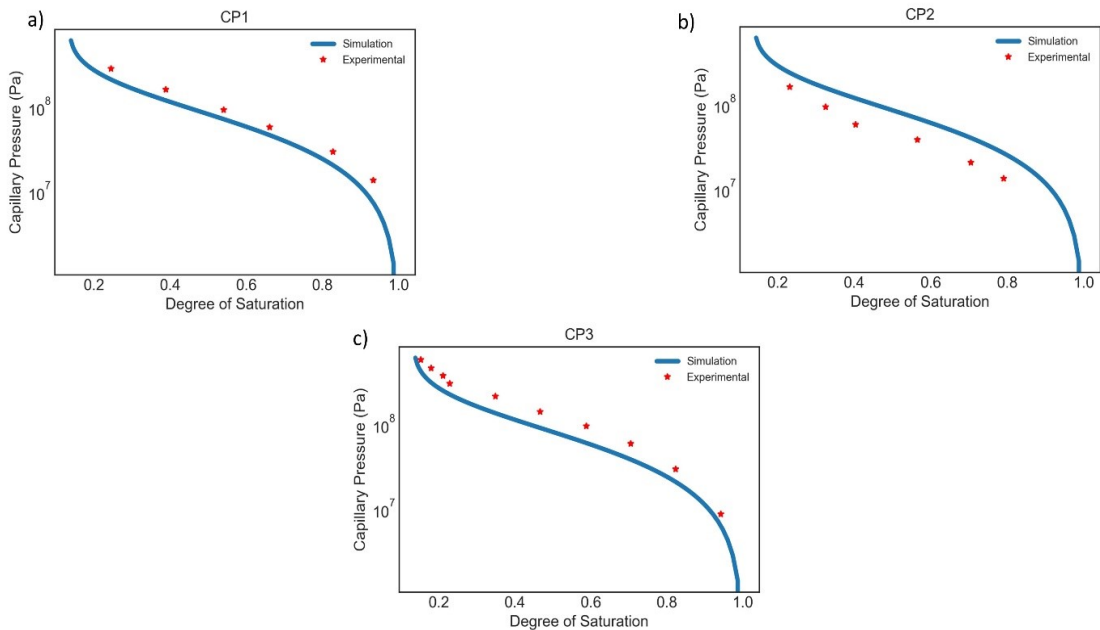


Figure 3-3. Estimated desorption isotherms for materials CP1-CP3 (previously reported in Babaei et al. [3])

results show reasonably good correlation with experimental results. The coefficient of determination ranges from 0.88 to 0.95 for predicted isotherm desorption curves. This increases confidence in the use of the multiscale WSI

framework. In other words, with the available knowledge of cement microstructure and the set of models used in the WSI framework, it is possible to arrive at the desorption isotherm directly from cement composition.

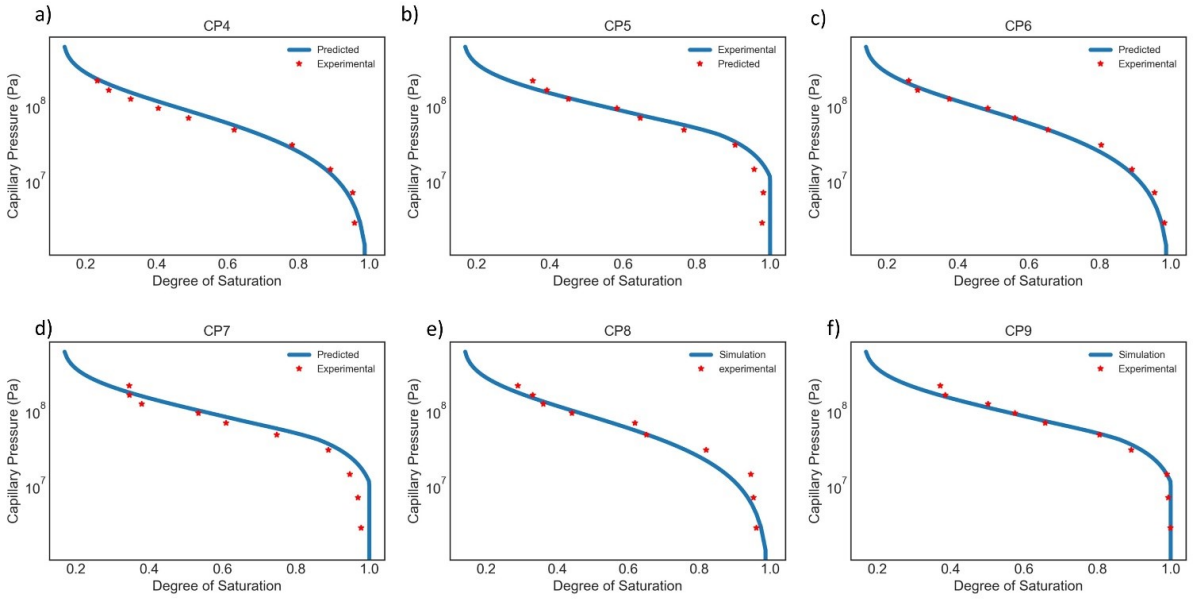


Figure 3-4. Estimated desorption isotherms for samples CP4-CP9 using Babaei et al. approach vs experimental data.

### 3.3.3 Effective bulk modulus

Based on the volume fractions of various hydration products and experimental data on Young’s modulus and Poisson’s ratio of individual phases of the cement paste (Table 3-2),  $K_b$  and  $K_s$  of the materials CP1 to CP9 are estimated as shown in Table 3-4.

With the exception of materials CP1, CP2 and CP8, the homogenization technique captures experimental  $K_b$  results well. The deviations in the case of CP1, CP2 and CP8 are attributable to the differences between the actual material and the microstructural model results, for instance, with respect to the volume fractions of various phases and ratio of LD and HD C-S-H.

*Table 3-3. Mechanical properties of hardened cement paste constituents [41, 45, 50, 103]*

	$E$ (GPa)	$\nu$ (-)
C-S-H Gel		
HD C-S-H	29.4±2.4	0.24
LD C-S-H	21.7±2.2	0.24
Cement Paste		
C <sub>3</sub> S	135	0.3
C <sub>2</sub> S	140	0.3
C <sub>3</sub> A	145	0.3
C <sub>4</sub> AF	125	0.3
CH	38	0.305
Other products	52	0.32

Table 3-4. Calculated bulk modulus vs experimental data.

Material code	Experimental bulk modulus ( $K_b$ ) (GPa)	Calculated Bulk modulus ( $K_b$ ) using proposed model (GPa)	Calculated solid bulk modulus ( $K_s$ ) using proposed model
CP1	10.5	11.52	18.5
CP2	6.0	7.50	16.6
CP3	12	12.20	17.4
CP4	11.0	11.85	18.9
CP5	13.8	13.67	18.48
CP6	11.0	11.27	18.05
CP7	12.4	12.61	17.45
CP8	9.27	10.34	16.25
CP9	12.8	12.02	16.10

### 3.3.4 Drying shrinkage strain

#### 3.3.4.1 Non-virgin material - reversible strain

Figure 3-5 (a)-(c) show a comparison of ultimate drying shrinkage strain of non-virgin materials (CP1 to CP3) as a function of degree of saturation. Note that for CP3, the experimental drying range is above  $RH=0.45$  (corresponding  $S_l=0.47$ ), where the disjoining pressure is postulated to be inactive, hence the shrinkage strain attributable to the disjoining pressure is zero. Overall, the predicted values show good correspondence with experimental data with coefficient of determination of 0.98, 0.91 and 0.99 respectively for CP1, CP2 and CP3,

although with a slight overestimation for CP1 and CP2 at very low degree of saturation. Even though the WRC for CP1 and CP3 are slightly less accurate, the drying shrinkage strains are reasonably well predicted. However, data concerning experimental uncertainty are not available to completely confirm the degree of accuracy. In relative terms, CP2 shows less overall accuracy based on the coefficient of determination (0.91). Note that CP2 has also the most unconventional composition i.e.  $w/c = 0.8$  and is a blended cement. The fundamental input for the construction of pore network originates from the cement hydration kinetics model, which provides volume fractions of various type of pores and hydration products; the latter also linked to the estimation of bulk modulus of the material. The accuracy of the microstructural model for such a blend relies on the extent of calibration (with isothermal calorimetric data) that have been performed with this unconventional material type, which could be one source of uncertainty. The consequence is that the predicted WRC is slightly less accurate in the entire range of degree of saturation. In addition, since CP2 has a lower strength compared to CP1 and CP3, there is a possibility that CP2 has higher microcrack density, which is not captured by the multi-mechanism model.

Figure 3-5(a)-(c) also shows contributions from the three shrinkage mechanisms. The general trend is that the contribution of surface free energy to the shrinkage strain is relatively less than the disjoining and capillary forces, but is still quantitatively important. The exception is however for CP2, where the contribution from surface free energy is more than the capillary forces. The exception is because the total porosity of CP2 is very high 0.47 ( $W/C=0.8$ ), which is directly accounted for in the  $\sigma$  term in the surface free energy (Equation (3-10)). Whereas, for the capillary force, the porosity is reflected in two properties: (i)  $K_b$  (Equation (3-5)), and (ii) desorption isotherm. Firstly, although  $K_b$  is important, it does not explain the difference even if the predicted  $K_b$  is replaced with experimental  $K_b$ . Secondly, the high porosity results in a

desorption isotherm that is characterized by lower capillary pressure for a given degree of saturation, compared to the materials with lower W/C ratios (CP1 and CP3). This results in a lower contribution from the capillary forces to the total shrinkage strain. However, the validity of the assumption  $\chi = S_l$  remains questionable.

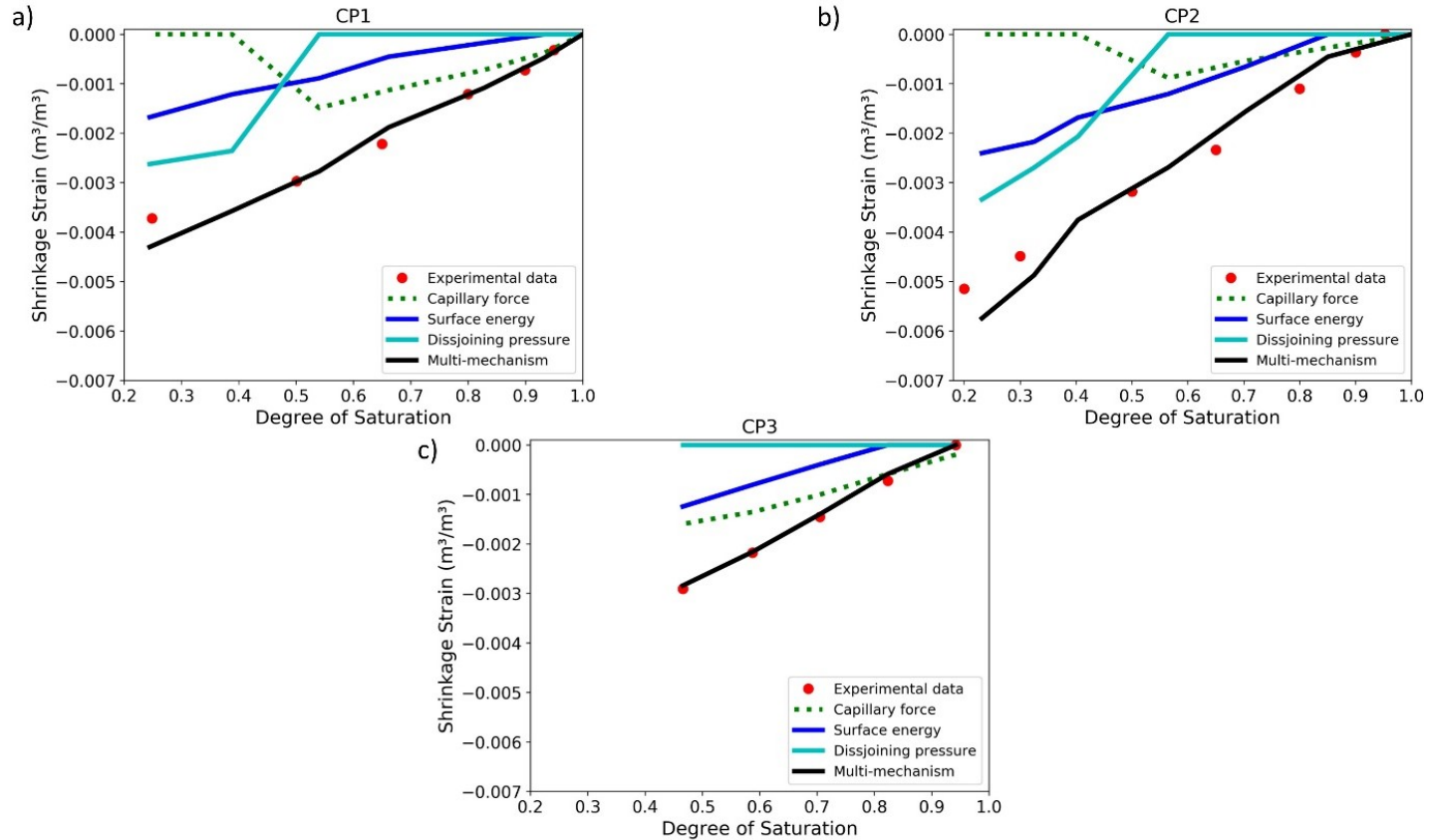


Figure 3-5. Contribution of each mechanism on predicted ultimate drying shrinkage vs. experimental data for non-virgin materials.

Figure 3-6 presents a comparison of results from the analytical framework that includes multi-mechanisms, Coussy et al. [75] that includes interface energy (Appendix A1) and Vlahinic et al. [24] that includes effective bulk modulus (Appendix A2) for CP1-CP3. The coefficient of determination of the predicted results varies from 0.91 to 0.99, 0.21 to 0.97 and 0.49 to 0.79 for the analytical framework, Coussy et al. [75] and Vlahinic et al. [24] respectively, thus offering an improved confidence in the capability of the analytical framework. Recall that

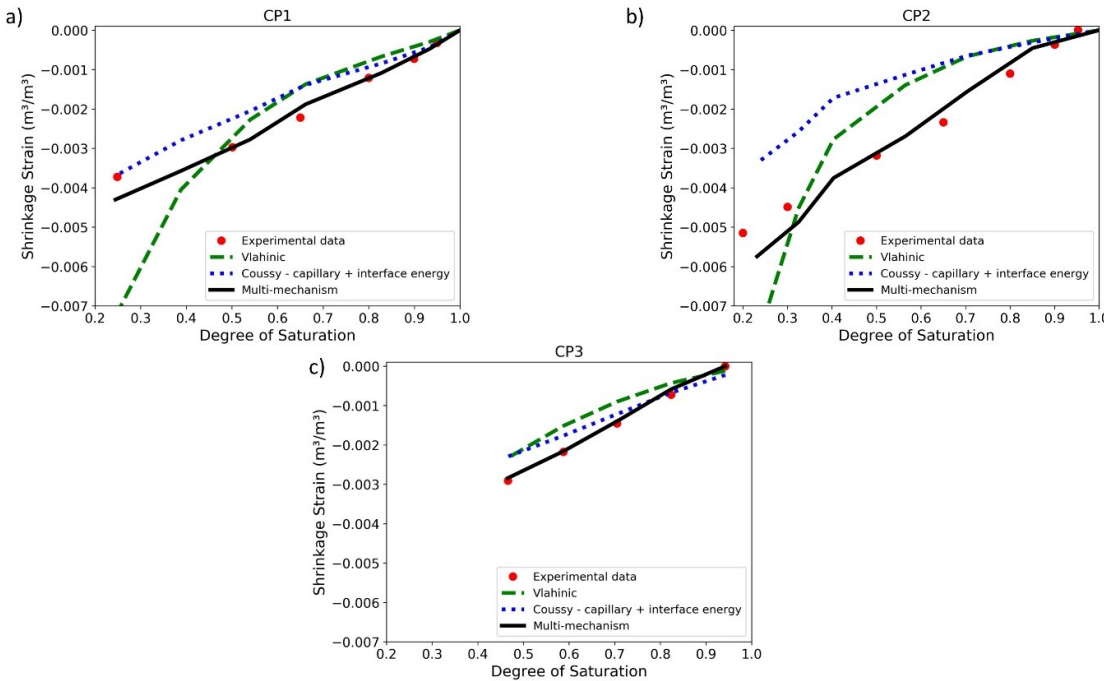


Figure 3-6. Predicted ultimate drying shrinkage from various models vs. experimental data for non-virgin materials.

Coussy’s model (Equation (3-16)) mainly relies on the WRC ( $S_l P_c$ ) to capture interfacial energies, and is also stated to be reliable up to  $RH=0.4-0.5$  according to Coussy et al. [75]. It is noted that as long as the capillary forces ( $S_l P_c$ ) dominate (Figure 3-5a and 3-5c), Coussy’s model shows reasonable correspondence with experimental data, which is the case with CP1 and CP3, although the deviation is much more with the latter. However, for CP2, which

has a relatively high  $W/C=0.8$ , it is shown that the calculated surface forces (Equation (3-10)) and disjoining pressure (Equation (3-12)) are dominant compared to the capillary forces (Equation (3-7)) (Figure 3-5b). Therefore, Coussy's model shows considerable deviation, which implies that their interfacial energy term does not fully compensate for the surface forces and disjoining pressure predicted by Equation (3-10) and Equation (3-12), respectively, specifically for high  $W/C$ .

### 3.3.4.2 VIRGIN MATERIAL - TOTAL STRAIN

Figure 3-7 (a)-(f) show a comparison of ultimate drying shrinkage strain of virgin materials (CP4 to CP9) as a function of degree of saturation. The predicted values generally show poor correspondence with experimental data except in the higher saturation range ( $S_l > 0.8$ ). The coefficient of determination for the multi-mechanism model ranges from 0.37 to 0.80 with a mean value of 0.64, for Coussy's model it ranges from 0.27 to 0.70 with a mean value of 0.57 and for Vlahinic's model it ranges from 0.2 to 0.6 with a mean value of 0.36. This is to be expected because during the first drying permanent deformation occurs (irreversible strain), which accounts for 29% to 40% of the total ultimate shrinkage strain (Table 3-2). Irreversible shrinkage may include processes such as densification of LD C-S-H [102, 104-106] and/or formation of microcracks [46, 106, 107] that are not captured by the multi-mechanism approach. In particular, it is clear that the strain due to capillary forces, surface free energy and disjoining pressure relies on two fundamental parameters, which are (i) desorption isotherm and (ii) bulk modulus. Firstly, a constant bulk modulus is considered for all the mechanisms and hence no microstructural changes are reflected. While it is possible to consider the variation of the bulk modulus as a

function of degree of saturation as in the effective bulk modulus concept (Appendix A1) of Vlahinic et al. [24], it still cannot compensate for the difference between the total strain and reversible strain, for example, as shown in Figure 3-7 (f) for CP9. Secondly, desorption isotherm is not significantly sensitive to small microstructural changes (Section 3.1 in [3]) and thus even though desorption isotherm may be determined on virgin samples, it will still not quantitatively reflect the microstructural changes.

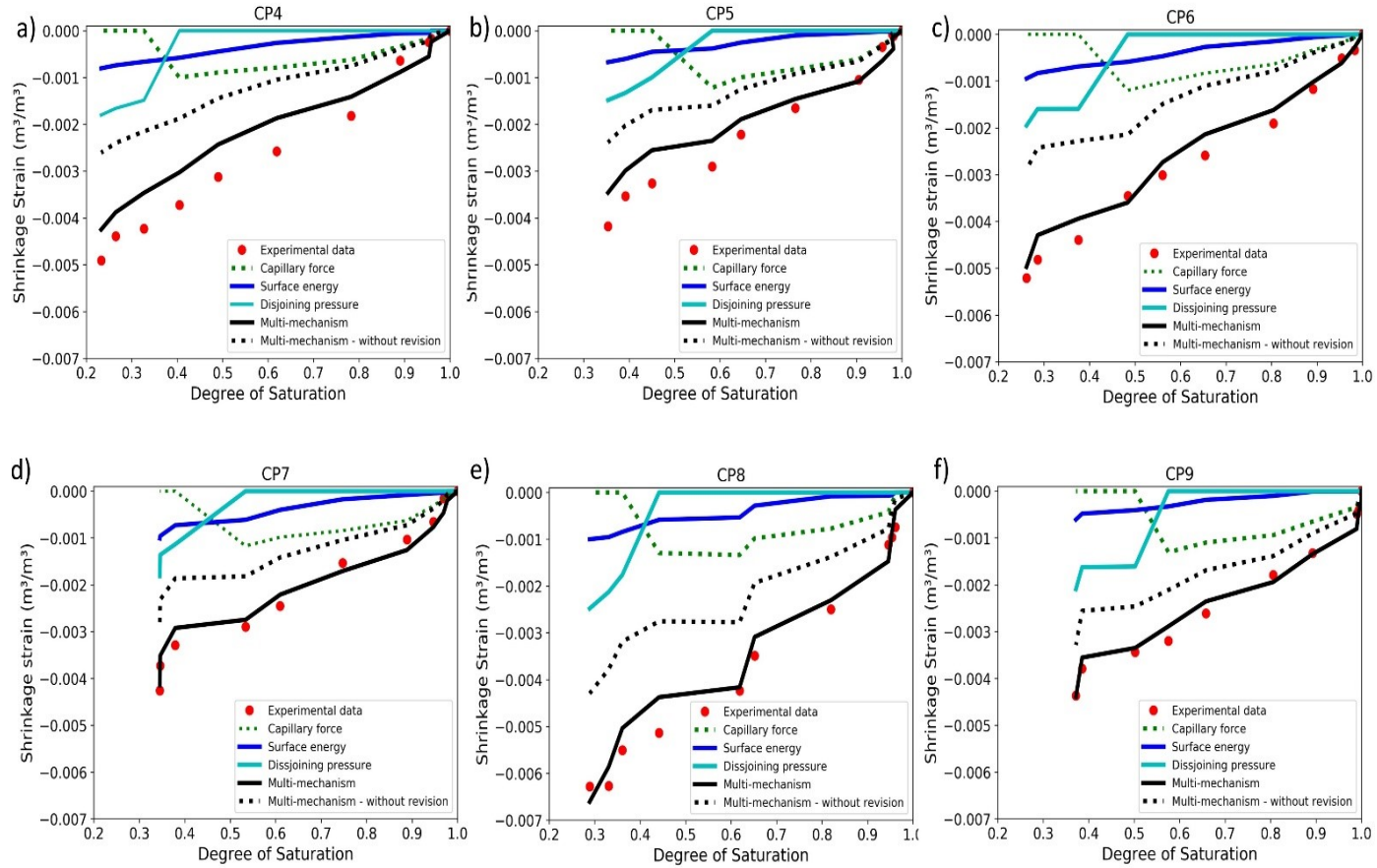


Figure 3-7. Contribution of each mechanism on predicted ultimate shrinkage vs experimental data for virgin materials. (multi-mechanism stands for proposed model plus experimental irreversible shrinkage)

To further explore the role of microstructure, irreversible shrinkage strains are extracted from the experimental data for CP4-CP9 by subtracting the total shrinkage strain obtained from the drying and wetting branch of the experimental isotherms at  $RH=1$ . Table 3-2 presents the maximum irreversible shrinkage strains for materials CP4-CP9 (column 11). A first observation is that the irreversible shrinkage strain is proportional to the extent of drying. For example, sample CP4 is subjected to more drying ( $S_f \approx 0.2$ ) compared to CP7 ( $S_f \approx 0.35$ ), and accordingly the irreversible shrinkage strain is slightly higher in the case of CP4. It is also seen that the higher the amount of LD C-S-H, the higher is the irreversibility (Figure 3-8(a) and Figure 3-8(b)). Jennings [47, 102] argued in his C-S-H conceptual model that drying densifies the low density C-S-H. Thus the experimental results confirm Jennings [47, 102] model. Furthermore, the only shrinking phase in the hardened cement matrix is C-S-H, therefore, it is evident that the volume fraction of C-S-H gel is proportional to the total shrinkage strain. Accordingly, Figure 3-8(c) shows the irreversible shrinkage strain as a function of product of volume fraction of LD C-S-H and total C-S-H. It is also observed that the surface area of the material has a noticeable influence on shrinkage [22, 36, 91]. Since surface energy is the only force active throughout the whole drying range (Figure 3-7), it can be a valid candidate for estimating irreversible component of shrinkage. Other factors affecting the irreversibility are the solid bulk modulus and porous bulk modulus, which are functions of volume fraction of various hydration products but mostly C-S-H and porosity. These factors provide a basis to propose a phenomenological approach to account for the volumetric irreversible shrinkage strain,  $\varepsilon_{v,irr}$ . One proposal could take the form:

$$\varepsilon_{v,irr} = (\varepsilon_{vs} V_{C-S-H} V_{LD\ C-S-H}) / \eta_t \quad (3-14)$$

Where  $\varepsilon_{vs}$  is shrinkage due to surface free energy,  $V_{C-S-H}$  is volume fraction of C-S-H,  $V_{LD\ C-S-H}$  is volume fraction of LD C-S-H. which is observed to be at

least valid for the six datasets presented in this paper (Figure 3-8(d)). Adding  $\varepsilon_{v,irr}$  with  $\varepsilon_{v,r}$  will yield the total drying shrinkage strain as shown in Figure 3-7 (*legend: multi-mechanism*). It is seen that the multi-mechanism model results now correspond well with the experimental data for virgin materials, especially for CP6-CP9 with coefficient of determination of 0.99 for all the four. However, the level of accuracy is less satisfactory for CP4 and CP5 whose coefficient of determination are 0.86 and 0.91, respectively indicating that the multi-mechanism approach may still be missing some important mechanisms or it is possible that there are some experimental uncertainties. It is important to note that Eq.(3-14) is merely a phenomenological model, which happens to work on these materials and no further conclusion can be made given such small number of data points.

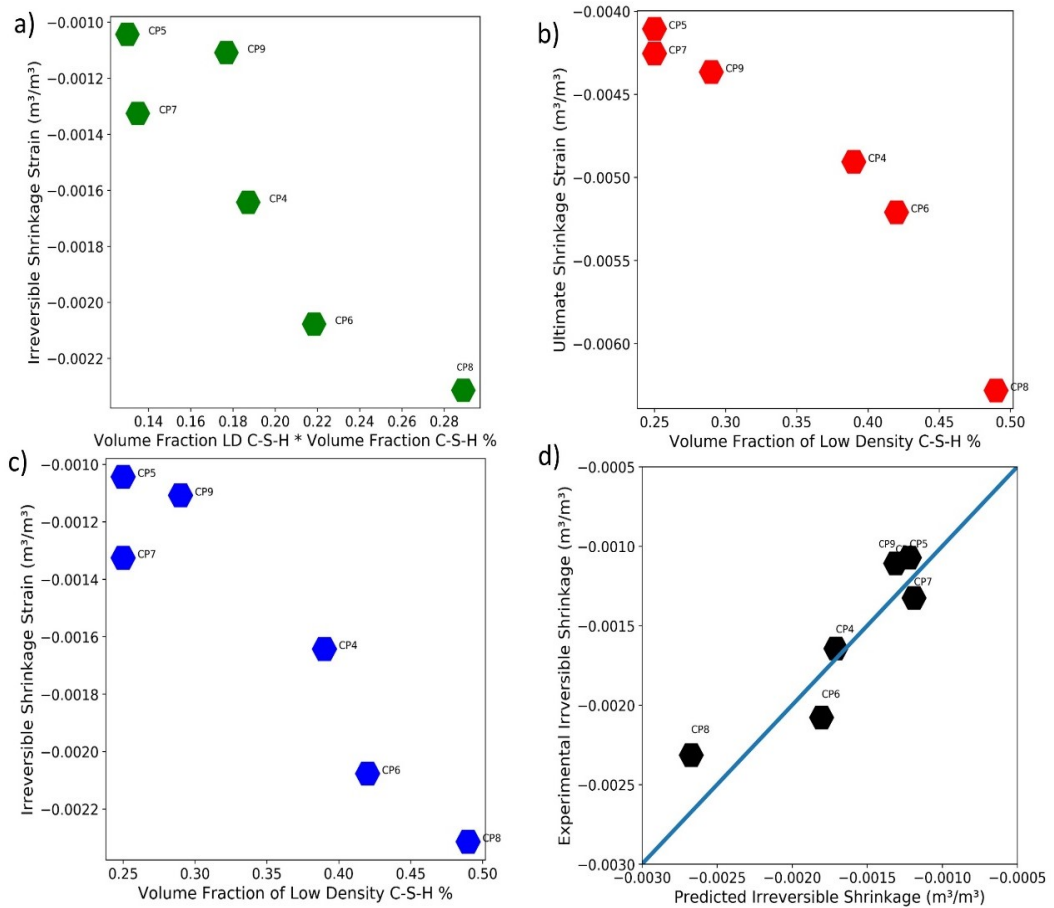


Figure 3-8. Irreversible shrinkage and its correlation with microstructural information.

### 3.4 Conclusions

A new analytical framework to estimate drying shrinkage strain for OPC-based materials is presented. As a starting point, the framework principally requires cement composition, microstructural information and mechanical properties of hydrated phases. There are only two calibration parameters: (i) a geometric parameter used in the pore network model, and (ii) a constant in the disjoining

pressure relationship, which is set to unity because of a lack of knowledge (hence strictly no calibration). Importantly, there is no need to calibrate these parameters for every experiment. The following specific conclusions are reached:

- i. Predicted desorption isotherms are in good correspondence with wide ranging experimental data from literature. In this study, six isotherms have been validated, which is in addition to the eleven isotherms already validated by the authors in their previous work Babaei et al. [3, 108], thus offering further confidence in the pore network model that forms the core module of the multiscale WSI framework.
- ii. With some exceptions, the predicted bulk modulus of hardened cement paste is in good agreement w.r.t. the experimental data from literature. The deviations are attributed to the uncertainty in the results of the hydration model.
- iii. The chosen drying shrinkage formulation has offered reasonably good results and offers insights into the active mechanisms during drying. In particular, the general trend is that the contribution of surface free energy to the shrinkage strain is relatively less than the disjoining and capillary forces, but is still quantitatively important for accuracy. Moreover, this trend depends on the W/C ratio. The formulation performs generally well compared to the equivalent pore pressure and effective bulk modulus concepts.
- iv. It is not surprising that the drying shrinkage formulation does not offer satisfactory results w.r.t. experiments on virgin materials, which are subject to first drying cycle. Examining the experimental results vis-à-vis hydration kinetics model suggest that the higher the amount of LD C-S-H, the higher is the irreversibility. A phenomenological model is proposed that quantitatively captures the irreversible shrinkage strain.

### 3.5 Appendix A

#### 3.5.1 Equivalent pore pressure concept – Coussy

Coussy et al. [75] used equivalent pore pressure concept to compute drying shrinkage strain. In their model, interface energy,  $U$ , was defined as the sum of energy of all the interfaces including, liquid-gas, solid-liquid and solid-gas:

$$U = \int_{S_l}^1 P_c(s) ds \quad (3-15)$$

Equivalent pore pressure,  $\pi$ , is defined via:

$$\pi = P^* - U \quad (3-16)$$

where  $P^*$  is the average pore pressure ( $S_l P_c$ ). The drying shrinkage strain is then calculated via:

$$\varepsilon = \frac{\alpha_B \pi}{K_b} \quad (3-17)$$

#### 3.5.2 Effective bulk modulus concept – Vlahinic et al.

Vlahinic et al. [24, 109] proposed a constitutive model, which considers loss of stiffness of the material as the main parameter that dictates the volumetric deformation, which is attributed to microstructural evolution during drying. Their approach deviates from Bishop [82], which considers average pore pressure as the main parameter that dictates the volumetric deformation. The loss of stiffness is thus expressed in the form of reduction of  $K_s$  with decrease in

degree of saturation,  $\bar{K}(S_l)$ , which is an experimentally aided estimate as defined in Eq. (3-19).

$$\varepsilon_{vc} = P_c \left( \frac{1}{K_b} - \frac{1}{\bar{K}(S_l)} \right) \quad (3-18)$$

$$\bar{K}(S_l) \approx K_s - \frac{K_s - K_b}{\varphi_0} \varphi(S_l) \quad (3-19)$$

$$\varphi(S_l) = \frac{(1 - S_l)\varphi_0}{1 - S_l\varphi_0} \quad (3-20)$$

where  $\varphi$  is the porosity of the effective solid,  $\varphi_0$  is the initial porosity and  $S_l$  is the degree of water saturation.

## 4 Permeability of hardened cement paste using the pore network model

---

### 4.1 Introduction

# Chapter 4

Cementitious materials are ubiquitously used in urbanization. They can be seen everywhere in civil and infrastructure constructions from small components to whole buildings. Besides their classical use in construction, these materials are also envisioned for use both as encapsulation of radioactive waste and as engineered barriers for disposal of radioactive waste, which is one of the direct relevance of this thesis. One of the major governing parameters for performance and safety assessment of cementitious materials is their permeability because this has a direct link with the transport mechanisms of aggressive substances responsible for degradation of the cementitious matrix. In addition, it is a measure of how the cementitious material can withstand drying due to external environmental loading, which can have a decisive impact on shrinkage induced cracks. Permeability itself as a general term is an indication of the ability for fluids (gas or liquid) to flow through porous material. The intrinsic water permeability (also called specific permeability or absolute permeability) is the measured permeability for a fully saturated state and the unsaturated water permeability or relative permeability is the measured permeability at lower degrees of saturation. However, measuring permeability is not straight forward and there are two main approaches to measure it in laboratory, direct and indirect measurements. While the former is done usually by means of applying a certain pressure gradient or flow rate on a cylindrical sample and quantifying the permeability using Darcy's law, the latter approach involves either the application of a transient pressure pulse technique or the application of

poromechanical techniques or inverse analysis of moisture loss experiments. A review of these experimental methods can be found in [110-113].

However, the experimental measurement of permeability is time consuming and results can vary depending on the experimental method. Furthermore, measurement of unsaturated permeability is even more challenging given the fact that having control over all the contributing parameters is hard to achieve. Therefore, the unsaturated permeability is usually measured using inverse analysis of weight loss experiments [111, 114].

Considering the importance of permeability and experimental challenges to overcome, there have been various attempts to model permeability starting from classical models such as Kozeny's work [115] that relates the permeability to the porosity and later modified by Carman known as Kozeny–Carman equation [116]. The Katz-Thompson model [117] that was initially developed to predict the permeability of sedimentary rocks and relates the permeability to microstructure of the cementitious material using an analytical approach. And more recently with advancements in numerical approaches there has been several studies to estimate transport properties of cementitious materials complex numerical models that have been proposed. To mention a few on numerical models, G. Ye et.al [118] presented a network model by means of extracting the pore space from simulated cement microstructure and embedding them into a network. They estimated the fluid flow by applying Hagen–Poiseuille law on the conduits and calculated the intrinsic permeability using Darcy's law. Their model only accounted for capillary porosity, which implies that there will be overestimation of the permeability value. Zalzale et.al [119] applied a 3D lattice Boltzmann technique to model permeability at different degrees of saturation. In addition to permeable micron-sized capillary pores they managed to also include weakly-permeable nano-porous calcium silicate hydrate (C-S-H) pores in their model. The critical parameters, C-S-H density and

capillary porosity, were taken from  $^1H$  (*hydrogen*) nuclear magnetic resonance relaxation analysis. Their model however accounted only for variation of capillary pore size distribution and applied pore blocking of these pores. Their pore blocking algorithm was based on the principle that the biggest pores get blocked first regardless of its location. Kai Li et.al [120, 121] employed discrete element method (DEM) to generate and characterize microstructures and estimated the permeability using conventional moisture transfer equation. However, their microstructure only included the capillary pores and the gel pores were neglected. Their computational approach for unsaturated permeability is similar to Zalzale et.al [119].

As mentioned all these previously proposed models either require some empirical or experimental parameters involved in the modelling or they do not take all the pore size range of the material into account. Therefore, this chapter presents a multiscale and largely predictive approach, which can drive the information from microstructure and integrate them into a representative numerical framework to model both intrinsic and unsaturated permeability. This numerical framework consists of different modelling tools discussed in Chapter 2 of this thesis to arrive at a statistically representative pore network, which is used as a basis to carry out moisture transport calculations. The proposed pore network modelling framework is validated against an extensive set of experimental data that includes a very wide range of materials[67, 110, 112, 114, 122-126].

## 4.2 Multiscale pore network

The pore network is constructed using hierarchical homogenization of pore space (Figure 4-1) similar to that elaborated in Chapter 2 and in [3] but since permeability is more sensitive to spatial distribution and arrangement of pore classes the microstructure is reflected slightly different into a pore network framework.

In Chapter 2, the network was constructed to determine the saturation degree at different relative humidity and thus the volume fraction of each pore class would be directly transferred to the network meaning that if the pore space consists of 0.5 gel pores and 0.5 capillary pores in terms of volume fraction then the same ratio in terms of volume fraction would have to exist in the network as well. Therefore, the resulting network would be much bigger (in terms of number of pores) but in this chapter in order to transfer the data from microstructure to the pore network the volume fraction of each pore class is converted to their population number, for instance a microstructure with capillary porosity of 0.25 and 0.6 C-S-H gel in microstructure level, is represented by 1.47 million of capillary pores and 1 million of gel pores assuming the gel porosity is 0.28. Network generation is carried out in four steps:

- (i) An initial cubic network with size of 100  $\mu\text{m}$  and 1 million pores is created for homogenized network at C-S-H level.
- (ii) Largest fraction at level (i) (C-S-H level) is chosen as the master phase and added to the network. Their population is calculated based on the LD/HD ratio at level (i) and total number amount to 1 million pores. i.e.,  $n_{master\ C-S-H} = \text{Dominant } C-S-H \text{ phase} * 1e6$

- (iii) Pores of secondary phase at level (i) are added to the master network to form a homogenized network at level (i) holding HD and LD C-S-H gel pores.
- (iv) The capillary pores are randomly distributed in the homogenized gel network to form a network, which includes all the three pore classes. The number of capillary pores is equal to  $n_{capillary} = \left( \frac{capillary\ porosity}{gel\ porosity} \right) * 1e6$
- (v) Throats are added to connect pores and their size is calibrated as described in Babaei et al. [3]

Once the pores are embedded, there are multiple possible ways to connect them, the coordination number in this research is assumed to be six as it assures enough connectivity within different classes of pores and also does not over facilitate the flow in the network as cementitious materials are known to be weakly permeable[3]. Regarding the size and length of this connecting throats the same values are applied as mentioned in Babaei et al. [3]. It is also worth recalling that there is a missing gap between the two scales as the biggest gel pore is 12 nm and smallest capillary pore possible with microstructural modelling is 1 um, this gap however is filled using a numerical approximation as explained in Babaei et al. [3].

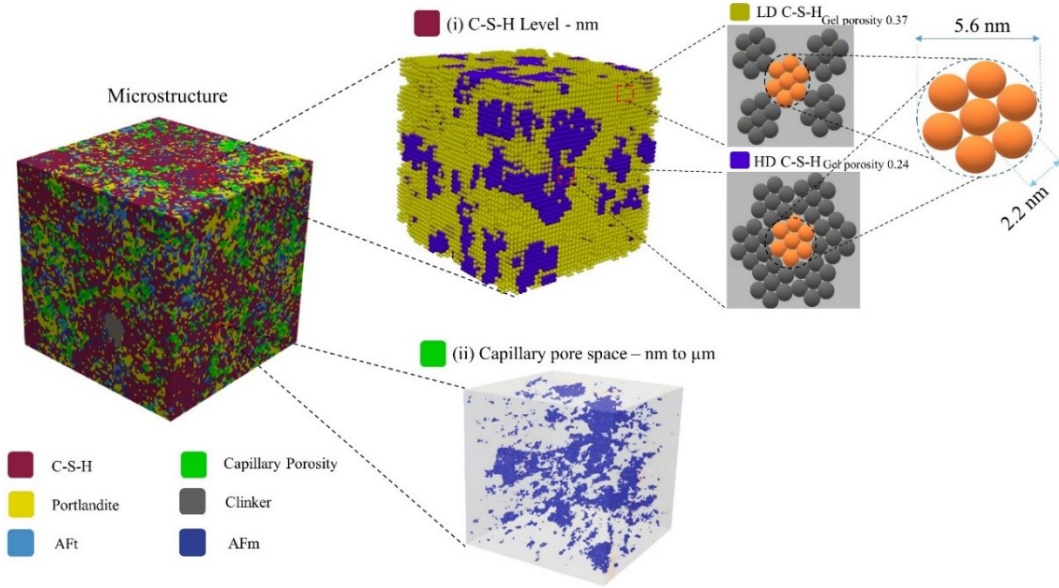


Figure 4-1. The microstructure and the pore space within the proposed multiscale modeling

### 4.3 Permeability calculations

#### 4.3.1 General principle

The general principle of computing permeability from the constructed pore network is to apply a water pressure gradient across any two opposite faces of the network and computing average water flux. Darcy's law can then be invoked to back calculate the permeability of the network as follows:

$$Q = K_l \frac{A}{\mu L} \Delta P \quad (4-1)$$

where  $Q$  is the flow rate ( $\text{m}^3/\text{s}$ ),  $A$  is the network cross section area ( $\text{m}^2$ ),  $L$  is length of the network (m),  $\mu$  is the dynamic viscosity (Pa.s),  $\Delta P$  is pressure

difference across the two opposing sides ( $P_a$ ), and  $K_l$  is permeability of the network ( $m^2$ ).

This formulation is applicable for water filled conduits only, i.e., for saturated porous medium. In the following sections, algorithms to compute intrinsic and unsaturated permeability are detailed.

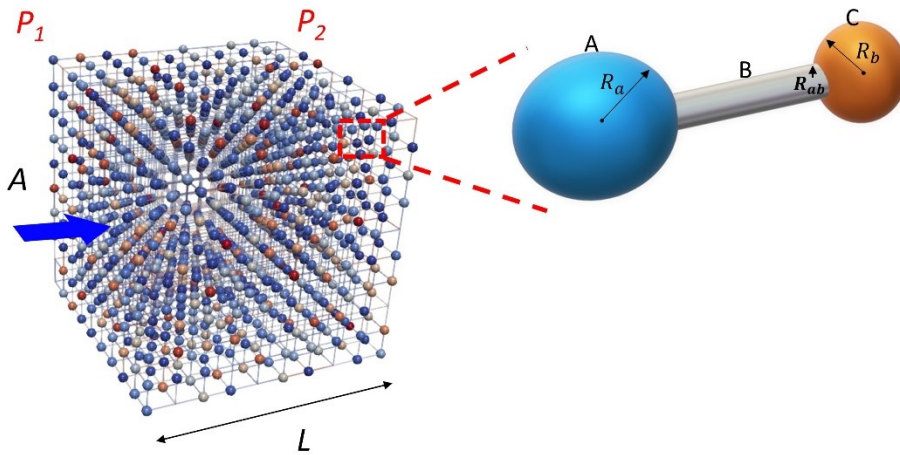


Figure 4-2. Measurement of intrinsic permeability by applying pressure gradient

### 4.3.2 Intrinsic permeability

The intrinsic permeability is independent of measurement factors such as, measurement method, sample size, pressure gradient, etc., and depends solely on pore space structure of the cementitious material.

The method described below essentially provides an estimation of the intrinsic permeability, meaning that all the pores are contributing to the flow rate and are

fully saturated. In order to compute the flow through the network an exact solution of Navier-Stokes equation, i.e. the Hagen-Poiseuille's law is applied for each conduit formed by two neighbouring pores and their connecting throat. The flow rate,  $q_c$ , and hydraulic resistance,  $R_c$ , for each conduit is computed via [40, 127]:

$$q_c = R_c \Delta P \quad (4-2)$$

$$R_c = \left[ \frac{1}{R_{p1}} + \frac{1}{R_t} + \frac{1}{R_{p2}} \right]^{-1} \quad (4-3)$$

where  $p1$ ,  $t$  and  $p2$  refers to pore 1, throat and pore 2, respectively that forms one conduit system. Throats have a constant diameter and Hagen–Poiseuille's law is directly applicable for computing their hydraulic resistance, but since the pores in the generated network are assumed to be spheres, they have varying cross section, depending on the connecting throat diameter in the entire network. Therefore, to compute the hydraulic resistance,  $R$ , of each element (throat and pores) the approach proposed by Akbari et.al. [127] for slightly varying micro-channels is used as follows:

$$R = q / \Delta P = [16\pi^2 \mu \int_{x_1}^{x_2} \frac{I_p^*}{A^2} dx]^{-1} \quad (4-4)$$

where  $I_p^* = I_p / A^2$  with  $I_p = \int_A (y^2 + z^2) dA$  is called the specific polar moment of cross-sectional inertia.  $\mu$  is the dynamic viscosity,  $A_1$  and  $A_2$  are the cross sectional area at  $x_1$  and  $x_2$  as in (Figure 4-3).

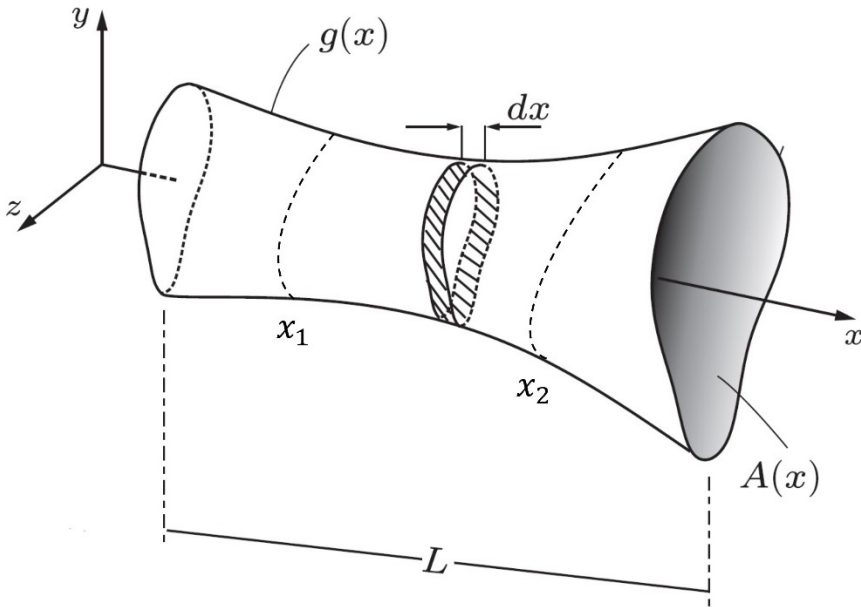


Figure 4-3. Geometry of a slightly varying micro-channel adapted from [127]

Once, the hydraulic resistances of all the conduits in the pore network are computed, an arbitrary positive pressure gradient is applied on any two opposite faces of the network (say in the  $x$  direction), with zero flux imposed on the remaining faces. The following mass conservation is solved for each pore as follows:

$$\sum_{j=1}^n R_{i,j} \cdot (x_i - x_j) = 0 \quad (4-5)$$

where  $j$  is the index of neighbouring pores, which is equal to the coordination number for pore  $i$  (here = 6),  $R_{i,j}$  is hydraulic resistance between  $i$  and  $j$ , and  $x$  is the unknown quantity being solved for, which is the pressure field here. For instance for pore  $i=1$  and its neighboring pores of  $j=(2,3,4,5,6,7)$ , it results in:

$$-(R_{1,2} + R_{1,3} + R_{1,4} + R_{1,5} + R_{1,6} + R_{1,7}) \cdot x_1 + R_{1,2} \cdot x_2 + R_{1,3} \cdot x_3 + R_{1,4} \cdot x_4 + R_{1,5} \cdot x_5 + R_{1,6} \cdot x_6 + R_{1,7} \cdot x_7 = 0 \quad (4-6)$$

For the entire pore network, the mass conservation equations can be assembled to calculate the unknown pressure field,  $\mathbf{x}$ :

$$\mathbf{x} = \mathbf{A}^{-1}\mathbf{b} \quad (4-7)$$

where  $\mathbf{A}$  is a matrix composed of set of linear equations in accordance with the abovementioned equation for each pore in the network. The vector  $\mathbf{b}$  contains components of the boundary condition, which is a constant arbitrary pressure applied on two sides of the network i.e., Dirichlet boundary condition. The flow field is computed based on the calculated pressure field as explained above. Finally, to determine the network's effective water permeability, the total flow rate is calculated at the boundary pores lying in a plane perpendicular to the flow direction. The water permeability is then obtained via Eq.(4-1) as explained earlier.

The calculations are repeated for the remaining pairs of opposite faces or sides to yield permeability in all mutually perpendicular directions. Finally, the average of the three permeability values are computed.

### 4.3.3 Unsaturated permeability

The calculated intrinsic permeability is not valid for partially saturated state in which some of the pores are empty and thus do not contribute to the water flow. In order to simulate relative humidity, two independent algorithms are implemented and executed in parallel on the same network to resemble realistic

partially saturated flow mechanism. The calculation methodology is the same as intrinsic permeability for network generation and calculation of hydraulic resistance. However, a preceding step involves running an invasion algorithm, which simulates drying process in response to the external boundary condition, which in this instance is the capillary pressure,  $P_c$ . Invasion algorithm essentially invades air phase into the network from all sides following the approach described in Chapter 2 or in other words conduits get desaturated in accordance with the applied  $P_c$  on the boundaries. The relative permeability is then computed via a number of sequential iterations of invasion algorithm and permeability simulation as follows (Figure 4-4):

- (i) The intrinsic permeability is calculated at  $P_c=0$  Pa (or  $RH=1$ ), i.e. for the fully saturated network. For this an arbitrary positive pressure gradient is applied across any two opposite sides.
- (ii) Invasion algorithm is applied on the network by incrementing  $P_c$  to desaturate the pores. The pores and throats, which are invaded (or desaturated) are assigned to be blocked from water flow.
- (iii) The permeability of the partially blocked network will be determined in accordance to step (i).
- (iv) The above sequence is continued for different increments of  $P_c$  to cover the entire range of degree of saturation (or  $RH$ ). It is obvious that when the degree of saturation of the network is close to zero, most of the network conduits are blocked.

In the example shown in Figure 4-4, four snapshots of desaturation of fully saturated pore network is shown. The desaturated pores seen in yellow colour are the ones that are blocked for water flow.

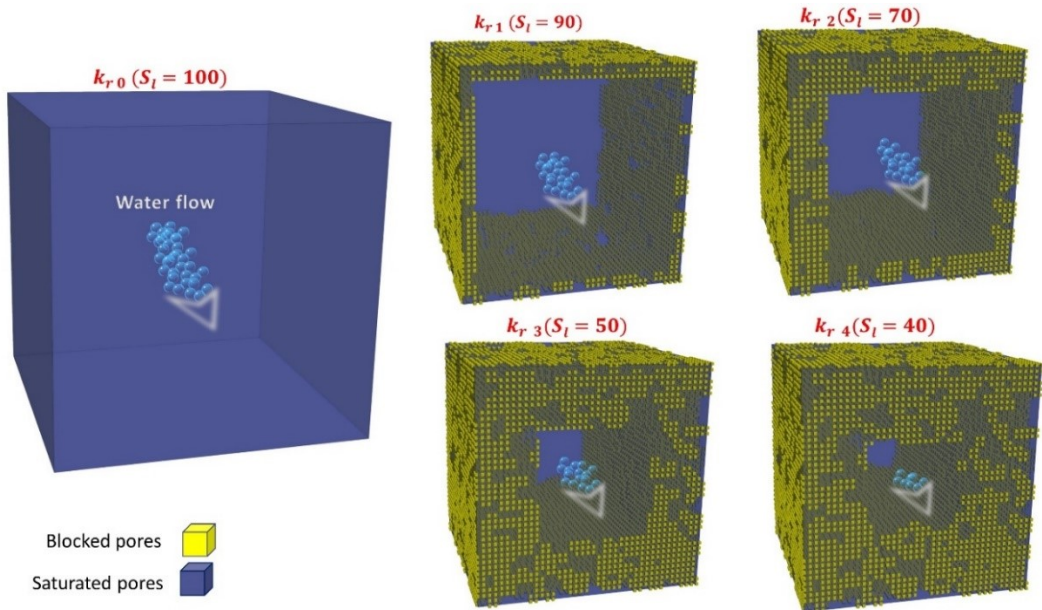


Figure 4-4. Sequential invasion of the network and calculating the relative permeability for each sequence (here 4 different degrees of saturations).

## 4.4 Results and validation

The method proposed in this paper is validated against an extensive number of experiments available in literature. The validation is conducted in two parts: (i) intrinsic and (ii) unsaturated permeability.

Table 4-1 shows the experimental details of each dataset. Note that the measured value for intrinsic permeability may differ depending on the experimental approach [111, 114, 128] and it can vary up to an order of magnitude and even higher [111, 114]. That is why an estimation within a range of order of magnitude is still acceptable. In addition to measurement uncertainties, there can be a factor of back calculation error effect involved in reported values, e.g. when the permeability is back calculated using Van Genuchten [129] retention curve but the fitting is not perfect.



Table 4-1. Experimental data from literature [67, 110-112, 114, 122-126]. \*Hardened cement paste (HCP)

Material	Author	Measurement method	Material Type	W/C	Age (days)	Curing	Intrinsic permeability (m <sup>2</sup> )
CP1	Baroghel-Bouny (1999)	Inverse analysis from mass loss	HCP	0.34	365	Sealed then vacuum rewetted	10 <sup>-21</sup>
CP2	Ai et al (2001)	Thermo-permeametry	HCP	0.4	548	Sealed and moist cured for 24 h then cured underwater	8.65 × 10 <sup>-22</sup>
CP3	Ye (2005)	Pressure cell	HCP	0.4	28	Sealed then vacuum rewetted	9 × 10 <sup>-22</sup>
CP4				0.5			1.33 × 10 <sup>-19</sup>
CP5				0.6			1.82 × 10 <sup>-18</sup>
CP6	Grasley (2007)	Dynamic pressurization (DP)	HCP	0.5	80	Limewater	3 × 10 <sup>-21</sup>
CP7				0.6			32
CP8	Phung (2013)	Constant flow	HCP	0.4	28	Limewater	8 × 10 <sup>-21</sup>
CP9				0.5			3 × 10 <sup>-20</sup>

Chapter 4 - Permeability of hardened cement paste using the pore network model

<b>CP10</b>				0.6			$7 \times 10^{-20}$
<b>CP11</b>	Kumar (2014)	MIP	HCP	0.45	28	sealed	$4 \times 10^{-21}$
<b>CP12</b>				0.5			$1 \times 10^{-20}$
<b>CP13</b>				0.64			$2 \times 10^{-19}$
<b>CP14</b>	Zamani (2014)	Inverse analysis	HCP	0.4	28	Under water	$4 \times 10^{-21}$
<b>CP15</b>	Egan (2017)	Inverse analysis	HCP	0.45	56	Limewater	$3 \times 10^{-21}$
<b>CP16</b>				0.55			$6 \times 10^{-21}$
<b>CP17</b>				0.65			$2 \times 10^{-20}$
<b>CP18</b>	Zhang (2018)	Beam Bending - Sorptivity	HCP	0.5	365	Limewater	Avg.= $1.2 \times 10^{-19}$

#### 4.4.1 Intrinsic permeability

The estimation of permeability involves carrying out microstructural modelling (hydration calculations) using the cement composition data reported by various researchers in Table 4-1(OPC here). The results from the microstructural model is presented in Table 4-2, based on which pore network is constructed for each material composition, which is subsequently taken forward to estimate permeability. Note that to simulate permeability, 18 pore networks have been constructed corresponding to the 18 data sets available in Table 4-2. A comparison of results from the proposed method against experimental observations are presented in Figure 4-5.

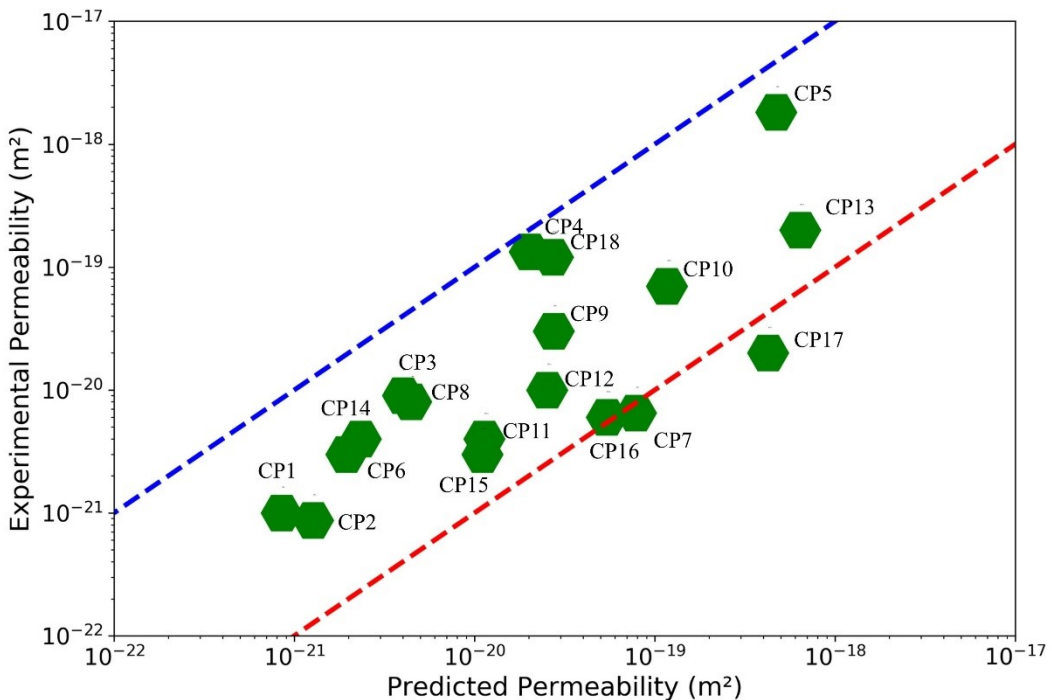


Figure 4-5. Estimated values using pore network modelling vs. experimental observations (\*dash lines order of magnitude lines).

Table 4-2. The microstructure information of the studied materials.

Material	C3S (wt%)	C2S (wt% )	C3A (wt% )	C4AF (wt%)	W/C (wt% )	C-S-H (vol%)	LD C-S-H (vol%)	HD C-S-H (vol%)	Capillary Porosity (vol%)	Total Porosity (vol%)	Estimated Permeability (m <sup>2</sup> ) – $k_0$
CP1	57.28	23.98	3.03	7.59	0.34	0.57	0.18	0.32	0.12	0.24	8.51E-22
CP2	67.1	17.5	7.7	7.6	0.4	0.53	0.22	0.25	0.13	0.25	1.27E-21
CP3	63	13	8	9	0.4	0.52	0.22	0.24	0.14	0.25	4.00E-21
CP4					0.5	0.50	0.33	0.13	0.19	0.29	2.21E-20
CP5					0.6	0.46	0.37	0.09	0.23	0.33	4.72E-19
CP6	48.3	21.5	7.6	9.1	0.5	0.49	0.33	0.13	0.19	0.30	1.94E-21
CP7					0.6	0.46	0.36	0.10	0.22	0.32	7.86E-20
CP8	62.5	18	9	10	0.4	0.50	0.21	0.23	0.14	0.25	4.45E-21
CP9					0.5	0.48	0.32	0.12	0.19	0.30	2.75E-20
CP10					0.6	0.45	0.40	0.05	0.24	0.34	1.17E-19
CP11	59.2	16.7	9	10.3	0.45	0.53	0.29	0.20	0.18	0.29	1.13E-20
CP12					0.5	0.51	0.35	0.14	0.20	0.32	2.53E-20
CP13					0.64	0.46	0.40	0.06	0.27	0.37	6.39E-19

Chapter 4 - Permeability of hardened cement paste using the pore network model

<b>CP14</b>	66.9	20	3.5	4.4	0.4	0.58	0.25	0.27	0.14	0.27	2.33E-21
<b>CP15</b>	56.5	18	6.3	11.4	0.45	0.50	0.28	0.18	0.17	0.28	1.11E-20
<b>CP16</b>					0.55	0.47	0.38	0.07	0.22	0.32	5.40E-20
<b>CP17</b>					0.65	0.44	0.38	0.06	0.26	0.36	4.25E-19
<b>CP18</b>	53.6	17.5	7.5	8.8	0.5	0.49	0.33	0.13	0.19	0.29	2.72E-20

The results show a very good correspondence with the experimental observations. In fact, the results fall well within the same order of magnitude for 17 out of 18 studied cases. This confirms that the proposed model can successfully and systematically transfer information from microstructure into a pore network, which is representative of permeability of HCP.

The predicted value for CP17 is the only case where the model fails to estimate within the same order of magnitude as the experimentally observed value. However, in this case, the permeability is indirectly measured; firstly fitting a Van Genuchten [129] curve on experimental retention curve and then back calculating the mass loss using the fitted Van Genuchten curve. This method however is sensitive to fitting parameters of the retention curve and thus can be affected by the accuracy of fitting. Moreover, different types of measurements can lead to different results and this is mainly due to experimental uncertainties. For instance, CP13 and CP17 have a relatively similar composition but the measured permeability for CP13 is exactly one order of magnitude less than that of CP17, while ratio of their permeability estimated by the proposed model is 3. The same argument holds for CP16, whose permeability value lies just at the border of the order of magnitude line.

While for CP7, the lack of accuracy can be at least partly attributed to the measurement method. The experimentally measured value for CP7, which is an OPC with W/C of 0.6 is measured to be  $6.5 \times 10^{-21} \text{ m}^2$  that is at least an order of magnitude lower than similar compositions with the same W/C ratio (CP5, CP10) and using different experimental methods. As mentioned the measurement method can also affect the measured value and this seems to be the case here. Furthermore, the estimated values using pore network seems to be mostly close to the values measured by constant flow and indirect measurements (inverse analysis).

From the microstructural modelling results presented in Table 4-2 it is seen that the permeability can be correlated with the ratio of HD and LD C-S-H at C-S-H level and the capillary porosity at microstructure level. A parametric analysis (Figure 4-6) shows that for the study cases the permeability is directly proportional to the capillary porosity (Figure 4-6 (a)) and inversely proportional to the HD C-S-H gel porosity (Figure 4-6 (b)), which is the lowest permeable phase of C-S-H. In terms of comparative parameters, consistent trends for  $V_{LD\ C-S-H} / V_{HD\ C-S-H}$  (Figure 4-6 (c)) and  $V_{capillary} / V_{total\ porosity}$  ratios (Figure 4-6 (d)) are also observed ( $V_x$  denotes volume fraction of phase x). One parameter that is found to be correlating the best with the estimated intrinsic permeability is the factor  $\alpha$  defined as  $\alpha = W/C * V_{C-S-H} * V_{Capillary\ porosity}$ . Hence, the higher the  $\alpha$ , the higher the permeability (Figure 4-6 (e)). This trend is consistent for all the data points with a small deviation from linear trend noticeable. The experimental observations also confirm the same trend. Such parameters come remarkably handy when a qualitative comparison needs to be done without doing complicated calculation.

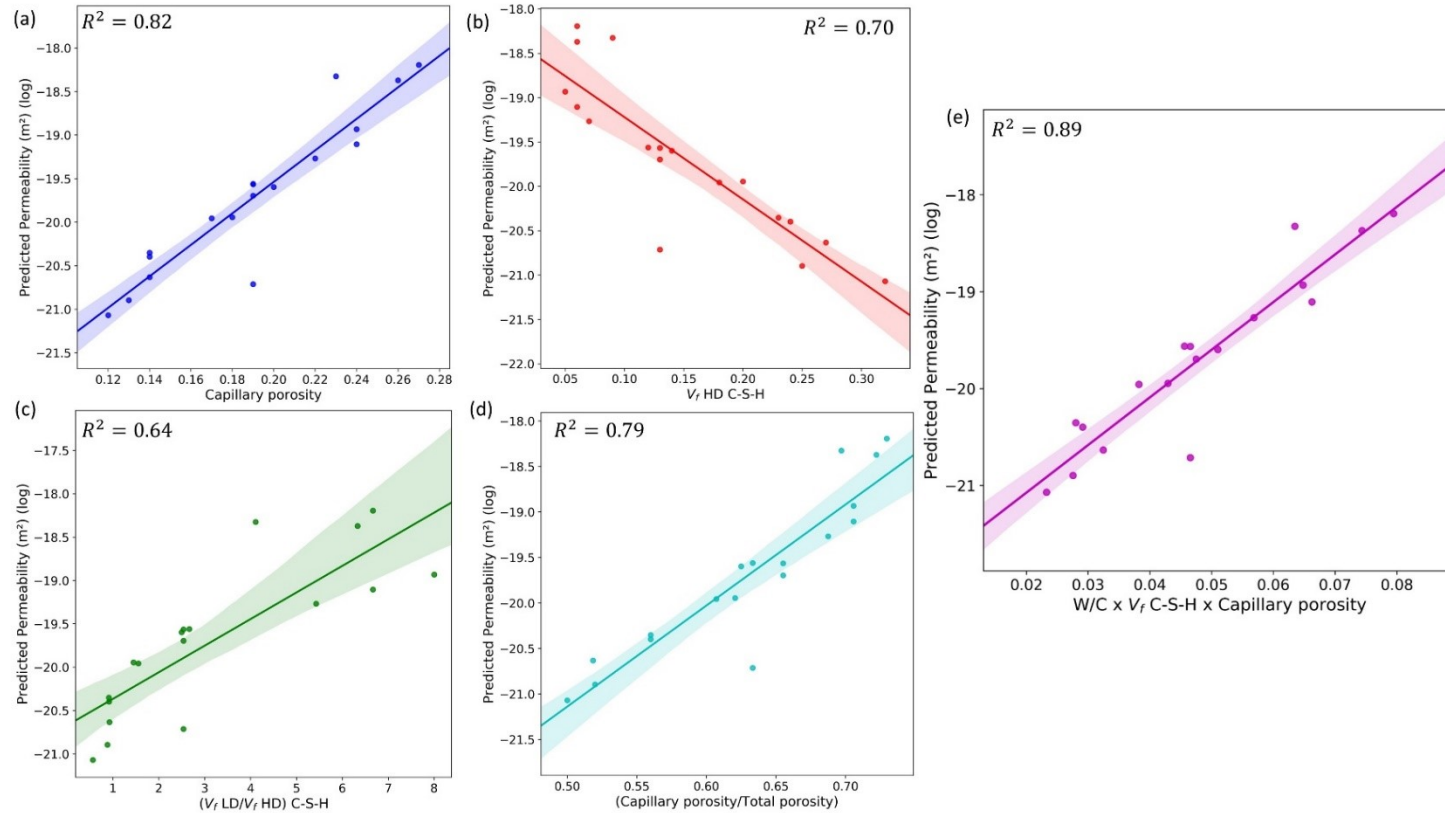


Figure 4-6. Parametric analysis of intrinsic permeability for the studied materials.

#### 4.4.2 Unsaturated permeability

Unsaturated permeability is simulated using the method explained in section 4.2.7. The unsaturated permeability is usually measured using inverse analysis of mass loss curve as direct measurement is not feasible. For the material CP1 and CP18 the unsaturated permeability values are available based on the inverse analysis, which will be used for comparisons. Additionally, comparisons will be made against the unsaturated permeability obtained from a calibrated water retention curve using the well-known Van Genuchten [129] model.

The Van Genuchten model for retention curve and unsaturated permeability is defined as follows:

$$S_l = \left[ \left( \left( \frac{p_c}{a_{mu}} \right)^{\frac{b_{mu}}{b_{mu}-1}} + 1 \right)^{-\frac{1}{b_{mu}}} \right] \quad (4-8)$$

where  $a_{mu}$  and  $b_{mu}$  are fitting parameters, which require fitting for each set of water sorption experiments available for the materials CP1 and CP18.

The unsaturated permeability is defined as:

$$k_l = k_0 k_{rl}(S_l) \quad (4-9)$$

where  $k_0$  is the intrinsic permeability for CP1 and CP18 (Table 4-1) and  $k_{rl}(S_l)$  is the relative permeability defined as:

$$k_{rl} = S_l^{0.5} \left[ \left( 1 - \left( 1 - S_l^{b_{mu}} \right)^{\frac{1}{b_{mu}}} \right)^2 \right] \quad (4-10)$$

Figure 4-7 shows a comparison of the results of the pore network and the Van Genuchten model and the experimental data from the mass loss experiments for the materials CP1 and CP18. For both materials, the pore network model is more accurate than the Van Genuchten model. This proves not only the network is representative for intrinsic permeability simulation, but also for unsaturated scenarios the constructed network can provide a better result compared to the classical models. The advantage of the proposed framework lies in the fact that it contains more information and relevance from the material that is representing while such relevance and link is missing in case of empirical models. Note that the experimental trend for CP1 is unreliable because it shows that the unsaturated permeability is higher at lower degree of saturation. This is likely to be caused by experimental uncertainties [67, 111, 114].

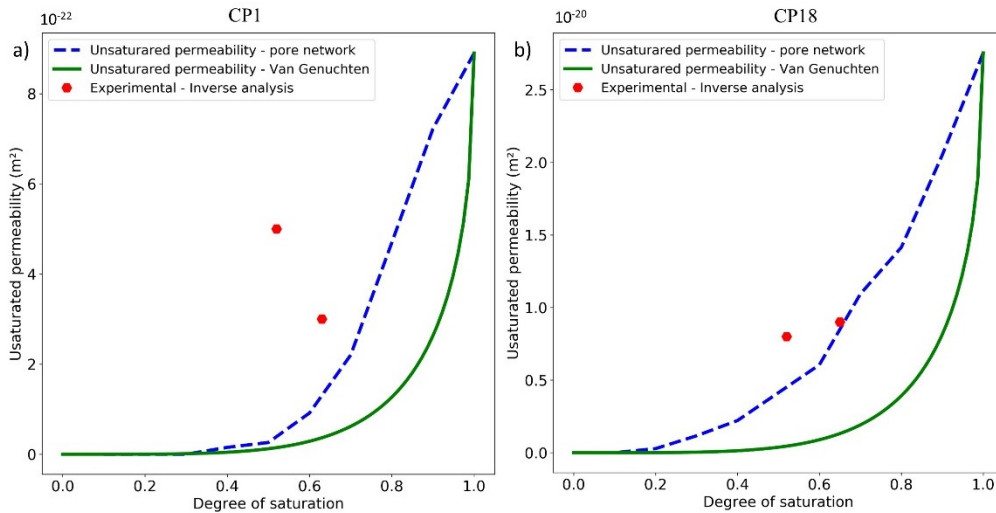


Figure 4-7. Unsaturated permeability estimated using pore network VS. experimental measurements

It is also worth noting that the unsaturated permeability estimated by pore network as well as the experimentally measured values remain in the same order of magnitude of the intrinsic permeability up to  $RH=0.5$ . At this relative humidity, pores with size of 12 nm are desaturated. Pores smaller than 12 nm are

mostly small capillary pores and gel pores. This indicates that gel pores are also contributing to the flow, even though because of their size they are weakly permeable, but their contribution is definitely not negligible this was also concluded in [119]. One additional conclusion to be drawn is that up to 50%  $RH$  the water permeability would still be in the range of intrinsic permeability indicating that moisture flow in the liquid phase is the major mechanism in this range as argued previously by multiple authors, to mention a few [67, 111, 114, 130]. In other words, no two-phase flow model is necessary to model moisture flow in unsaturated cement paste up to this  $RH$  level.

## 4.5 Conclusions

This chapter presents a new methodology for computation of intrinsic and unsaturated permeability of OPC-based cementitious materials. The proposed methodology utilizes a multiscale numerical framework starting from cement composition and its microstructure to constructing a hierarchical pore network and computation of the permeability. Moreover, a novel multi-algorithmic approach is developed to compute unsaturated permeability at different degrees of saturation.

The proposed approach is validated against an extensive number of experiments available in the literature and results are remarkably promising, indicating the flexibility and reliability of the framework.

In terms of disadvantage of the proposed framework, its reliance solely on microstructural modelling and all the initial inputs that are derived herewith could have a negative impact on the final estimation if the microstructure is not accurate in reporting the phase fractions. One additional limitation is the applicability of the framework on the blended systems because of the lack of

established microstructural modelling for these materials. However, CP2 in the studied materials includes 6% silica fume and estimated permeability is also fairly accurate. But applicability on systems with high percentage of additives such as limestone calcined cement [131, 132] remains uncertain.

# 5 Micromechanical analysis of mechanical and hydro-mechanical properties

---

## 5.1 Introduction

# Chapter 5

Concrete is a complex multiscale and multiphase material used in structural applications worldwide that its mechanical properties and performance has always been an important topic for researchers and industries to investigate. Given its complexity, various numerical and analytical frameworks have been proposed to compute mechanical properties of both sound and degraded states of the material. To mention a few recent studies in this area, Smilauer and Bittnar [133] studied a microstructure-based model in order to predict mechanical properties of hydrating paste. They utilized CEMHY3D for microstructural modelling and FEM and FFT for computation of Young's modulus. Mazaheripour et.al [17] used micromechanical modelling for estimation of Young's modulus using a lattice model. Their lattice model was verified with the results from FEM. They used HYMOSTRUC3D to generate a synthetic microstructure, which formed a basis for the micromechanical analysis. Lin Liu et.al [2, 134] studied drying behavior of cement paste using a multiscale framework and a lattice model at two different scales: (i) C-S-H, and (ii) cement paste level. While they used HYMOSTRUC3D to generate a synthetic microstructure, the C-S-H structure was modelled using a particle packing technique. A more detailed state of the art on microstructure informed micromechanical modelling is reviewed by Hongzhi Zhang et.al [16].

Even with significant advances in micromechanical modelling, material properties such as coefficient of thermal expansion (CTE) and drying shrinkage strains of cement-based materials have not been modelled within a numerical

micromechanical framework. although attempts have been made analytically, no numerical homogenization has been carried out. Furthermore, none of the studies discussed above and those reviewed by Hongzhi Zhang et.al [16] examine the stress field at the microstructure and concrete scale using a numerical micromechanical framework. Thus, this chapter describes a micromechanical framework that is adopted, firstly, to model mechanical properties of cementitious materials such as elastic modulus, Poisson's ratio and CTE, and secondly to examine the effect of drying shrinkage at cement paste and concrete levels. The aim of this analysis is to firstly provide a more informed insight on thermo-mechanical processes on lower scales i.e., microstructure, cement paste and concrete level, and secondly examine our current understanding of drying shrinkage at cement paste and concrete levels.

The computational framework is similar to some of the studies cited above wherein a hydration model is used to generate a synthetic microstructure that is consistent with cement hydration process, and the resulting microstructure provides geometrical input to a finite element model (FEM) in which mechanical, thermo-mechanical and hydro-mechanical analyses are carried out to determine the aforementioned properties.

## **5.2 Methodology**

### **5.2.1 Mechanical properties of hardened cement paste**

The mechanical properties under consideration are the Young's modulus and Poisson's ratio. These are determined by solving the boundary value problem of the standard conservation (balance of linear momentum) equation at the microscale assuming no body forces.

$$\nabla \cdot \boldsymbol{\sigma} = 0 \quad (5-1)$$

To determine the effective mechanical properties, the effective stiffness tensor  $\langle \mathbf{D}^{eff} \rangle$  has to be calculated as follows (e.g., Hain and Wriggers, 2008):

$$\langle \boldsymbol{\sigma} \rangle = \langle \mathbf{D}^{eff} \rangle : \langle \boldsymbol{\epsilon}_{el} \rangle \quad (5-2)$$

where  $\boldsymbol{\sigma}$  is Cauchy's stress tensor and  $\boldsymbol{\epsilon}_{el}$  is the elastic small strain tensor and the Macaulay brackets defined as follows:

$$\langle \blacksquare \rangle = \frac{1}{|\Omega|} \int_{\Omega} \blacksquare d\Omega \quad (5-3)$$

The effective mechanical properties are determined by subjecting the representative volume element (RVE) to boundary conditions that satisfy Hill's energy criterion relating the microscopic elastic energy to the macroscopic elastic energy (Hain and Wriggers [135]). Both linear displacement and uniform traction boundary conditions satisfies this criterion. In this study, linear displacement boundary condition is applied, which translates into the four sides of the RVE subjected to roller support boundary condition (Rigid Motion Suppression Boundary Condition) and displacement applied to only one side (e.g., top face in Figure 5-1). However, one side is left free (no constraints) in order to compute the Poisson's ratio.

Due to the heterogeneous distribution of various hydrated and unhydrated phases inside the RVE, some of the boundary elements may not have the same material properties. As clarified in Hain and Wriggers [136], if the boundary elements or voxels have different materials such as CSH, CH or unhydrated clinkers, then the linear displacement boundary condition violates local equilibrium at the boundary. However, this aspect has not been studied in this work.

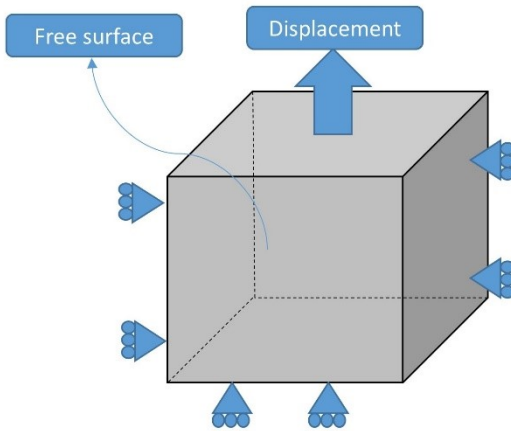


*Figure 5-1. Boundary Condition*

The mechanical properties for each voxel are assigned based on the phase distribution obtained from the micromechanical model. Initially, a comparative study on the size of RVE and its effect of final results on both microstructural modelling and computed mechanical properties is carried out. Implicit in this statement is that it is necessary to also run the microstructural model (cement hydration kinetics) for different RVE sizes, which will form a basis for the mechanical analysis. The RVE sizes studied are: 10, 20, 40, 60, and 80  $\mu\text{m}$ .

The microstructure of the bigger RVEs that are proven to be more representative [133, 135, 137] are directly exported to CAST3M [138] mesh. The mesh is an equally spaced, uniform grid, where each element or voxel corresponds to an 8-noded hexahedral element. Since the output from VCCTL is also voxel based, the transfer of information to CAST3M is rather straightforward.

### 5.2.2 Coefficient of thermal expansion

In order to determine CTE a similar approach as in section 5.2.1 is adopted, however, with a thermo-mechanical constitutive law as follows:

$$\langle \boldsymbol{\sigma} \rangle = \langle \mathbf{D}^{eff} \rangle : \langle \boldsymbol{\epsilon}_{Tot} - \alpha(T - T_0)\mathbf{I} \rangle \quad (5-4)$$

where  $\boldsymbol{\epsilon}_{Tot}$  is the total strain tensor, and the second term is the thermal strain tensor with  $T$  being the field temperature,  $\alpha$  the volumetric CTE,  $T_0$  the initial temperature and  $\mathbf{I}$  the identity matrix.

The boundary condition mimics free thermal expansion of the RVE. Accordingly, three surfaces are without constraints and three of them are prescribed with roller support boundary condition. Different phases in the RVE are assigned their specific CTE values and then a homogenous temperature change ( $T - T_0$ ) is applied on the RVE (every integration point). The average expansion  $\Delta V$  of the RVE is calculated by solving the conservation equation. The following formula allows calculation of the effective volumetric CTE,  $\alpha_{eff}$ .

$$\frac{\Delta V}{V} = -\alpha_{eff}(T - T_0) \quad (5-5)$$

with  $V$  is the initial volume.

### 5.2.3 Drying shrinkage strain

The drying shrinkage behaviour is studied both at the cement paste and concrete scales to understand the evolution of stresses in different phases of HCP as well as in the HCP phase in concrete as a function of drying. Prediction of drying

shrinkage strain of HCP as a function degree of saturation via a multi-mechanism approach has already been described in Chapter 3, which forms a basis for the study objectives stated above.

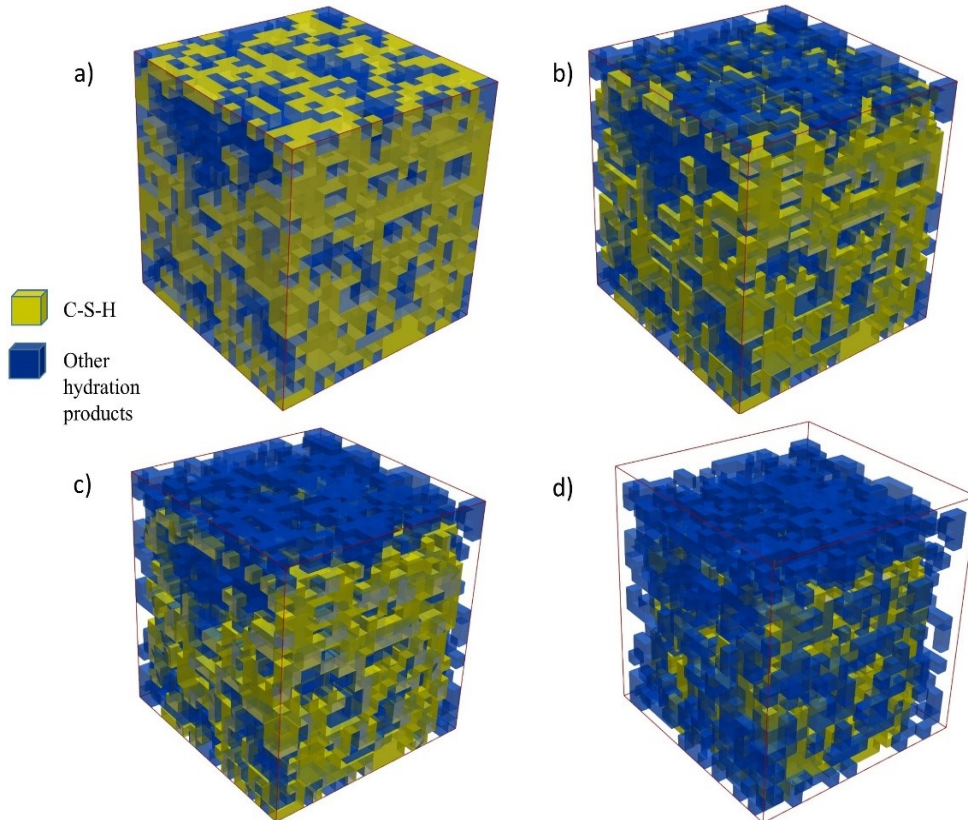


*Figure 5-2. Drying shrinkage simulated by contacting C-S-H phase. (a) fully saturated, (b) 80% saturation, (c) 70% saturation, (d) 50% saturation*

For the HCP micromechanical model, the C-S-H phase is assumed to be the only shrinking phase, which means other phases such as AFm, AFt, portlandite and unhydrated clinkers are assumed to not undergo any shrinkage (they are the constraint). Thus, for a given material composition, first, the total drying shrinkage strain of the HCP is determined from the multi-mechanism model for various degrees of saturation (Chapter 3). The strain in the C-S-H phase is calibrated until the total drying shrinkage strain computed from the multi-

mechanism model for the given material is reached. For instance, if the volumetric free drying shrinkage strain at a given degree of saturation is  $100 \mu\text{m/m}$ , the RVE of the HCP also experiences the same shrinkage as a whole, but the C-S-H gel as the sole shrinking phase would contract more than the computed value via the multi-mechanism model because it occupies only a portion of RVE. Regarding the assumption of C-S-H as the shrinking phase it should be noted that since C-S-H is matrix of the HCP and it contains majority of the pore space this assumption is not far from reality.

In simulation of drying shrinkage at concrete level, it is assumed that HCP is the only shrinking phase and not the aggregates. The shrinkage of HCP as a function of degree of saturation is calculated by means of the multi-mechanism model and is directly imposed on HCP in the concrete RVE to compute the total shrinkage of concrete.

The micromechanical boundary conditions for the analysis of both HCP and concrete are the same as for the CTE example (Section 5.2.2), i.e. to mimic unconstrained shrinkage. The calibration of the shrinkage strain for the C-S-H phase in case of cement paste RVE and imposition of shrinkage strain for the HCP phase in case of concrete RVE are achieved using the same thermo-mechanical framework by suitably adjusting the CTE and temperature gradient values (Section 5.2.2).

Figure 5-2 illustrates drying shrinkage strain experienced by the microstructure for the following scenarios: fully saturated, 80%, 70%, and 50% of drying.

## 5.3 Validation and discussion

### 5.3.1 Cement Composition

The studied material is a CEM I with composition as reported in Table 5-2 [100, 106, 139]. The results achieved by solving cement hydration kinetics for five different RVEs (Table 5-1) show that the average phase fraction estimated by VCCTL is not significantly affected for 20  $\mu\text{m}$  RVE and above, however, converges at and above 60  $\mu\text{m}$ .

*Table 5-2. Chemical composition(%mass) of the studied material and its curing method ([10-12])*

Material	C3S	C2S	C3A	C4AF	W/C	Curing method	Experimental method
N55	0.62	0.18	0.056	0.1	0.55	Saturated conditions for 91 days (100% RH)	Climate chamber with $h$ control using sodium hydrate solution T=20°C

*Table 5-1. Results of microstructural modelling for different RVE sizes (%volume)*

Size of RVE	DoH	C-S-H	Total Porosity	CH	Clinker	AFt +Ettringite	AFm
10 $\mu\text{m}$	0.92	0.47	0.27	0.15	0.04	0.07	0.01
20 $\mu\text{m}$	0.92	0.47	0.27	0.15	0.04	0.07	0.01
40 $\mu\text{m}$	0.90	0.47	0.27	0.145	0.04	0.07	0.01
60 $\mu\text{m}$	0.88	0.45	0.28	0.145	0.04	0.07	0.01
80 $\mu\text{m}$	0.88	0.45	0.29	0.14	0.04	0.07	0.01
100 $\mu\text{m}$	0.875	0.45	0.29	0.14	0.04	0.07	0.01

### 5.3.2 Mechanical properties

Linear displacement is applied as shown in Figure 5-1, including the remaining mutually perpendicular directions so as to determine Young's modulus in XYZ directions and the average Poisson's ratio. Mechanical properties of various HCP phases are already reported in Table 3-3 in Chapter 3. The topological arrangement of phase fractions are different as the size of RVEs increases as shown in Figure 5-3.

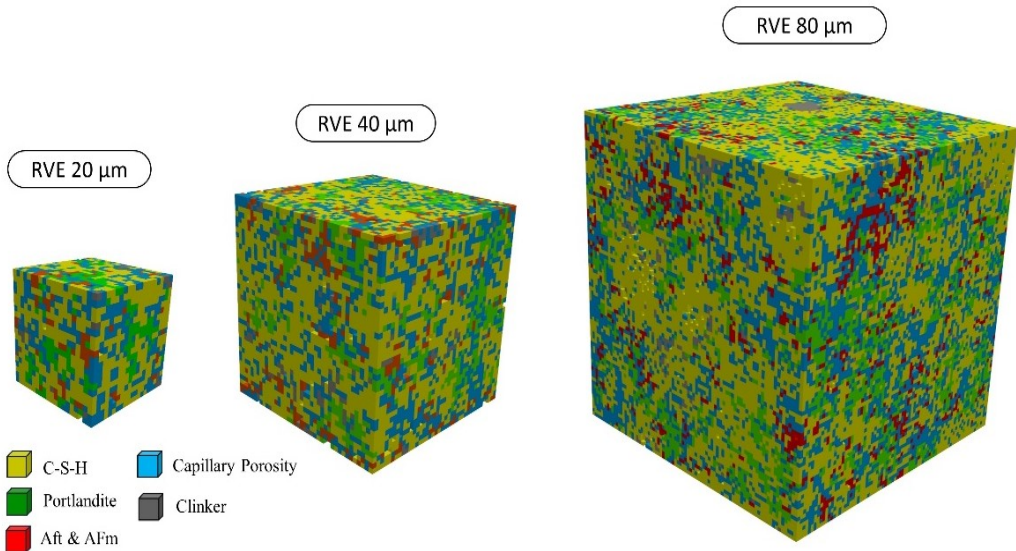


Figure 5-3. Different RVEs with various topological arrangements (N55, CEM I).

Table 5-3 shows calculated vs. experimental mechanical properties [140]. It is seen that the calculated values show a convergence for a RVE size of 40  $\mu\text{m}$ . In terms of accuracy, the results are in good agreement with experimentally measured modulus, indicating the reliability of the numerical homogenization method as well as the coupling of cement hydration kinetics model with FEM analysis.

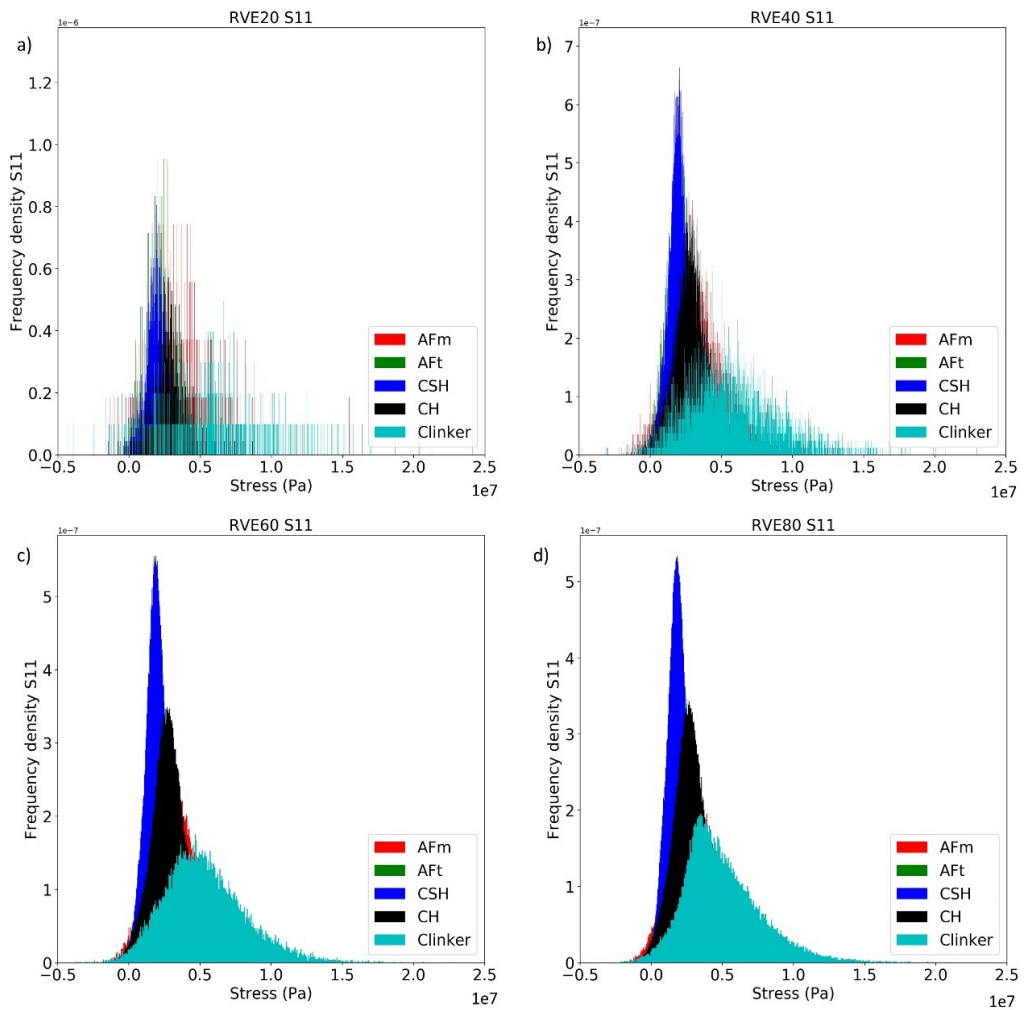


Figure 5-4. Stress distribution of different phase fractions under a uniaxial tensile loading (N55, CEM I)

Table 5-3. The mechanical properties computed for different RVE sizes (N55, CEM I).

REV size	10μm	20μm	40μm	60μm	80μm	Experimentally measured values ([13])
E modulus	E <sub>x</sub> =16.6	E <sub>x</sub> =16.8	E <sub>x</sub> =16.8	E <sub>x</sub> =16.5	E <sub>x</sub> =16.5	15.1
	E <sub>y</sub> =17.8	E <sub>y</sub> =15.9	E <sub>y</sub> =16.9	E <sub>y</sub> =16.6	E <sub>y</sub> =16.4	
	E <sub>z</sub> =17.5	E <sub>z</sub> =16.7	E <sub>z</sub> =16.5	E <sub>z</sub> =16.5	E <sub>z</sub> =16.4	
Poisson ratio	0.27	0.26	0.26	0.26	0.26	0.26

In addition to the effective mechanical properties, in order to investigate the mechanics of microstructure, the stress distribution in all the phases are examined. Since cementitious materials demonstrate a quasi-brittle behavior, tensile stress is known to be critical value to account for possible damage and failure. Therefore maximum tensile stress (first principal stress denoted in figures as  $S_{11}$ ) is chosen as the variable for discussions [16, 141, 142]. Figure 5-4 shows the frequency density of the first principal stress evaluated in the RVE. As expected, the higher the young modulus of a given phase, the higher the stress level. Accordingly, the highest to lowest stress values follow the order: clinker, AFt phases, Portlandite (CH), C-S-H and finally pores, respectively.

In terms of RVE choice and its effect on computed stress distribution, it is strikingly interesting to notice that even though the bigger RVE leads to smoother stress distribution and consequently less discontinuities, the mean stress values are similar for all RVEs. This explains why the classical analytical homogenization techniques can also to some extent capture the general properties of the material, for example, Young's modulus, as long as the stress range remains in elastic regime [133, 142-144]. Note that stress distributions are best analyzed with larger RVEs.

### **5.3.3 Coefficient of thermal expansion**

An arbitrary  $(T-T_0)$  field is imposed on the RVE as the CTE results do not depend on the temperature difference in the elastic regime. Furthermore, CTE values are computed in three mutually perpendicular directions. Similar to the mechanical properties discussed in Section 5.3.1, calculated CTE values also reveal that

convergence is reached with an RVE size of 40  $\mu\text{m}$ , which is much faster to simulate as well as post-process compared to the 100  $\mu\text{m}$  RVE, and results are not significantly different as seen in *Table 5-4*. The CTE results correspond very well with experimentally measured value [139].

*Table 5-4. Computed CTE for different RVE sizes (N55, CEM I).*

REV size	10 $\mu\text{m}$	20 $\mu\text{m}$	40 $\mu\text{m}$	60 $\mu\text{m}$	80 $\mu\text{m}$	Experimentally measured value ([12])
<b>Properties</b>						
Coefficient of thermal expansion ( $\mu\text{m}/\text{m}$ )	CTE <sub>x</sub> =	20				
	25.1	21.9	21.5	21.6	21.1	
	CTE <sub>y</sub> =	CTE <sub>y</sub> =	CTE <sub>y</sub> =	CTE <sub>y</sub> =	CTE <sub>y</sub> =21.0	
	21.5	21.5	21.2	21.6		
	CTE <sub>z</sub> =					
	26.1	21.6	21.4	21.7	21.0	

Due to the imposed temperature difference thermal stresses arise in the RVE. For the same reason described in Section 5.3.1, the first principal stress (denoted as S11) is chosen as the variable for further discussions as shown in Figure 5-5. It is interesting to note that the stress distribution for thermal loading is different from the distribution associated with mechanical loading. Here, the AFm phase has the highest stress values compared to the others because of their high CTE and also relatively high Young’s modulus. Similar to the previous analysis (Section 5.3.1), for the thermo-mechanical analysis, it is observed that mean stress values remain in the same range even if RVE size changes because the material behaviour remains in the linear range.

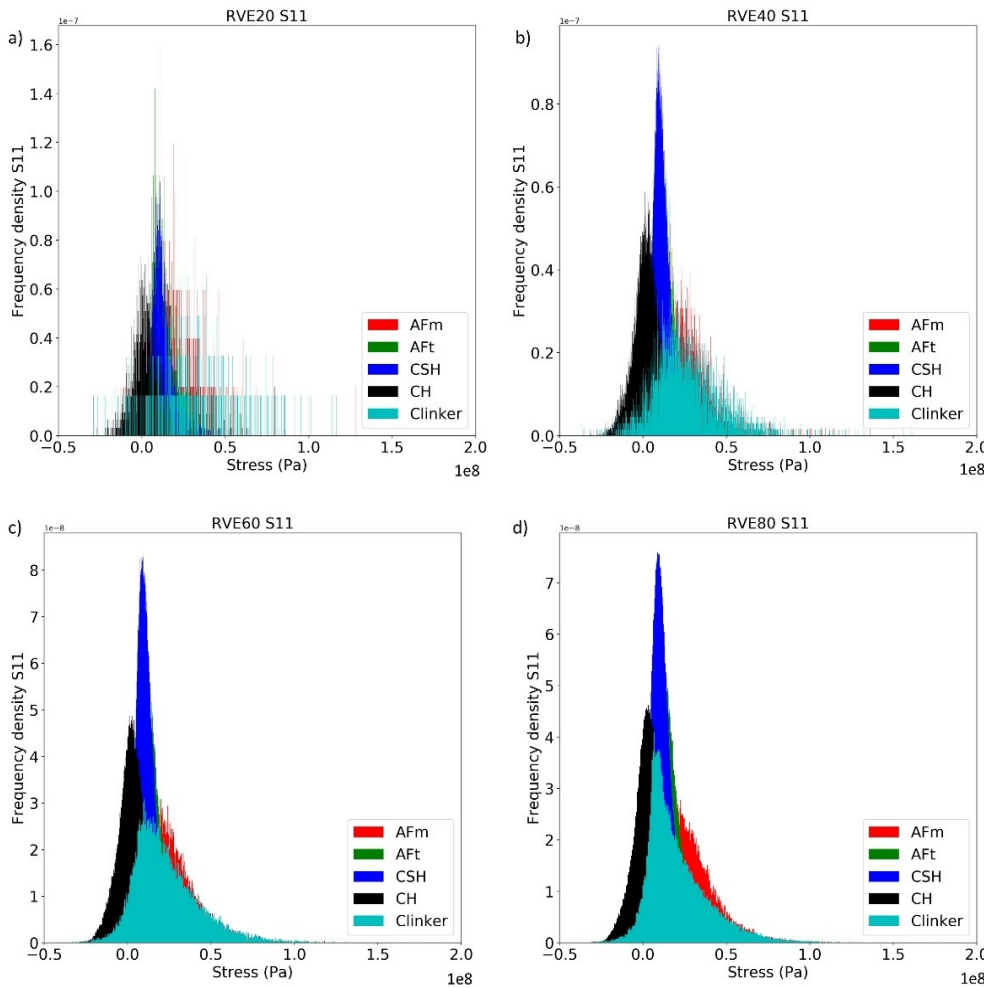


Figure 5-5. Stress distribution of different phase fractions under uniform thermal (N55, CEM I) expansion

### 5.3.4 Drying shrinkage

#### 5.3.4.1 Drying shrinkage – cement paste level

Since C-S-H is the only shrinking phase, the other hydration products would restrain the contraction of C-S-H, thus the stress build up in the C-S-H phase is

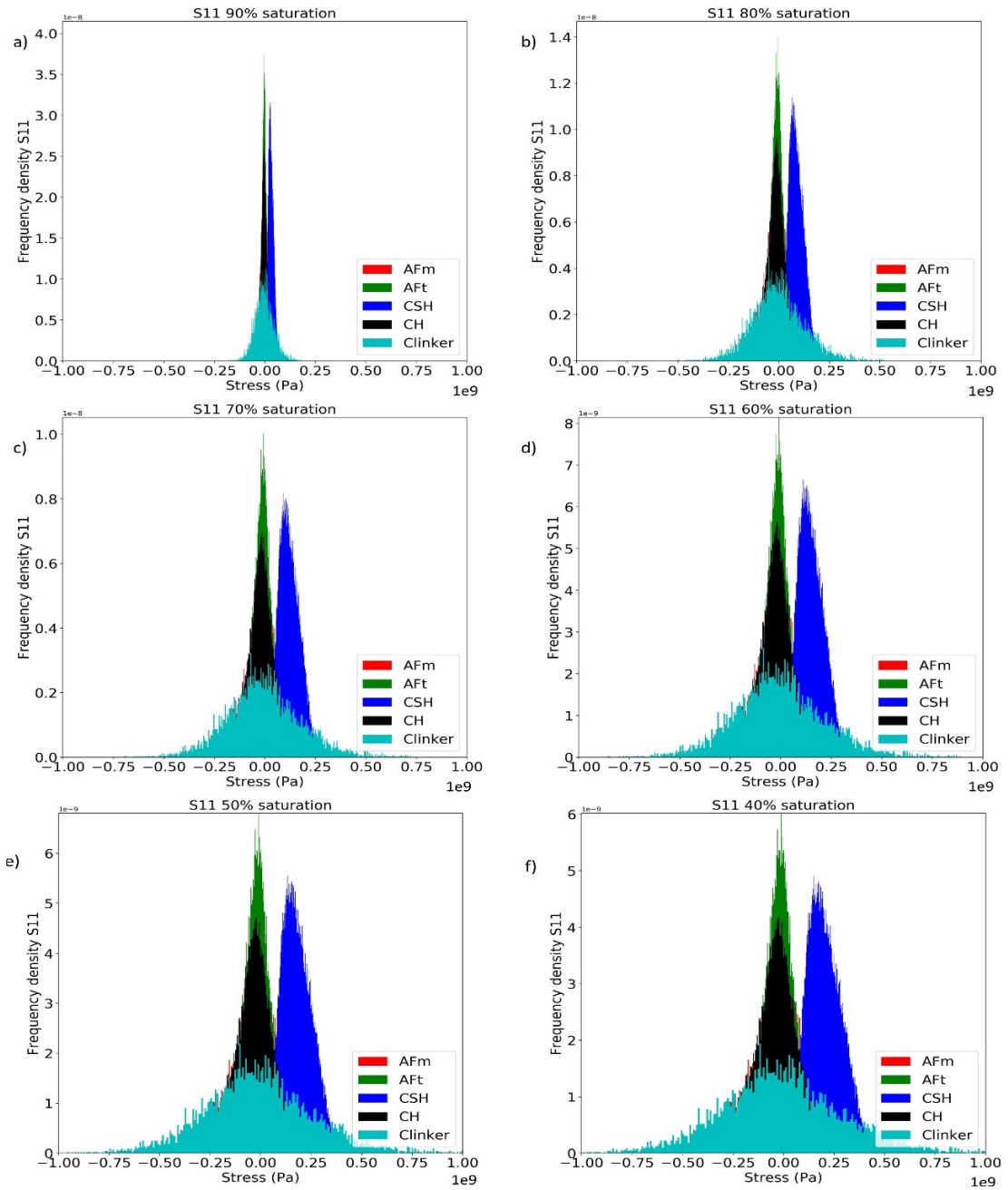


Figure 5-6. Drying shrinkage at cement paste level with C-S-H as the only shrinking phase (N55, CEM I)

always tensile (positive), while all the other phases experience compressive stress (negative) and this behaviour will amplify as the degree of saturation drops

because the drier the system is, the higher the tensile stresses and hence correspondingly the compressive stresses [2, 15, 75, 134].

The first principal stress distribution of all the phases are shown in Figure 5-6. The results show that as the degree of saturation reduces the stress values rises and the stress distribution evolves into a wider distribution for all the phases. It is also worth noting that as the material dries out the stress level for C-S-H moves toward higher tensile stress values while the remaining phases experience a higher compression stress values (moving towards left side). A quantitative comparison on mean maximum tensile stress values as a function of degree of saturation reveals that stress level changes drastically for C-S-H phase during

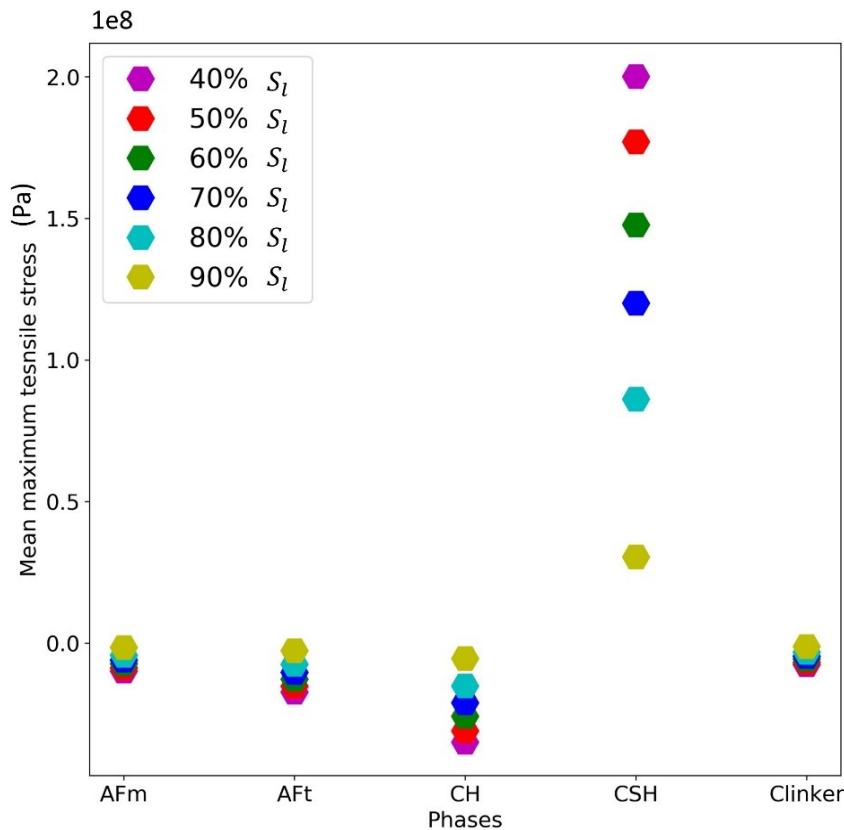


Figure 5-7. Mean maximum tensile stress values for different phases at different degree of saturation (N55, CEM I)

the course of drying while the variation of mean compression stress on other phases is not as pronounced as demonstrated in Figure 5-7.

Therefore, as expected the phase prone to damage first and experience cracking is C-S-H gel. Hence, a deeper look into the C-S-H phase stress distribution as function of drying would reveal more details on possible damage and crack initiation in cement paste level. This is further demonstrated in Figure 5-8 (stress

components denoted as  $\sigma = \begin{bmatrix} S_{xx} & S_{xy} & S_{xz} \\ S_{yx} & S_{yy} & S_{yz} \\ S_{zx} & S_{zy} & S_{zz} \end{bmatrix}$ ) for both normal and shear stress

components of C-S-H gel. The trend that is apparent during drying is the increase of mean normal stress values. This can be seen in the form of a considerable shift of normal stress components distribution curves towards the higher mean values (right side) as also shown in Figure 5-7, while the shear stress remains on mean values of zero because of volumetric nature of the shrinkage and free shrinkage boundary condition assumed here. Additionally, the stress distribution curves get wider throughout the drying course, which means more local extremums, and local extremums in microstructure means more locally self-equilibrated forces in the microstructure and consequently more microcracks [12, 145, 146]. This was hypothesized by some of the pioneers in the field such as Bazant and BENBOUDJEMA but in the author's knowledge not been quantitatively reported.

In terms of quantitative stress values, it is interesting to note that if pure elastic behavior for all the phases is assumed then drying shrinkage induced stress values are extremely high for C-S-H and given the fact that cement paste demonstrates a quasi-brittle behavior the high tensile stress values can lead to damage and failure. The maximum tensile stress for C-S-H gel is illustrated in Figure 5-8 (e) (denoted as S11) and it is shown that mean maximum tensile stress

by drying range of 70% saturation would exceed 100 MPa and this value would double by drying the material up to 40% saturation. Note that Hlobil et.al [142] have reported the tensile strength of C-S-H gel to be 66 and 107 MPa, respectively, for LD and HD C-S-H gel. Nemecek [147] have measured these values (tensile strength of C-S-H) to be as high as  $264\pm 70$  and  $700\pm 199$  MPa, while Shahrin and Bobko [148] in a recent work measured and reported similar values for compressive strength of C-S-H gel (225–606 MPa). It is widely observed and accepted that compressive strength of cement paste is much more than its tensile strength [12].

Since the mechanical behaviour of C-S-H gel is not very well established it is not possible to draw a definite conclusion but what is apparent is that even if a high tensile strength is assumed for C-S-H gel, for instance, 150 MPa, then this value is already surpassed by lowering the saturation to 70%. Therefore, drying shrinkage (at lower degree of saturation i.e., 70%) at microstructure level is probably accompanied by cracking and creep. The main reason for the first one is that shrinkage is accompanied by high tensile stress values and due to low permeability of cementitious materials drying does not occurs uniformly, consequently this high local stress values are self-equilibrated by microcracking, which was also argued in [12]. While the latter happens due to presence of water in gel pores (gel pores are saturated up to a drying range of 40%-50%) and high value stress field that facilitates sliding creep mechanism in C-S-H gel. Additionally, Bazant argues in his microprestress theory that by drying, the water pore pressure changes that would alter the disjoining pressure in the gel pores and this phenomenon eventually helps the sliding and creep [12, 25].

These observations and conclusions also explain the drying creep effect also known as Picket [146] effect where the material under drying experiences an intensified creep deformation compared to sealed and saturated material (basic creep), the reason as explained is that drying shrinkage (even free drying

shrinkage) itself accompanies creep and microcracking. Therefore, when the mechanical load is applied it is applied on an already creeping material with microcracks therefore the measured drying creep is neither solely due to external mechanical loading nor shrinkage but a mixed effect of both. In this regard, Bazant argues that a proper drying shrinkage test is to be conducted on 3 mm sample over the course of two years in order to overcome the non-uniform drying and effect of microcracking [12]. Such experimental data is not available in the literature but given the results acquired here, one can speculate that even if non-uniform drying and its consequential microcracks are avoided, the stress level over the course of drying would simply surpass the elastic bound of C-S-H (even if highest value reported is assumed i.e., 260 MPa it would be surpassed by 50% sat). Hence, the drying shrinkage would also affect the creep behavior of cementitious materials regardless of its size. Clearly if the effect of microcracking is eliminated, the effect of drying shrinkage on creep behavior would be also less prominent and this has never been shown and discussed quantitatively in the literature.

Nevertheless, the stress distribution of cement paste at microstructure level during drying shrinkage has not been available prior to this research and that is why these information bring further insights into the possible explanation and justification for the material behavior. However, further refinements and experimental validation would also help to confirm the above conclusions.

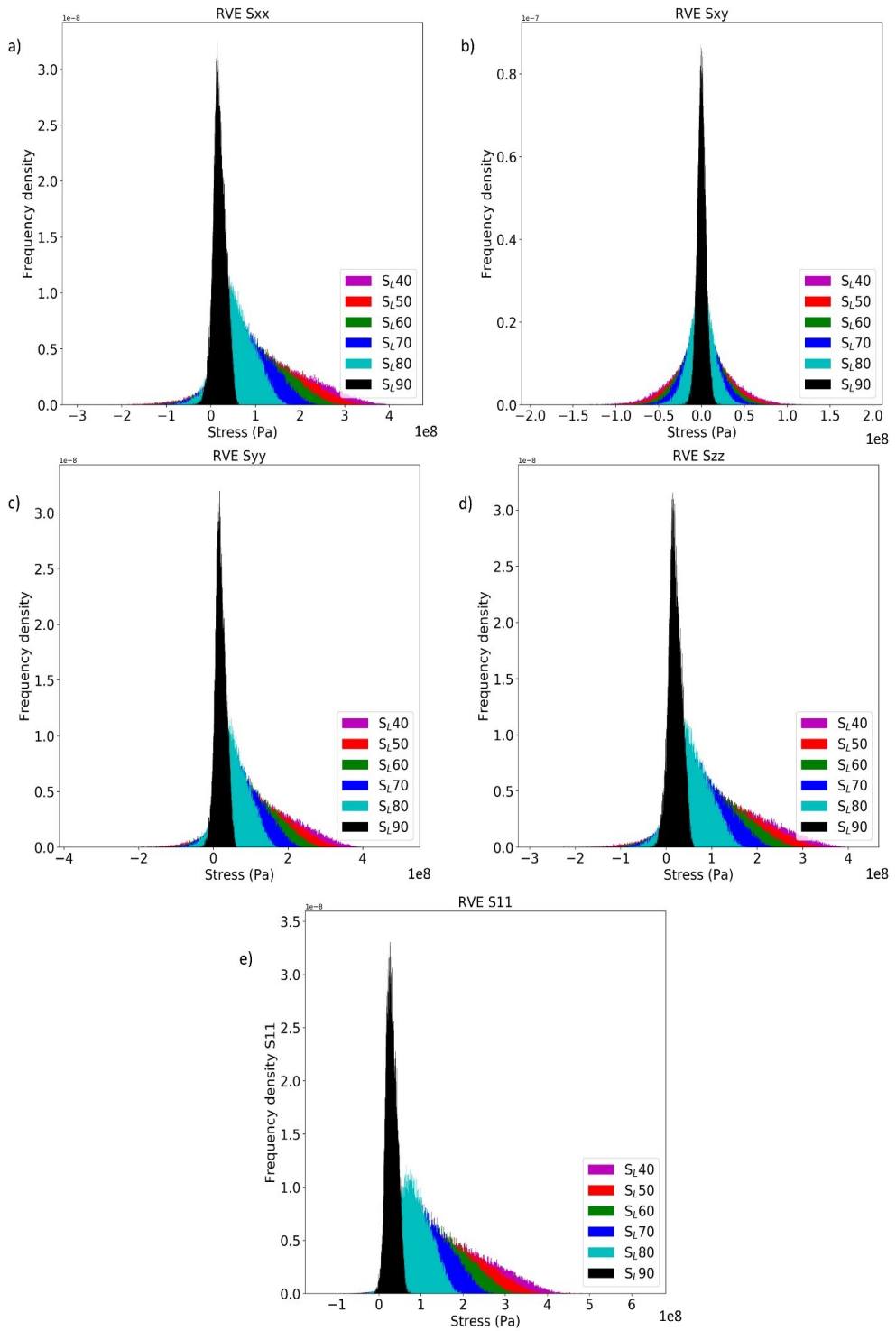


Figure 5-8. Stress distribution in C-S-H gel over the course of drying.  $S_L$  denotes degree of saturation% (N55. CEM I).

### 5.3.4.2 Drying shrinkage – concrete level

This section exclusively studies the shrinkage for the material composition of the concrete buffer of the Supercontainer concept [4, 70]. The studied material composition is a self-compacting concrete (SCC) with material design reported in Table 5-5.

*Table 5-5. Material composition of the studied SCC ([27])*

Material	Amount (kg/m <sup>3</sup> )
<b>Cement CEM I/42.5N HSR</b>	350
<b>Limestone filler</b>	100
<b>Limestone 0-4</b>	840
<b>Limestone 2-6</b>	327
<b>Limestone 6-14</b>	559
<b>Superplasticizer</b>	10
<b>Water</b>	175

As the largest aggregate size is 20 mm, an RVE size of 60 cm is chosen. This RVE is constructed based on aggregate size distribution available for the concrete material [4]. Therefore, randomly shaped aggregates with a size distribution in accordance with Table 5-5 [4] are embedded in a meso-structure, which represents the material at concrete level.

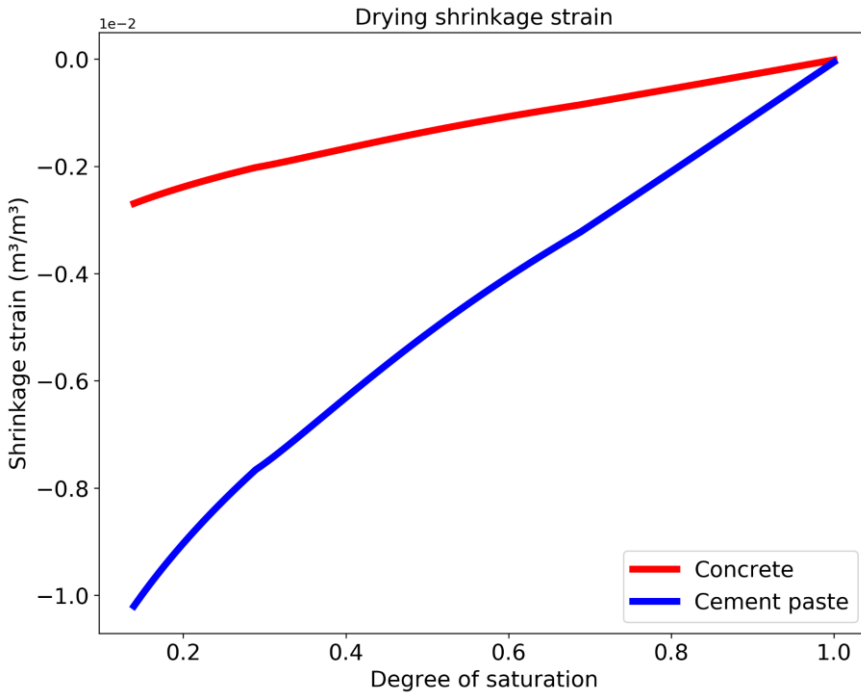


Figure 5-9. Drying shrinkage of cement paste and concrete level for Supercontainer, material composition as (I271)

The shrinkage strain as a function of degree of saturation for the cement paste phase is computed from the multi-mechanism model (Chapter 3) for the given material composition (Table 5-5), which is plotted as the blue curve in Figure 5-9. These strains are applied to the cement paste phase of the concrete RVE. Then, the total shrinkage of concrete is calculated by solving the conservation equation (Section 5.2.3). The drying shrinkage as a function of saturation for both cement paste and concrete are shown in Figure 5-9. Also, the stress distribution of the cement paste phase is computed as a function degree of saturation (Figure 5-10), which is similar to C-S-H phase at the cement paste level.

It is a valid assumption that cement paste is the only shrinking phase in concrete level and aggregates restraining the shrinkage [12]. Therefore, the stress induced

in the cement paste during the drying is always tensile while aggregates are under compression. The same observation is noted at the cement paste level between C-S-H gel as shrinking phase and other hydration products as restraints (Section 5.3.3). Given the quasi brittle behavior of the cement, the tensile stress is assumed as a critical loading and controls the failure mechanism of the material as well [12, 16]. It is also apparent that with increase in drying (lower degree of saturation), higher tensile stresses are induced in the cement paste (Figure 5-10). It is also interesting to note that stress distribution follows a similar trend to the microscale level as the drying continues, i.e., the stress distribution expands more. Quantitatively, also the stress levels if interpreted by pure elastic approach would be really high as shown in Figure 5-10 (e). The mean value for maximum tensile stress would range from 10 to 50 MPa for a drying range of 90% to 40% saturation. This is while the tensile strength of hardened cement paste usually ranges between 2-20 MPa [149-153] at cement paste level. This leads to the same conclusion as previous section for microstructure level but since the tensile strength of cement paste is much lower than the C-S-H gel even considering the most optimistic reported value by Qian [149] i.e. 20 MPa, the drying shrinkage at concrete level seems to be even more critical than at the microstructure level.

These observations confirm all the previously concluded details of drying shrinkage at microstructure level. However, at the concrete level since the properties of cement paste are well-documented and measured it can be concluded that drying shrinkage at concrete level is always accompanied with microcracking and creep. The microcracking is due to low permeability of hardened cement paste and its consequent non-uniform moisture field and finally self-equilibrated stresses, while the latter is because of presence of water in the paste and high stress values, which cannot be endured by purely elastic response of the cement paste. While the conclusions at microstructure are not easy to validate due to a lack of information on properties of C-S-H gel, the conclusion

for concrete level are more definite. Since both, the microcracking and creep phenomenon are also involved in drying shrinkage and even in free drying shrinkage scenario (like the RVE here), it is also worth mentioning that the classic drying creep deformation is not solely due to external mechanical loading but drying shrinkage with initiating microcracks and creep intensifies the measured value for drying creep.

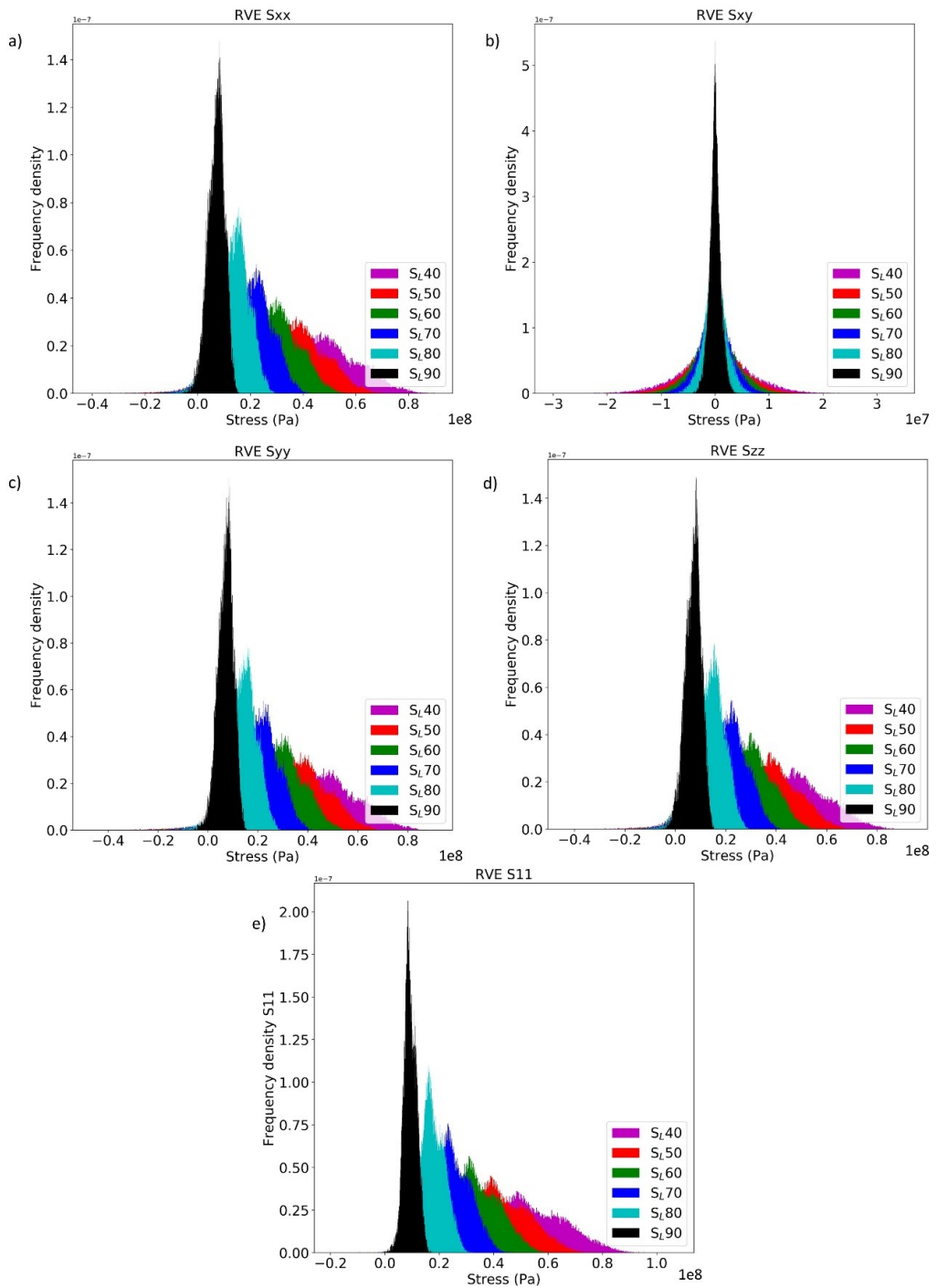


Figure 5-10. Stress distribution of cement paste over the course of drying for at concrete level for the studied material (Supercontainer)

## 5.4 Conclusions

In this chapter a numerical micromechanical framework is hired to compute thermo-mechanical properties of cementitious materials at two scale of cement paste and concrete. In addition, a detailed quantitative study on micromechanical behavior of cement paste and concrete under thermo-mechanical evolution is conducted. Finally, the developed framework is utilized to investigate the drying shrinkage behavior of cementitious materials at two different scales of cement paste and concrete level where new insights are presented.

The developed framework can accurately compute the thermo-mechanical properties of hardened cement paste and concrete this is evident in the validation section. The results of the final section of this chapter are utilized for large scale thermo-hydro-mechanical simulation in the next chapter where drying shrinkage plays an important role.

It is important to state that the microstructure developed by the cement hydration kinetics models such as VCCTL are not the true microstructure and hence stress distributions can be better analyzed using the actual 3D images.

## 5.5 Acknowledgements

The work presented in this chapter has been conducted during my research Visit at Prof. Dr. Farid Benboudjema's lab (LMT Ecole normale supérieure Paris-Saclay) and under his direct supervision. His kind help and persistent supervision is greatly appreciated and acknowledged. This work has been partially supported by the ENEN+ project that has received funding from the EURATOM research and training Work Programme 2016 – 2017 – 1 #755576.

# 6 A Multiscale Approach to Model Thermo-Hydro-Mechanical Behaviour of non-reinforced Concrete

---

## 6.1 Introduction

# Chapter 6

In this chapter the thermo-hydro-mechanical behavior of Supercontainer, a case study relevant to our interest is carried out. The overarching goal of the series of numerical analyses to be carried out within this PhD program is to simulate the 2<sup>nd</sup> half scale test of the Belgian concept of Supercontainer (SC) [4, 70]. There are two half scale (not strictly half scale) tests that have been carried out so far. The first half-scale test (HST1), performed in 2009, demonstrated to a large extent that the SC can be constructed using available industrial techniques [4, 70, 154]. HST1 also studied early-age behaviour of the concrete buffer of the Supercontainer during the different construction stages, with and without thermal load, and to evaluate the possible risk of early-age cracking (macrocracking). However, micro-cracks were formed on the surface of the concrete buffer during the heating phase of HST1. The absence of a dedicated crack-monitoring system precluded defining the exact time of initiation, evolution and depth of penetration of these micro-cracks.

To build further on the knowledge acquired in HST1, a second test (HST2) was performed in 2013, which is the focus of this PhD study. Some of the objectives of this test were (i) to further investigate the feasibility of constructing the SC, and (ii) to advance our understanding of the thermo-mechanical behaviour of the self-compacting cementitious (concrete and mortar) materials, (iii) modifying operational aspects of concrete mixing and casting to prevent the formation of a

transition casting joint as observed in HST1, (iv) testing a new filler composition with reduced modulus of elasticity to lower the risk of cracking in the buffer.

The experimental mock-up weighed approximately 32 tons and consisted of two main construction phases. Phase 1 carried out the construction of a massive non-reinforced concrete buffer using a self-compacting concrete (SCC) mixture. This construction phase created a concrete buffer with an inner cavity large enough to hold a carbon steel overpack, as specified in the Belgian conceptual design. In Phase 2, a pre-heated carbon steel overpack was inserted into the existing cavity of the buffer and the free space in the cavity was subsequently filled with a cementitious filler (assumed to be the same SCC here). The preheated overpack contained a heat source to simulate the heat emitted by a real canister. Phase 1 is beyond the scope of this study. The main focus is therefore on the Phase 2 analysis where concrete buffer is matured and thermal load is active (Table 6-1).

*Table 6-1. Timeline of HST2*

<b>Phase</b>	<b>Day</b>	<b>Milestone</b>
Phase 1	0	Cast concrete buffer
Phase 1	6	Removal inner mold
Phase 1	29	Removal outer mold
Phase 2	56	Cast filler & start heating
Phase 3	133	Shut OFF heater

Figure 6-1 shows Supercontainer at different stages of construction. It is worth noting that hydration of filler and lid which are added as in Figure 6-1 (b.2) and (c) are not taken into account in the simulation.

From a numerical point of view, a fully coupled THM analysis, however, in a stepwise manner to understand the importance of individual processes on the

cracking potential of the buffer is conducted. This mainly constitutes a 2D axisymmetric analysis Figure 6-2.

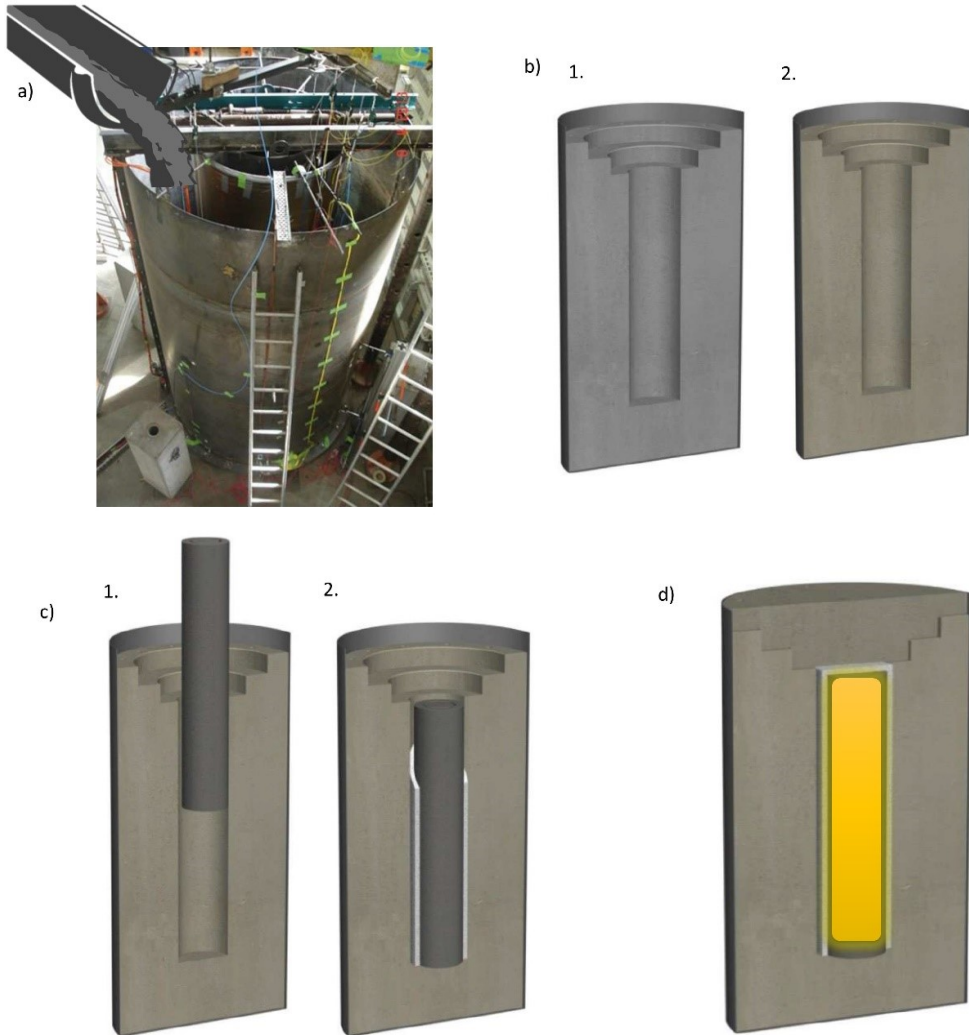


*Figure 6-1. Supercontainer at different stages of construction, (a) casting fresh concrete in the mold, (b.1-2) concrete matures and mold is removed, (c.1) insertion of Carbon steel overpack, (c.2) casting the filler (SCC) between the overpack and structure, (d) installation of the lid and initiation of thermal loading – case study of this chapter.*

## 6.2 Description of the simulation

As mentioned the main goal of this study case is to firstly demonstrate the application of the developed multiscale framework (Chapter 2 to 5) and secondly to investigate the main contributors to the observed cracks during HST2 [155].

### 6.2.1 Geometry

The studied geometry is a 2D axisymmetric analysis of SC as illustrated in Figure 6-2. Additionally, there are four investigation points defined as in Figure 6-2 (b) where the actual evolution of temperature, degree of saturation and damage are available from in situ sensors. The mesh is as in Figure 6-2 (c), where each

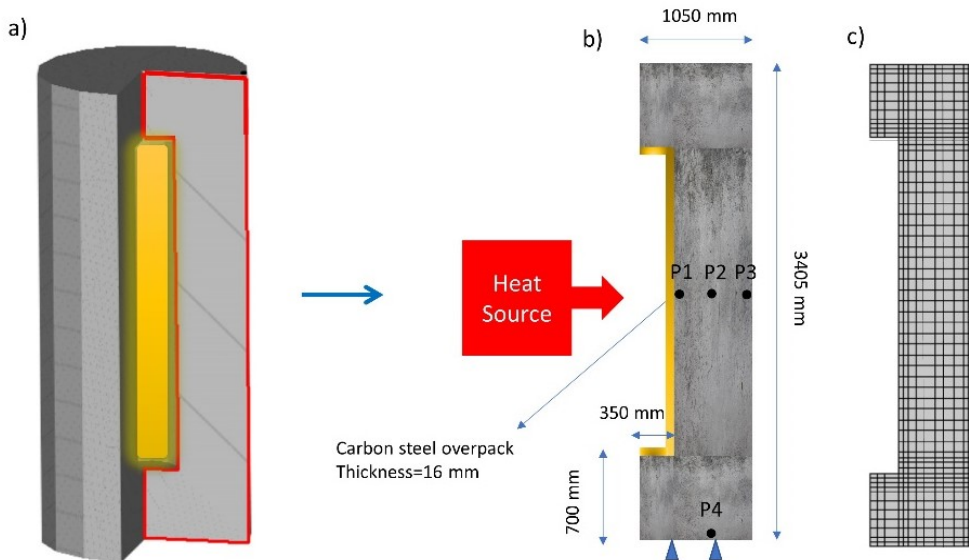


Figure 6-2. 3D geometry (a), studied geometry with investigation points P1-P4 (b), studied mesh (c).

element corresponds to an 8-noded quadrilateral element. The analysis has been done using finite element software CAST3M [138].

### 6.2.2 Initial conditions

Initial conditions are imposed in accordance with experimental procedure. The initial saturation degree is estimated with VCCTL with assumption of sealed hydration for 56 days. The input parameters are cement composition, w/c, curing and the output is the resulting microstructure which contains volume fraction of each phase and degree of saturation based on the curing method.

*Table 6-2. Initial conditions of simulation*

Initial conditions	
Thermal	
Temperature (T)	20 °C – inside and outside
Hydraulic	
Saturation Degree	91% - <a href="#">Hydration model</a>
Mechanical	
Mechanical loading	Self-weight loading

### 6.2.3 Boundary conditions

Boundary conditions are imposed in accordance with the experimental procedure.

Table 6-3. Boundary condition applied on the geometry

Boundary conditions	
Thermal	
Temperature	20 °C – outer shell (ambient condition)
Thermal loading	Heat source in canister - 300 (W/m)
Hydraulic	
Relative humidity	Ambient - 78%

## 6.2.4 THM governing equations

THM governing equation, which are also well-established [156-159] in the literature are briefly elaborated in this section.

### 6.2.4.1 Heat (thermal) transport

The thermal field in concrete can be computed based on the energy conservation law.

$$\rho C_t \frac{\partial T}{\partial t} = q_h - \nabla \cdot \mathbf{Q} \quad (6-1)$$

where  $\mathbf{Q}$  is the heat flux,  $q_h$  is heat source (heat of hydration, if concrete is not mature),  $\rho$  is the density and  $C_t$  is the specific heat capacity of concrete. Since the concrete is weakly permeable it is assumed that the heat transfer in concrete due to migration of liquid water and water vapour is negligible (convection is ignored). Therefore, the heat transfer equation here is the same as Fourier's law:

$$\mathbf{Q} = -\lambda_t \nabla T \quad (6-2)$$

with  $\lambda_t$  being the thermal conductivity of concrete at saturated state. However, there are empirical expressions proposed to account for temperature and saturation variation effect on  $\lambda_t$  [59, 157-159]. It is argued that assuming a constant  $\lambda_t$  will not affect the accuracy of the model significantly [12]. The heat flux on the boundaries is due convection mechanism as follows:

$$\mathbf{Q} \cdot \mathbf{n} = h_t (T - T_{env}) \quad (6-3)$$

Where  $T$  is the temperature of concrete structure,  $T_{env}$  is ambient temperature,  $h_t$  is heat convection factor, which depends on environmental conditions such as air circulation or liquid cooling during test, here it is the natural air circulation with wind velocity less than 1 m/s (5.6 W/m<sup>2</sup>/K). In terms of internal thermal loading, there were two potential options as 50 and 70 years old waste with heat flux of respectively 360 and 240 (W/m) and the experiment was conducted using a heat source with 300 W/m. [4, 71], and hence simulations discussed further refers to this wattage.

#### 6.2.4.2 Moisture transport

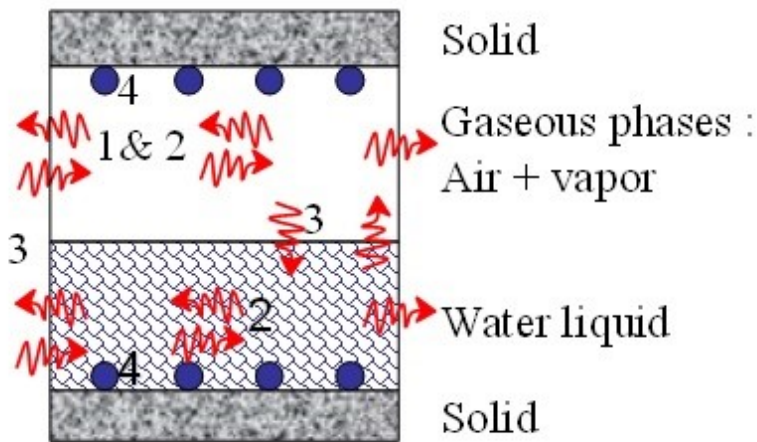
Since the external metallic mold is removed before thermal loading the moisture transport with environment is made possible in HST2. The moisture transport is modeled using the mas balance equation. Concrete is considered as partially saturated because of self desiccation as well as exchange of moisture with atmosphere. Mass balance equations for liquid water, water vapor and dry air are defined via:

$$\dot{m}_l + div(m_l \mathbf{v}_l) = -\dot{m}_{vap} - \dot{m}_{hyd} \quad (6-4)$$

$$\dot{m}_v + \text{div}(m_v \mathbf{v}_v) = \dot{m}_{vap} \quad (6-5)$$

$$\dot{m}_a + \text{div}(m_a \mathbf{v}_a) = 0 \quad (6-6)$$

where  $m_i = \phi S_i \rho_i$  is the mass of fluid per unit volume ( $i = l$  for liquid water,  $v$  for water vapor and  $a$  for dry air);  $\phi$  is the total porosity;  $S_i$  is the degree of saturation;  $\rho_i$  is the density;  $m_{vap}$  is the mass of vaporized water per unit volume;  $m_{hyd}$  is the mass of water that has reacted with cement per unit of volume;  $\mathbf{v}_i$  is the velocity of the fluid.



- 1 : Vapor water **diffusion** / air
- 2 : **Darcian** flow of liquid water and gas
- 3 : Evaporation / condensation
- 4 : Adsorption / desorption

Figure 6-3. Water transfer mechanism

The velocity of each phase is related to the solid skeleton's strain, permeation, diffusion and convection. For simulating drying, it seems reasonable to assume the following hypothesis:

- The effect of the solid skeleton's strain rate on the drying process is negligible and the velocity of the solid skeleton is negligible compared to those of the fluid phases.
- The gas pressure (vapor and dry air) is equal to the atmospheric pressure and is negligible compared to the liquid water and capillary pressures (which equals about -96 MPa at 50 % relative humidity). Thus, the capillary pressure and the liquid water pressure are assumed to be equal ( $p_c = p_l$ ).
- the parameters governing the drying phenomena do not depend on cracking.

By neglecting movement of dry air and effect of hydration on drying, we obtain the following equation:

$$\begin{aligned} \rho_l \left[ \Phi \left( 1 - \frac{\rho_v}{\rho_l} \right) \right] \frac{\partial S_l}{\partial t} & \quad (6-7) \\ & = \text{div} \left[ \frac{\partial p_c}{\partial S_l} \left( K_l \frac{\rho_l}{\mu_l} + D_v h \frac{p_{vs}}{\rho_l} \left( \frac{M_w}{RT} \right)^2 \right) \text{grad}(S_l) \right] \end{aligned}$$

The final form of moisture transport can be written as:

$$\frac{\partial S_l}{\partial t} = \text{div}[D(S_l)\text{grad}(S_l)] \quad (6-8)$$

Where  $D(S_l)$  is the effective diffusivity corresponding to the movement of liquid and vapor water. In this study however it is assumed that liquid water transfer is the dominant moisture transfer mechanism as explained also in Chapter 4 (it was

observed that up to 50% degree of saturation, water permeability is the major transport mechanism). However, it is acknowledged that vapour transfer could also influence moisture transport at high temperature. In order to compute the moisture transport, according to Eq.(6-9) the liquid permeability  $K_l(S_l)$ , and water retention curve  $S_l(p_c)$  are required. These two fundamental inputs are computed using the pore network framework developed in Chapter 2 and Chapter 3. However, in order to account for temperature effect, the results from pore network modelling at an ambient temperature are embedded in Van Genuchten model described in Eq.(6-10), and then the effect of temperature is also accounted for.

Water sorption isotherm as:

$$p_c = a_{mu} \left[ (S_l^{-b_{mu}} - 1)^{1 - \frac{1}{b_{mu}}} \right] \quad (6-9)$$

Parameters affected by temperature directly imposed on sorption isotherm as:

$$a_{mu} = a_{mu0} e^{\frac{T - T_{ref}}{T_{mu} - T_{ref}}} \quad (6-10)$$

where  $T_{mu} = 331.3$ ,  $a_{mu0} = a_{mu}(T_{ref})$ , and  $T_{ref} = 293$ .

The temperature dependent viscosity of the water is also computed as follows:

$$\mu_l = A_\mu 10^{\frac{B_\mu}{T - C_\mu}} \quad (6-11)$$

where  $A_\mu = 2.414 \times 10^{-5}$  Pa.s,  $B_\mu = 247.8$  K and  $C_\mu = 140$  K.

### 6.2.4.3 Mechanical constitutive laws

Considering the study case of the chapter, thermal loading causes expansion whereas the drying contraction. While the basis for these contraction and expansion is a linear correlation with temperature and moisture field via Eq.(6-14) and Eq.(6-15), the stress levels corresponding to these strain fields can be interpreted based on either linear or non-linear stress-strain constitutive laws. In this chapter it is presumed that stress level built in the material is linearly associated with the strain using the classic Hooke's law as:

$$\boldsymbol{\sigma} = (1 - d)\mathbf{D}:\boldsymbol{\epsilon}_{el} \quad (6-12)$$

$$\boldsymbol{\epsilon}_{el} = \boldsymbol{\epsilon}_T - (\boldsymbol{\epsilon}_{th} + \boldsymbol{\epsilon}_{sh} + \boldsymbol{\epsilon}_c) \quad (6-13)$$

where  $\boldsymbol{\sigma}$  is stress tensor,  $\mathbf{D}^{eff}$  is material's stiffness matrix  $\boldsymbol{\epsilon}_T$  total strain, which is the combination of elastic deformation, thermal expansion, drying shrinkage, and creep, respectively denoted as  $\boldsymbol{\epsilon}_{el}$ ,  $\boldsymbol{\epsilon}_{th}$ ,  $\boldsymbol{\epsilon}_{sh}$  and  $\boldsymbol{\epsilon}_c$ , and  $d$  is the damage parameter which is assumed to be a scalar value in this study. Creep is indicated when strain in a solid increases with time while the stress producing the strain is kept constant. In more practical terms, creep is the increased strain or deformation of a structural element under a constant load. Creep behavior can also reduce the stress values in response to strain generated in the structure (stress relaxation).

#### 6.2.4.4 Thermal expansion, drying shrinkage and creep models

The coefficient of thermal expansion is measured using micromechanical modelling and assumed to be constant. The thermal expansion strain is computed as:

$$\dot{\epsilon}_{th} = k_{th}\dot{T} \quad (6-14)$$

The drying shrinkage is calculated using the methodology presented in Chapter 3. The volumetric drying shrinkage is initially computed using multi-mechanism model for cement paste scale in order to estimate the deformation as a function of degree of saturation. Then a realistic meso-structure using randomly shaped aggregates and in accordance with real concrete aggregate size distribution given in [4] is constructed, then the computed shrinkage for cement paste is imposed on the cement present in concrete scale and the deformation of the whole RVE is measured. And finally the measured value from concrete level is reflected in a linear function using shrinkage coefficient then embedded in model as an equation similar to Eq.(6-14) for thermal expansion but here temperature is replaced by degree of saturation, which is computed by the above mentioned methodology.

$$\dot{\epsilon}_{sh} = k_{sh}\dot{S}_l \quad (6-15)$$

With  $\dot{\epsilon}_{sh}$  as shrinkage strain,  $k_{sh}$  as shrinkage coefficient and  $S_l$  water content.

As demonstrated in Chapter 5 the drying shrinkage strain cannot be accommodated solely with elastic stress response as the stress levels would be unrealistically high and it would overestimate the damage. Therefore, creep seems to be an inseparable phenomena from shrinkage. However, creep here is due to internal forces (drying shrinkage and thermal expansion) not due to

external mechanical loading as opposed to the classical definition of drying creep.

Under stress, a concrete specimen deforms with time more than an identical load free companion specimen. The difference is the mechanical strain  $\varepsilon_\sigma$  which consists of elastic strain  $\varepsilon_e$  and creep strain  $\varepsilon_c$  defined as:

$$\varepsilon_\sigma = \varepsilon_e + \varepsilon_c \quad (6-16)$$

where  $\varepsilon_e = \frac{\sigma}{E}$  with  $\sigma$  as stress and  $E$  as elastic modulus.

The creep here is treated as a modification in mechanical properties of concrete in order to obtain more realistic results for damage prediction in the abovementioned THM simulation. This is done via introduction of creep coefficient and updating the tension threshold of the material in damage model. The creep coefficient is defined as the ratio of the creep strain to the elastic strain of concrete at an age of 28 days (reference elastic deformation) under the same stress.

$$\varphi_c = \frac{\varepsilon_c}{\varepsilon_e} \quad (6-17)$$

The creep coefficient includes basic and drying creep:

$$\varphi_c = \varphi_{bc} + \varphi_{dc} \quad (6-18)$$

Where  $\varphi_{bc}$  is basic creep and  $\varphi_{dc}$  is drying creep. It is worth mentioning that basic creep alters in higher temperature and it can increase by a factor of 2.5 by increasing the temperature up to 80 °C. Therefore, given the case study of this chapter the basic creep coefficient is revised for higher temperatures as:

$$\varphi_{bc} = \varphi_{bc0} * \varphi_{th} \quad (6-19)$$

Where  $\varphi_{bc0}$  is specific basic creep and  $\varphi_{th}$  is thermal creep coefficient and it is assumed to be equal 2 adapted from [160, 161]. Specific basic creep is defined as basic creep at room temperature. Specific basic creep is measured from experimental data reported in [4, 162] as 0.3 and drying creep is estimated based on fib 2010 code, which would be equal to 0.7. As mentioned earlier, the main implication of creep coefficient here is in estimation of the damage.

#### 6.2.4.5 Damage model

Mazars damage model [163, 164] is hired here in order to estimate damage during THM loading. The evolution of damage is based on the amount of extension that the material is experiencing during the mechanical loading. An equivalent strain is defined as:

$$\tilde{\varepsilon} = \sqrt{\sum_{i=1}^3 (\langle \varepsilon_i \rangle_+)^2} \quad (6-20)$$

Where  $\langle \cdot \rangle_+$  is the Macauley bracket and  $\varepsilon_i$  are the principal strains. The loading function of damage is

$$f(\tilde{\varepsilon}, k) = \tilde{\varepsilon} - k \quad (6-21)$$

where  $k$  is the threshold of damage growth. Initially, its value is  $k_0$ , which can be related to the peak stress  $f_t$  of the material in uniaxial tension:

$$k_0 = \frac{f_t}{E_0} \quad (6-22)$$

In the course of loading  $k$  assumes the maximum value of the equivalent strain ever reached during the loading history.

*if*  $f(\tilde{\varepsilon}, k) = 0$  *and*  $\dot{f}(\tilde{\varepsilon}, k) = 0$ , *then*

$$\begin{cases} d = h(k) \\ k = \tilde{\varepsilon} \end{cases} \text{ with } \dot{d} \geq 0, \text{ else } \begin{cases} \dot{d} = 0 \\ \dot{k} = 0 \end{cases}$$

The function  $h(k)$  is detailed as follows: in order to capture the differences of mechanical responses of the material in tension and in compression, the damage variable is split into two parts:

$$d = \alpha_t d_t + \alpha_c d_c \quad (6-23)$$

where  $d_t$  and  $d_c$  are the damage variables in tension and compression, respectively. They are combined with the weighting coefficients  $\alpha_t$  and  $\alpha_c$ , defined as functions of the principal values of the strains  $\varepsilon_{ij}^t$  and  $\varepsilon_{ij}^c$  due to positive and negative stresses:

$$\varepsilon_{ij}^t = (1 - d) C_{ijkl}^{-1} \sigma_{kl}^t, \quad \varepsilon_{ij}^c = (1 - d) C_{ijkl}^{-1} \sigma_{kl}^c \quad (6-24)$$

$$\alpha_t = \sum_{i=1}^3 \left( \frac{\langle \varepsilon_i^t \rangle \langle \varepsilon_i \rangle}{\bar{\varepsilon}^2} \right)^\beta, \quad \alpha_c = \sum_{i=1}^3 \left( \frac{\langle \varepsilon_i^c \rangle \langle \varepsilon_i \rangle}{\bar{\varepsilon}^2} \right)^\beta \quad (6-25)$$

The evolution of damage is provided in an integrated form, as a function of the variable  $k$ :

$$d_t = 1 - \frac{k_0(1 - A_t)}{k} - \frac{A_t}{\exp[\beta_t(k - k_0)]} \quad (6-26)$$

$$d_c = 1 - \frac{k_0(1 - A_c)}{k} - \frac{A_c}{\exp[\beta_c(k - k_0)]} \quad (6-27)$$

The damage parameters here are assumed to be in accordance with a semi-brittle behaviour of the material. Hence, the values are as [163]:

$$A_c = 1.4, \quad \beta_c = 1900$$

$$A_t = 0.85, \quad \beta_t = 11000$$

With  $\beta=1$  Eq.(6-25). It is worth mentioning that in order to account for creep behaviour of the material and its implication on the damage, the  $f_t$  term in  $k_0$  is revised as:

$$\hat{f}_t = f_t * \frac{E_c}{E_{eff}} = f_t * (1 + \varphi_c) \quad (6-28)$$

Herewith the creep behaviour of material is indirectly incorporated in the final damage calculation. An alternative could also be done by updating the elastic

modulus to effective E modulus according to fib code 2010 [165] as  $E_{eff} = \frac{E_c}{(1+\varphi_c)}$ . This however would change the stress values that is why it is not used here.

### 6.2.5 Properties

Prior to THM calculation, material related parameters are computed using techniques developed in this thesis. This section explores the acquisition these properties.

In order to acquire thermo-hydro-mechanical properties of SC in a multiscale framework a stepwise analyses is conducted (Figure 6-4):

- I. Modelling the microstructure of SC at its hardened cement paste level from its chemical composition and curing condition - initial input.
- II. Constructing a network corresponding to the microstructure to estimate hydraulic and transport properties: water retention curve and intrinsic and relative water permeability – Chapter 2 and Chapter 4.
- III. Computing thermo-mechanical properties using micromechanical method at cement paste and concrete level, i.e., elastic modulus, Poisson's ratio, coefficient of thermal expansion (CTE) – Chapter 5.
- IV. Modelling the drying shrinkage strain as a function of degree of saturation using multi-mechanism shrinkage model at cement paste level – Chapter 3.
- V. Upscaling the drying shrinkage from cement paste level to concrete level using numerical homogenization and simulated meso-structure at concrete level – Chapter 3 and Chapter 5.

In addition to the properties captured in abovementioned steps, there are few other experimentally measured [4, 71, 162] values that are also needed for a fully coupled thermo-hydro-mechanical modelling, including damage. The estimated parameters along with experimentally measured parameters are reported in

Table 6-4. The predicted water retention curve and unsaturated water permeability are presented in Figure 6-5. It is worth mentioning that for unsaturated water permeability as discussed in Chapter 3 the pore network modelling is more accurate than Van Genuchten model, hence, the results from pore network modelling are taken as the reference values into account (red curve).

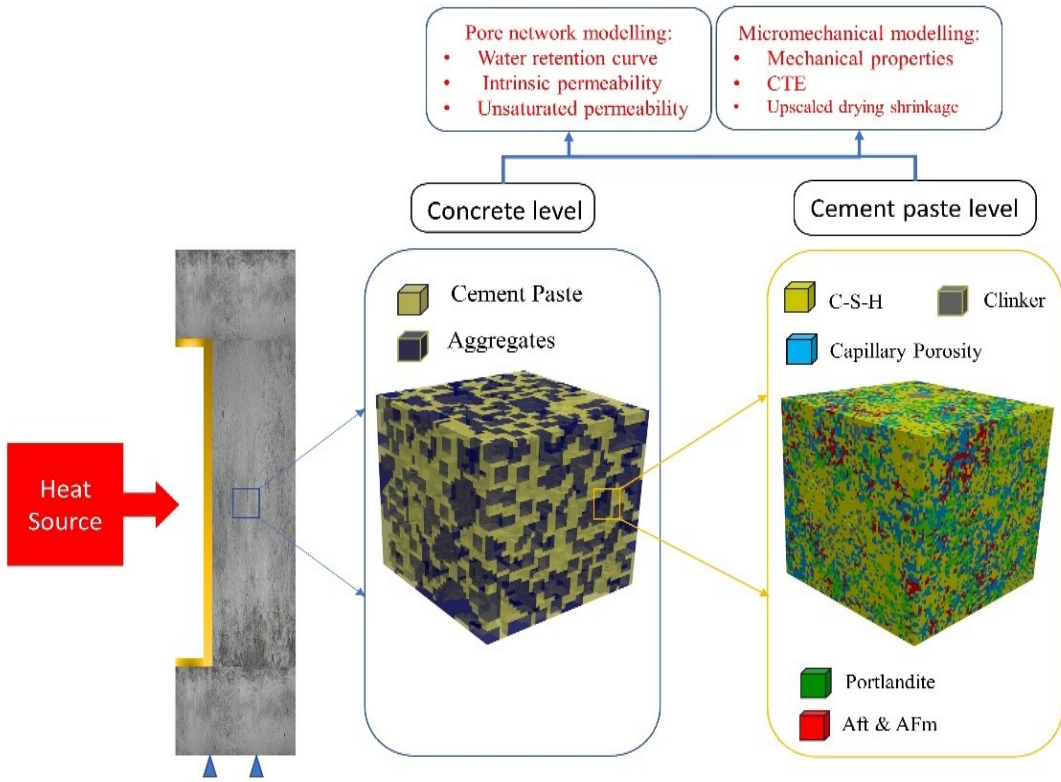


Figure 6-4. Large scale THM analysis with data driven from multiscale analysis modelling framework

Table 6-4. Material parameters

Material Parameters (SCC)	
Thermal	
Convective heat transfer coefficient (W/(m·°C))	5.6 - Empirical
Density (kg/m <sup>3</sup> )	2390 - Experiment
Thermal conduction (W/(m·°C))	1.89 - Experiment
Heat capacity (kJ/(kg·°C))	2390 - Experiment
Density of water (kg/m <sup>3</sup> )	1000 - Constant
Hydraulic	
Permeability (m <sup>2</sup> )	$5.45 \times 10^{-21}$ - Pore network modelling
Porosity at concrete level (-)	0.15
Water retention curve	See Figure 6-5
Mechanical	
E modulus (GPa)	35 - Micromechanical modelling – (36 = experiment)
Poisson ratio (-)	0.26 - Micromechanical modelling
Tensile strength (MPa)	4.4 - Experiment
Coefficient of thermal expansion (1/°C)	$8.5 \times 10^{-6}/^{\circ}\text{C}$ - Micromechanical modelling
Compressive strength (MPa)	45.2 - Experiment
Shrinkage Coefficient	$3129 \times 10^{-6} (\text{m}^3/\text{m}^3)$ - Pore network – multi mechanism model
Creep Coefficients	$\varphi_{bc} = 0.3, \varphi_{dc} = 0.7, \varphi_{th} = 2$ - Experiment & fib code
Damage parameters for Mazars model	$A_c = 1.4, \beta_c = 1900$ $A_t = 0.85, \beta_t = 11000$

Mechanical loading 1	Self-weight loading
Mechanical loading 2	Drying shrinkage strain
Mechanical loading 3	Thermal expansion
Mechanical (carbon steel canister) [4]	
E modulus (GPa)	210
Poisson ratio (-)	0.3
Coefficient of thermal expansion (1/°C)	12 x 10 <sup>-6</sup> /°C

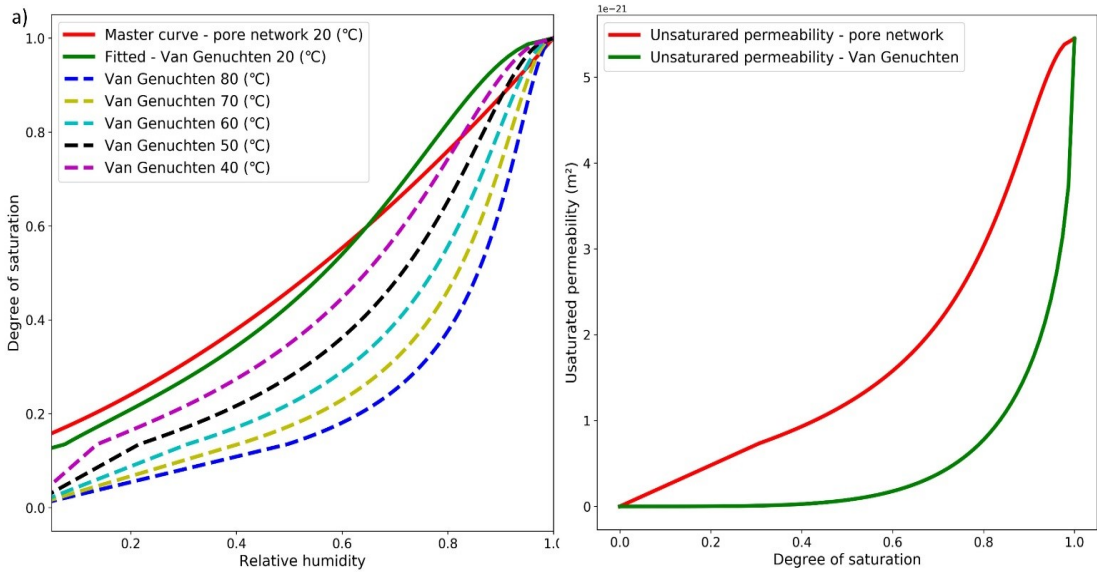


Figure 6-5. Water retention curve at different temperatures (a), unsaturated water permeability (b).

### 6.3 Results and discussion

In the simulations, the evolution of the structure for a period of 90 days under thermal loading is studied. This is corresponding to experimental observation of major cracking, which has happened for thermal loading of 77 days [155, 166, 167]. As a matter of fact the first cracks appeared after 6 days of thermal loading [155]. The analysis is carried out in two steps: (i) only thermal and drying shrinkage are explored, and (ii) thermal, drying shrinkage, creep and damage are explored.

#### 6.3.1 Thermal loading and drying shrinkage – temperature field

Temperature field over the course of 90 days of simulation is reported. It is apparent that after roughly 45 days the temperature variation becomes slower and temperature field stabilizes. The temperature rises due to thermal load on the

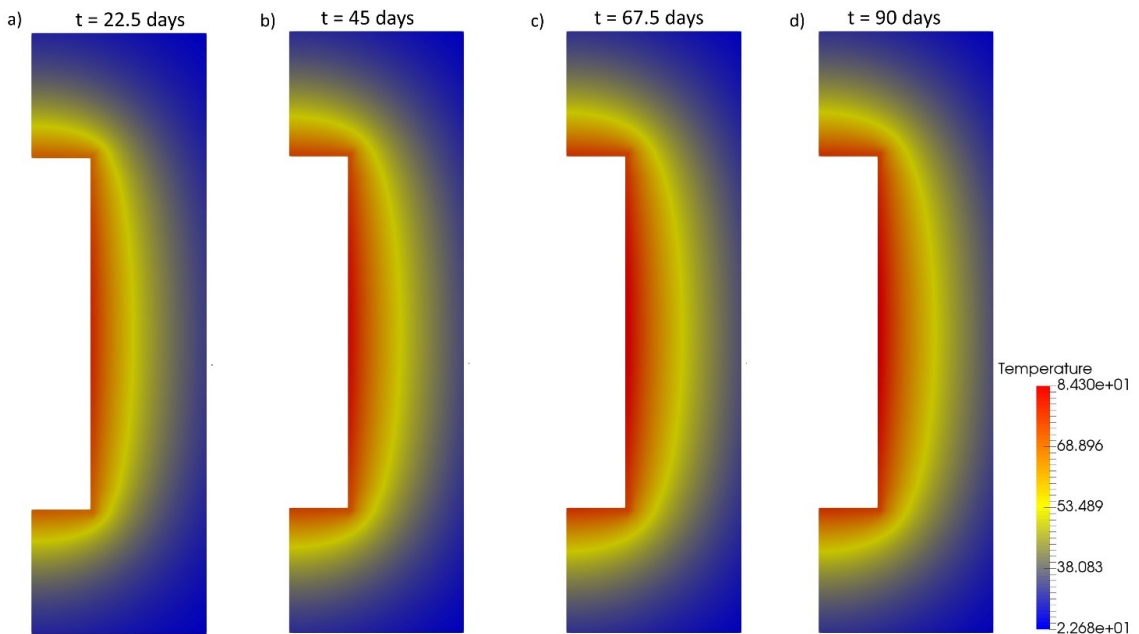


Figure 6-6. Temperature field evolution in 90 days of thermal loading at four different stages. Captured each 22.5 days.

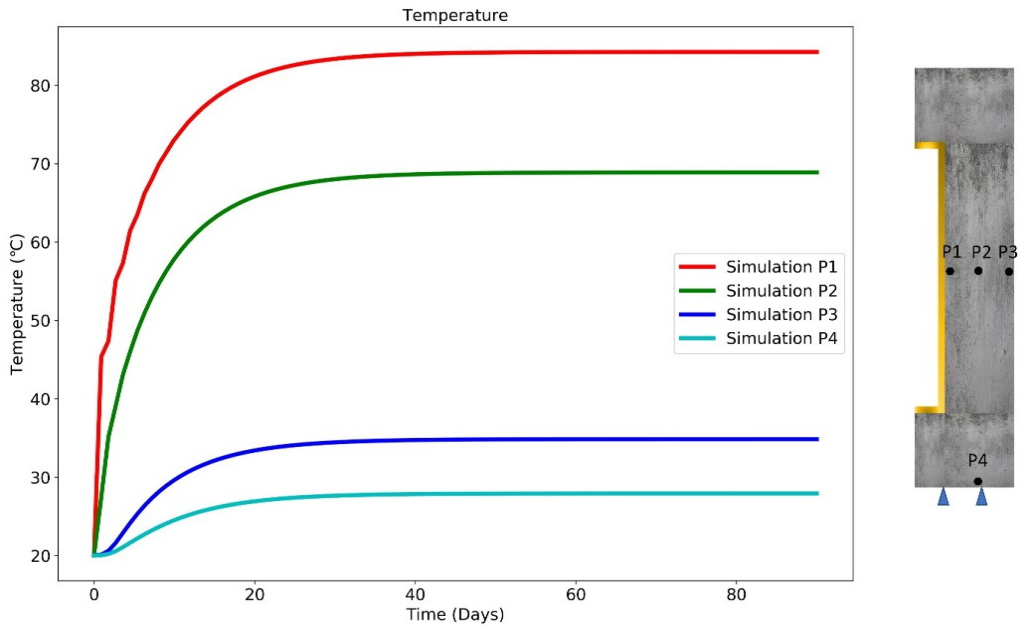


Figure 6-7. Evolution of temperature at investigation points

metallic overpack where the temperature increases exponentially (Figure 6-7) and consequently heat transfers to the buffer, which due to much bigger volume and higher heat capacity 2390 vs 502 (kJ/(kg·°C)) damps down the heat transfer and keeps the temperature outside of the buffer as low as 34 °C on the outer side and 23 °C on the upper and lower sides P4 (Figure 6-6 and Figure 6-7). While, the temperature between overpack and the buffer goes up to 84 °C. Figure 6-7 also shows that the temperature at the core of the structure would remain below 70 °C (P2).

### 6.3.2 Thermal loading and drying shrinkage – moisture field

The moisture field here is modelled assuming the liquid water transport as the main mechanism and results are illustrated for each 22.5 days in Figure 6-8. It is

apparent that drying front is formed on the outer shell (right side) where the water can escape. The concrete is weakly permeable therefore the drying would happen very slowly. This is also evident given the fact that the drying front would not reach anywhere deeper than 5 cm in the core of the structure in 90 days of thermal loading. Expectedly, as time goes by the drying front would

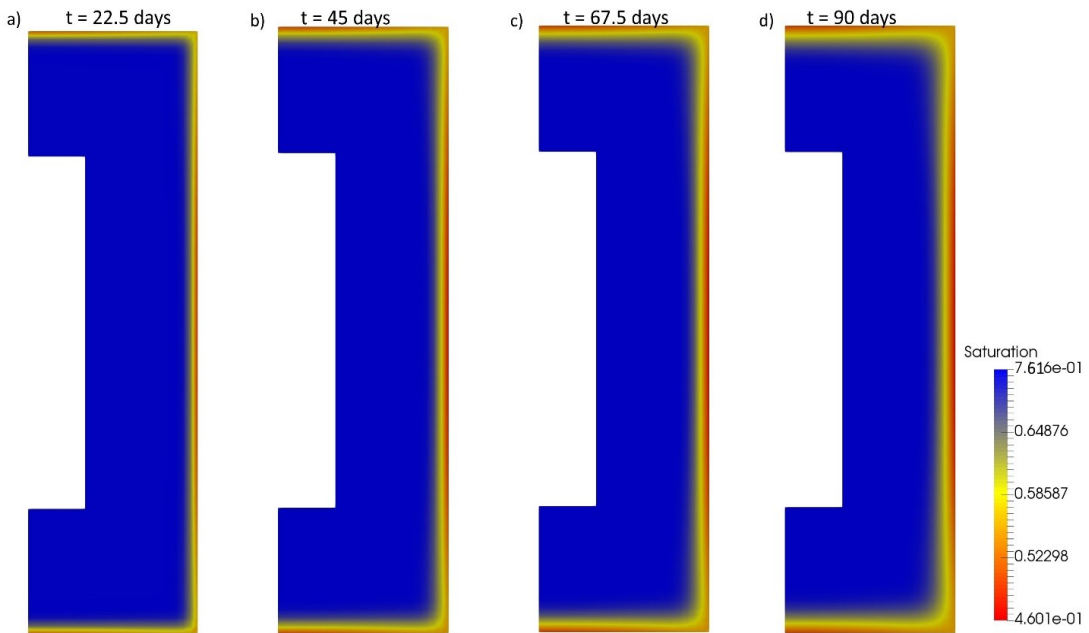


Figure 6-8. Moisture field evolution in 90 days of thermal loading at four different stages. Captured each 22.5 days.

move towards the center of the structure where the thermal loading is imposed. The moisture field does not change fast but due to the fact that it is accompanied with high stress values it is an important phenomenon that should be taken into account.

Figure 6-9 shows the evolution of saturation degree for investigation points where the saturation for P1 and P2 remains always higher than P3 and P4 because water cannot escape the system while P3 and P4 are located on the boundary where the moisture exchange happens. Expectedly, since the P3 is the closest point to the heat source on the boundary, the saturation degree drops to 0.46 saturation while P4 remains above 0.5 degree of saturation. Note that one should expect some drop in the degree of saturation at the inner radius due to a very high temperature ( $84^{\circ}\text{C}$ ) and should propagate in the outwardly direction depending on the moisture transfer rate. However, moisture transfer due to vapour flow has been ignored in this study.

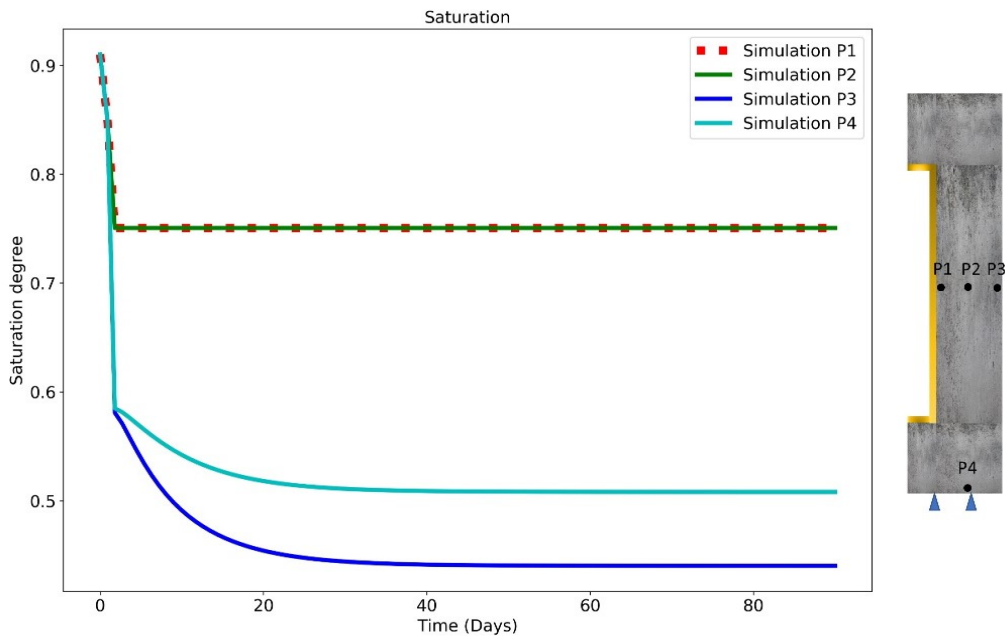


Figure 6-9. Evolution of saturation for investigation points

### 6.3.3 Thermal loading and drying shrinkage – elastic behaviour

The stress distribution in the SC is illustrated in Figure 6-10 and Figure 6-12 for a period of 90 days of thermal loading and linear elastic behavior assumption for materials behavior. The stress distribution here is the result of coexistence of moisture field as in Figure 6-8 and temperature field as in Figure 6-6. This results in very high tensile stresses up to 22.8 and 21.8 MPa for axial and tangential stresses respectively on the outer side and compressive stress on the internal side up to 16.9 and 14.7 MPa for axial and tangential stresses, respectively. Clearly, the concrete can stand the resultant compressive stress of 16 MPa as it is lower than its compressive strength (45 MPa) but this does not hold valid for the tensile

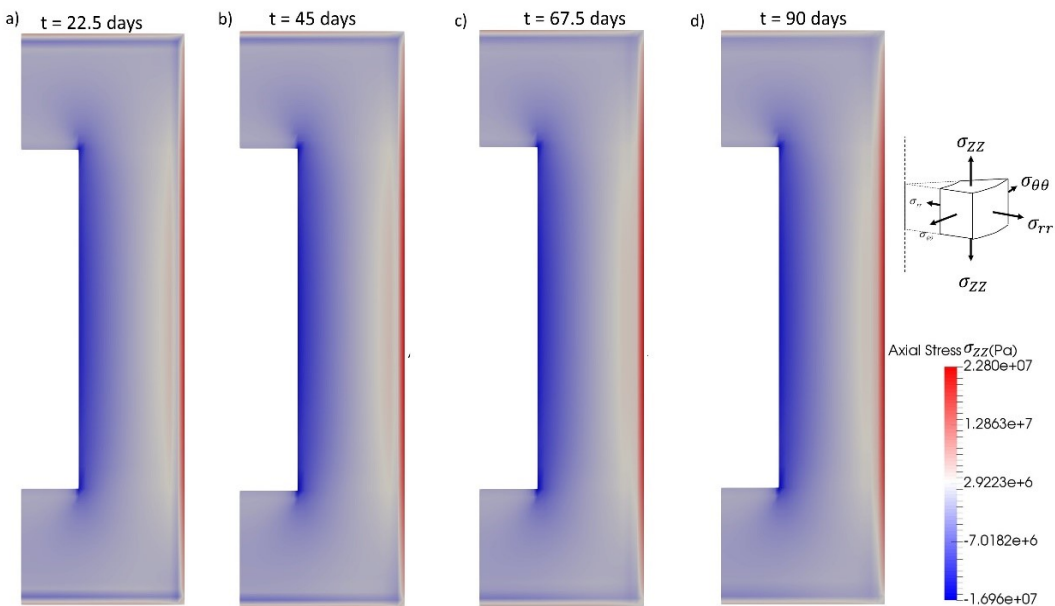


Figure 6-10. Axial stress field evolution in 90 days of thermal loading at four different stages. Captured each 22.5 days.

stress values. The tensile stress value on the external side of SC is as high as 5 times of its tensile strength (4.4 MPa) assuming a linear stress-strain correlation.

Corresponding to these high stresses, the damage evolution in the structure is presented in Figure 6-11. However, note that this analysis does not take into account creep, which could considerably relax the stresses [12, 146].

Given the stress level on the external side of SC, damage appears at relatively early ages (5 days) and it expands further by the time where the damage at point P2 the core of the structure raises up to 0.75 whereas at location P1, which only goes through compression remains intact (Figure 6-13). Expectedly, the predicted damage is overestimated if a linear elastic behavior constitutive law is used for such study case, i.e., thermal loading and drying shrinkage. The damage cannot be this prominent as such amount of damage means that the structure would collapse, which is not the case from experimental observation. Therefore, the creep coefficient is introduced in the damage model to revise the estimated damage values.

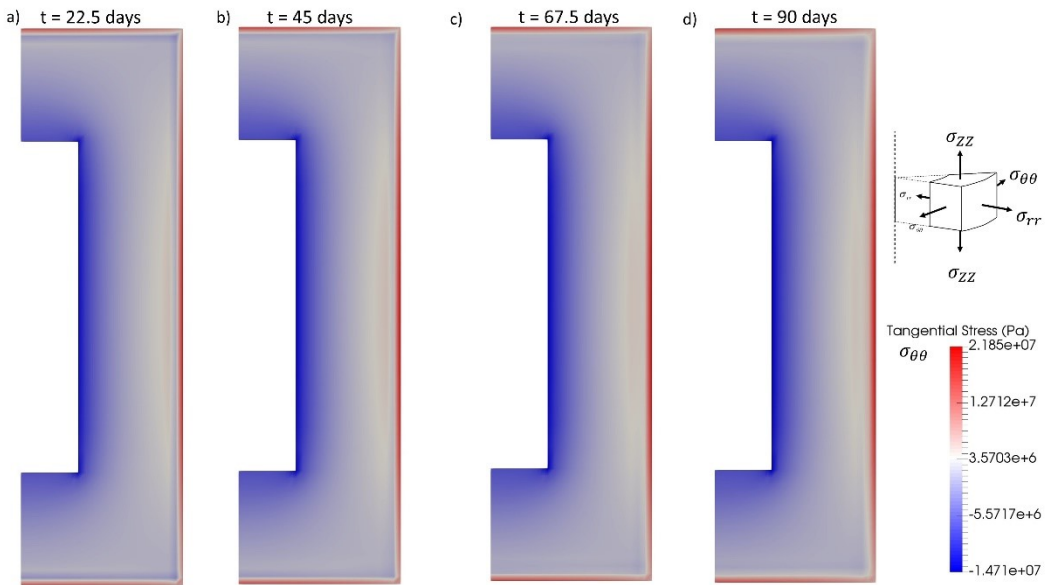


Figure 6-12. Tangential stress field evolution in 90 days of thermal loading at four different stages. Captured each 22.5 days.

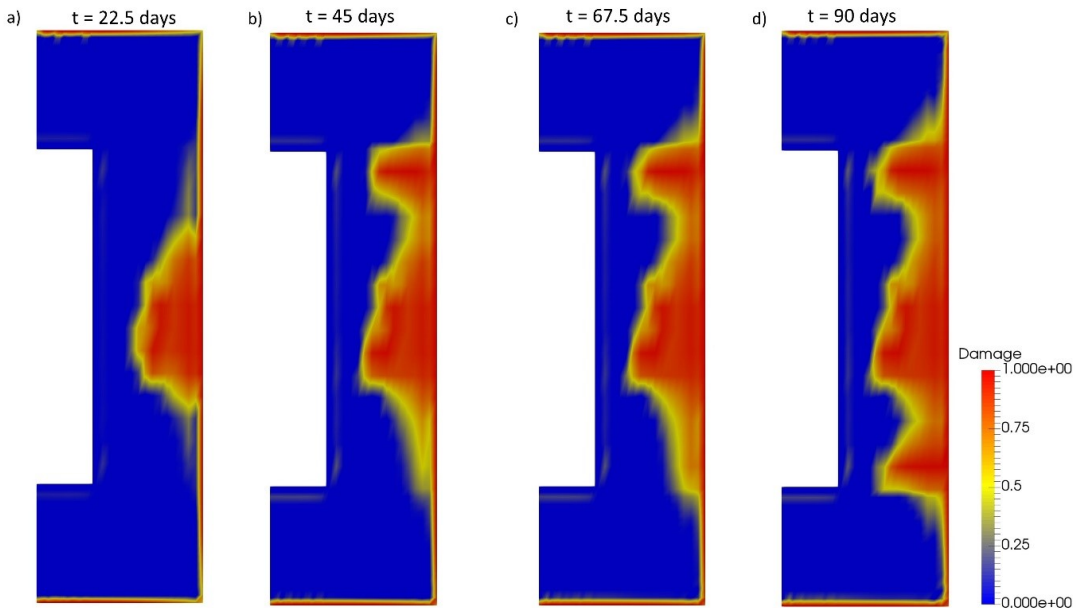


Figure 6-11. Damage evolution in the structure during the thermal loading. Pure elastic behavior.

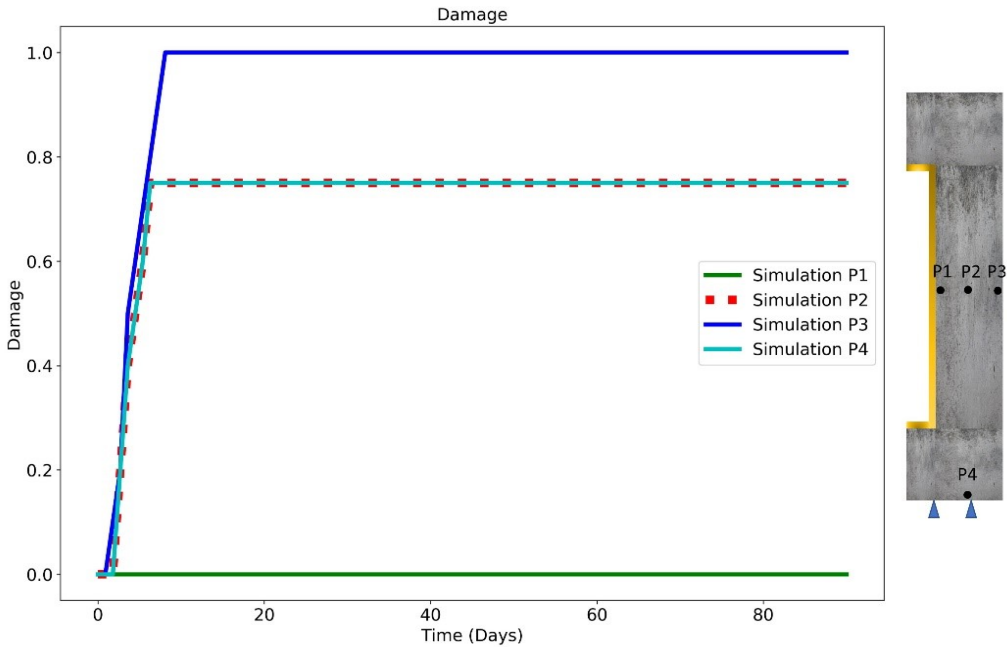


Figure 6-13. Evolution of damage at investigation points (pure elastic behavior)

### 6.3.4 Thermal loading and drying shrinkage, including creep and damage

As described earlier, creep and microcracking are coupled with drying shrinkage at micro and meso scale (chapter 5). It was also shown in the previous section that at structure scale without consideration of creep the damage would be overestimated. In this regard, the creep and relaxation of the stress is accounted for by means of creep coefficient in order to investigate the likelihood of damage in the SC structure in a more realistic way.

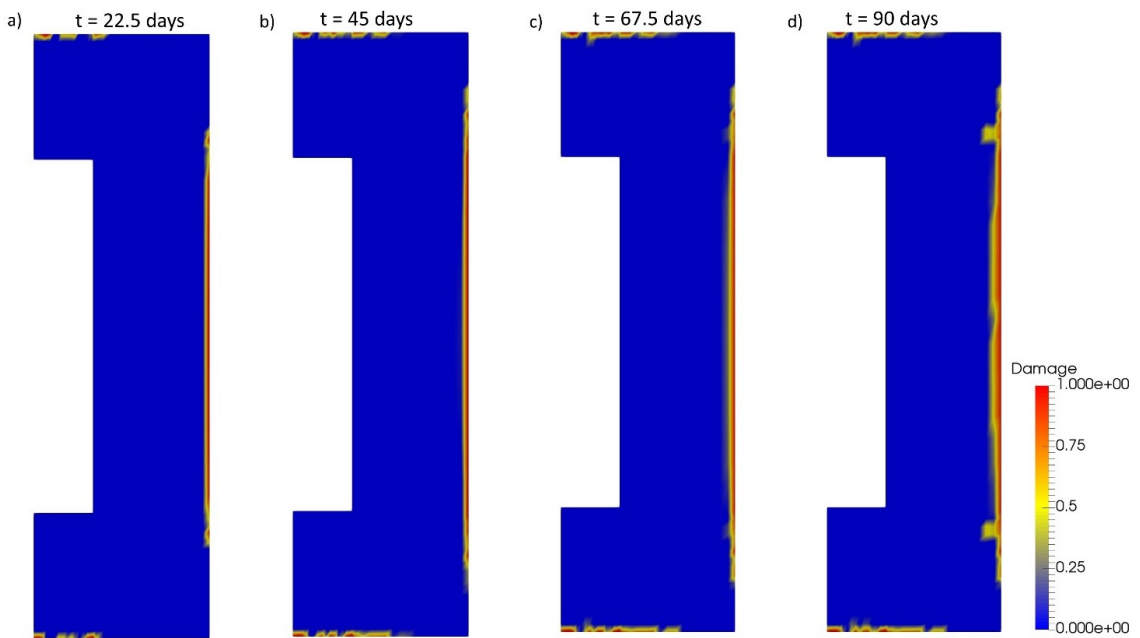


Figure 6-14. Estimated damage considering creep behavior at different time steps.

The indirect implementation of creep in final damage is done by assuming pure linear elastic stress-strain correlation as in Figure 6-10 and then revising the tensile strength value by introduction of total creep coefficient as explained in section 6.2.4.

It is worth noticing that even with basic, thermal and drying creep taken into account there is some damage expected to the structure. The damage is mostly estimated locally at the external surface of the SC where the drying happens and it only evolves with time. In terms of observed damage in investigation points, only P3 and P4, which are on external boundary experience damage and it only reaches 0.32 for P4. The damage estimation here is in agreement with the ones of experimentally observed cracking on the outer side of HST2 [71, 155]. This shows that predicted values using the developed framework not only are valid and applicable on the micro and meso scale but also at structure level they can provide reliable results.

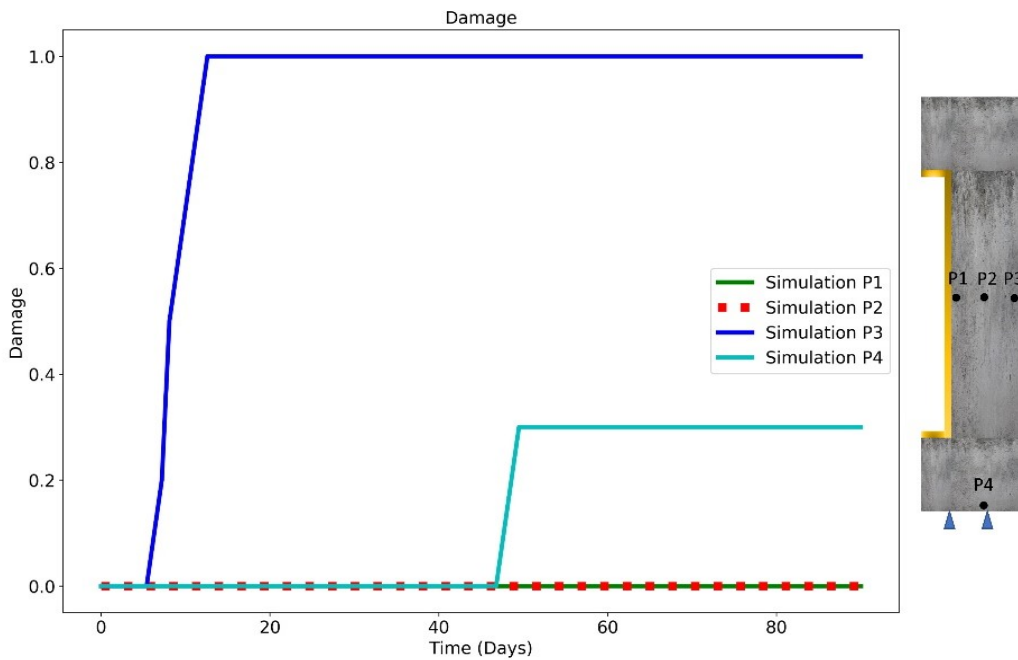


Figure 6-15. Evolution of damage at investigation points (creep included behavior).

A qualitative comparison of predicted damage here and cracking observed during HST2 is illustrated in Figure 6-16 where two investigation points are compared against our predictions. The investigation of crack formation and on the surface of Supercontainer (Figure 6-16) shows formation of crack at early age of thermal loading and its progress throughout the loading. The Figure 6-16 shows a sample which has been extracted from the core of the structure and it shows that cracks are deep. On this sample a 38 cm deep crack was captured which correspond to a possible damage in range of what is predicted Figure 6-11 and Figure 6-14 which are the two pessimistic and optimistic case scenarios respectively.

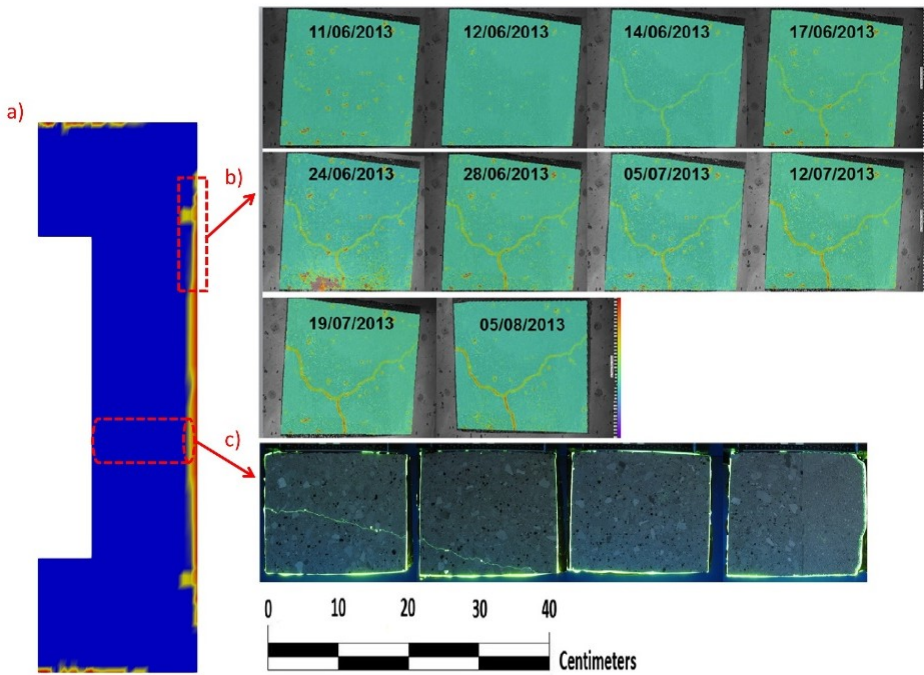


Figure 6-16. Evolution of cracks at two experimental investigation points adapted from [155].

Given the observed results of previous sections and the fact the damage is expected due to the thermal loading and drying, it is worth investigating which one of the two i.e., thermal loading or drying plays a more detrimental role in the observed damage.

### **6.3.5 Thermal stresses vs drying shrinkage stresses – elastic interpolation**

In order to quantify the influence of each phenomenon on the performance of SC structure and their consequential induced stresses at the end of period of thermal loading of 90 days, the drying shrinkage and thermal loading are decoupled into two separate case-studies where only one of them independently occurs. Therefore, the study-cases are: (i) thermal loading without drying effect (stress induced solely by thermal field Figure 6-6 (d) ), and (ii) drying shrinkage without thermal loading (stress induced by moisture field Figure 6-8 (d))

The thermal loading as elaborated earlier causes a temperature gradient within the structure and expansion on the internal side causes a tensile stress on the external side. The distribution of stress just like the temperature distribution is wide and it is dispersed throughout the cross section (Figure 6-17 (a)) while the opposite is true for pure drying shrinkage problem because concrete is weakly permeable and drying usually happens non-uniformly and so its resultant stress distribution. This can be clearly observed in Figure xx where stress induced due to pure drying shrinkage is concentrated on the drying front (Figure 6-17 (b)).

Because of nature of the simulation (axisymmetric) and due to sensitivity of the concrete to tensile stress the axial stress is reported here. Quantitatively speaking, the compressive stress values due to thermal expansion are much higher than the compressive stress due to drying shrinkage, whereas this is not the case for tensile stress and as a matter of fact the opposite contrast exist. The tensile stress due to drying shrinkage in our case study could go as high 15 MPa while in case of thermal expansion the maximum value would be less than half at 7 MPa but it affects a much bigger area compared to the drying shrinkage. Therefore, one can speculate that the drying shrinkage can initiate the damage

because it accompanies locally higher values of stress and thermal loading (in the sense of thermal expansion) would help propagating the damage. This trend is also visible in Figure 6-14 where the damage appears at the drying front and slowly propagates further perpendicular to the drying frontier as seen in Figure 6-14 (d).

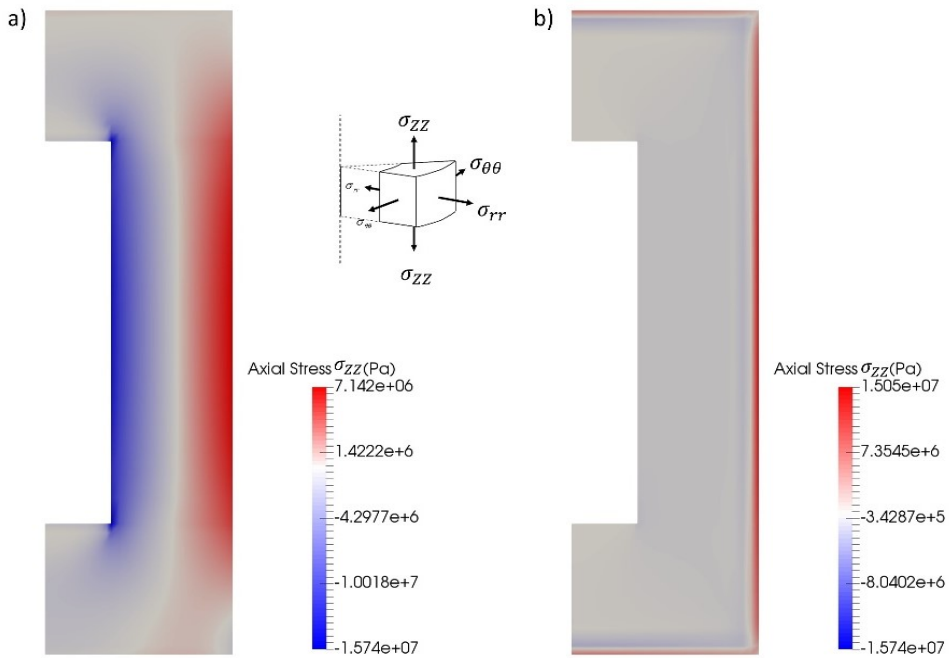


Figure 6-17. Stress field induced due to decoupled temperature gradient (a) and moisture gradient (b).

## 6.4 Conclusions

In this chapter a fully coupled THM analysis of HST2 is carried out using inputs from the multiscale modelling framework developed in this study. The results

show a good agreement with experimental observations both in estimated material parameters (e.g., E modulus, CTE

Table 6-4) and multiphysical phenomena (e.g. drying shrinkage and possible damage), which confirms the capability of the developed methodology. The methodology can successfully extract data from lower scales and upscale them up to structure level simulation.

Regarding the case study of this chapter, the SC structure, thermal expansion and drying shrinkage are the two main phenomena playing a prominent role in the performance of the structure and also its experimentally and numerically observed damage [154, 155, 167]. It was observed that drying shrinkage could cause a locally high stress and thermal expansion a dispersed stress distribution throughout the structure and combination of the two causes damage and cracking, which was observed during HST2.

There are many possible parameter combinations in different categories i.e., material's design, structure design and the choice of the nuclear waste, that can be adapted in order to assure the integrity of the structure. But if the structure and the material designs remain intact there are three possible options for the nuclear waste that impose different thermal loading on the structure as discussed in detail in [4]. As demonstrated here and experimentally observed, the 300 W/m thermal loading and given the boundary condition of the structure can lead to damage in the structure, therefore the lowest possible heat emitting waste would be 240 W/m for 70 years old nuclear waste [4], which would increase the temperature of overpack up to 74 °C, which would decrease the thermal stress. On the other hand, drying shrinkage would still cause locally high stress values on the external surface, therefore the boundary condition should not allow the drying to proceed to degree of saturations lower than 60%. This is possible if the

surrounding relative humidity is as high as 90%. If these two contributing factors (temperature and drying extent) are moderately controlled and damped down, their progressive effect would also decrease significantly, and thus the cracking and damage would be prevented.

One simple design enhancement is also to keep the external mold after casting, and cure the structure before the thermal loading which would control the drying. This will result in stress values reported in Figure 6-17 (a). If interpreted linearly, the damage and cracking is still possible, but since the material is highly saturated its thermal creep would be also higher and therefore the stress values would be relaxed significantly. This can only be concluded confidently if thermal creep at high saturation degrees is measured.

Finally, creep behavior of the material specially drying creep and thermal creep are not measured and only interpolated via empirical models which can introduce uncertainties to the final estimations. Therefore, it is worth further investigating the creep behavior of the material and update the calculations with experimentally measured values.

## **6.5 Acknowledgements**

The work presented in this chapter has been conducted during my research Visit at Prof. Dr. Farid Benboudjema's lab (LMT Ecole normale supérieure Paris-Saclay) and under his direct supervision. His help and persistent supervision is greatly appreciated and acknowledged. This work has been partially supported by the ENEN+ project that has received funding from the EURATOM research and training Work Programme 2016 – 2017 – 1 #755576.



## 7 Conclusions and future perspectives

---

### 7.1 General conclusions

# Chapter 7

Upon conducting this study on multiscale modelling of THM behavior of concrete and development of the elaborated framework in this thesis, conclusions are drawn and future perspectives are discussed in this chapter.

This thesis contributes to a better understanding of the multiscale THM behavior of concrete from a numerical point of view. A unique framework is proposed by means of improving some of the existing numerical modelling tools coupled with multiscale hierarchical modelling techniques. This framework is developed incrementally throughout this PhD study and each of its core components are presented as a chapter in this thesis. Conclusions of each core component or Chapter is discussed here.

Chapter 2 shows that provided the microstructure and enough information on pore space of the material is available, pore network modelling can estimate water retention curve with a good accuracy using the hierarchical network arrangement and a relatively straight forward topological arrangement of pore space. This is valid only if the representative pore network is large enough and all the pore classes are included in the simulation. Even though pore size distribution in the range of capillary pores 12 nm to 1  $\mu\text{m}$  are missing, the predictions are largely satisfactory. There is only one geometrical factor that need to be calibrated making the proposed framework largely predictive unlike any existing studies. This study demonstrates that it is indeed possible to start with a mix composition to predict water retention curve, which allows for preliminary assessment of implication of a given mix design.

Chapter 3 proposes a theoretical framework for estimation of drying shrinkage strain of HCP directly from material composition and its microstructure using the input from Chapter 2, an analytical homogenization technique and a multi-mechanism theoretical formulation. This chapter explores active internal forces responsible for drying shrinkage at different scales and range of drying. It is observed that such a model can be far more accurate and predictive compared to mono-mechanism or empirical models. In terms of calibration parameter, only one parameter ( $\beta$ ) related to disjoining pressure is assumed due to a lack of information. The only other calibration parameter is the geometrical factor related to PNM. However, note that these are fitted only once for an arbitrary material, thus making the theoretical framework largely predictive. This study demonstrates that it is indeed possible to start with a mix composition to predict drying shrinkage strain, which allows for preliminary assessment of the implication of mix design.

Chapter 4 demonstrates a more advanced application of pore network modelling by estimating the saturated and unsaturated permeability of hardened cement paste materials. The framework works by imposing two different algorithmic simulation of ‘constant flow’ and ‘invasion algorithm’ on the same network, which is constructed on the basis of microstructure modelling. The results show a good agreement with wide range experimental observation making this methodology a very successful demonstration of pore network modelling. It is also worth mentioning that the retention curve, which is estimated in Chapter 2 is possible to measure (although time consuming and needs composition specific experiments), however, measuring both saturated and unsaturated permeability is very time consuming and especially the unsaturated permeability is hard to directly measure therefore the added value of this work fully justifies the use of pore network modelling.

Chapter 5 investigates the micromechanics of thermo-mechanical behavior of hardened cement paste (HCP). Firstly, this framework is adopted to estimate thermo-mechanical properties of HCP and concrete from their microstructure and secondly and more importantly the stress distribution during the thermo-mechanical evolution is studied and new insights are shared, which has not been reported previously according to author's knowledge. Finally, drying shrinkage process is analyzed at two scales of HCP and concrete and it is observed that in both the cases shrinkage is accompanied with high stress values which means significant cracking if the shrinkage is interpreted as linear elastic process which is not necessarily always the case in reality. Therefore, it can be concluded that the drying shrinkage (both constraint and free shrinkage) is accompanied with creep and microcracking. Additionally the drying shrinkage computed using the framework described in Chapter 3 is numerically homogenized to concrete level and its application is demonstrated in Chapter 6, meaning the drying shrinkage is computed directly from material composition for both cement paste and concrete level.

Chapter 6 is where all the previously developed tools and techniques are centralized in a numerical modelling framework to model THM behavior of a large scale structure for a Belgian nuclear waste disposal concept referred as Supercontainer. This analysis is conducted to firstly demonstrate the applicability of this study on practical engineering problems and secondly to validate the THM model against experimental observation conducted as HST2. Prior to THM analysis following steps are required in order to obtain material necessary properties:

- I. Modelling the microstructure of SC at its hardened cement paste level from its chemical composition and curing condition - initial input.

- II. Constructing a network corresponding to the microstructure to estimate hydraulic and transport properties: water retention curve and intrinsic and relative water permeability – Chapter 2 and Chapter 4.
- III. Computing thermo-mechanical properties using micromechanical method at cement paste and concrete level, i.e., elastic modulus, Poisson's ratio, coefficient of thermal expansion (CTE) – Chapter 5.
- IV. Modelling the drying shrinkage strain as a function of degree of saturation using multi-mechanism shrinkage model at cement paste level – Chapter 3.
- V. Upscaling the drying shrinkage from cement paste level to concrete level using numerical homogenization and simulated meso-structure at concrete level – Chapter 3 and Chapter 5.

This shows that some of the most important properties needed for THM analysis are directly derived from the framework developed in this thesis. Regarding the results of the simulation it was found that coexistence of drying shrinkage and thermal gradient in the structure can lead to damage which explains the observed cracking during the heating phase. Consequently, possible refinements are proposed.

## **7.2 Future perspectives**

Just as any other research, the proposed work can be further advanced to achieve better predictive models. The following perspectives are shared herein.

Microstructure modelling was used as the primary source of information in the developed framework here. Although the microstructure modelling has advanced remarkably in recent decades and these models are well established

and calibrated with OPC-based cementitious materials, they still fall short in keeping up with development of new materials. Therefore, blended cement systems are not well accommodated in the present microstructure modelling tools and if added they can considerably broaden the field of study on multiscale frameworks. Additionally, improvement in the covered scale of simulation can also bring new insights into the pictures. For instance, having information on nano-micro-meso structure would help researcher to draw a well-informed conclusion on each individual phenomena, similar to discussion on drying shrinkage on two different scale of microstructure (HCP) and meso-structure (concrete). Therefore, possibility to include new materials and wider range of hydration RVE size (nano to meso scale) would be great future development, i.e., a multiscale microstructural modeling tool.

One of the integral components of the developed methodology in this study is pore network modelling that provides an efficient numerical framework to solve pore space related problems. While pore network modelling is numerically efficient and it can accelerate computation significantly the reliability of its predictions, depends vastly on the quality of the correspondence between the pore space of the studied medium and the pore network constructed as its representation. The quality of the representation of a given medium on its own depends mainly on the characterization techniques that are utilized. Given the limited resolution or range of pores that can be characterized using established methods such as direct imaging and adsorption techniques one can conclude that the wider the pore size range of the material is the more challenging is the task of pore network modelling to represent such material and this is the case for cementitious material with a very wide pore size range. Therefore, the first and the main challenge to address in field of cementitious materials is to represent such a wide range of pore space and this is where a clear understanding of the pore space is critical.

Therefore, there are two possible trajectories for PNM to advance in the field of cementitious materials (i.e., to construct a more representative network). The first one is with reliance of PNM on multiscale modelling and available understanding from well-established theoretical frameworks such as molecular dynamics and upscaling properties and information, which are needed for construction of a representative network right from the scale where each class of pore exist. e.g., a microstructural modelling, which can hold C-S-H gel porosity as well as capillary porosity within the same hydration model with all the reaction parameters included such as chemical composition, particle packing, and curing condition.

The second possible source of information is the experimental observation. With advancement in measurement techniques (mostly direct imaging techniques e.g., fib SEM) and their characterization resolution, the issue of discrete measurements (where each technique is used for a specific scale) could be resolved. This results in a better understanding of the pore space properties of cementitious materials and simply with more measurement data points a better informed pore network can be constructed where with optimum computational effort favorable accuracy is reachable. This only can be achieved if data science is coupled well with experimental observations and a reliable data-driven methodology is developed. It is also worth noting that the developed pore network model in this work was not validated for adsorption isotherm. Also the pore size distribution resulted from particle packing and hydration model are not compared to experimental observations which can be an added value.

Regarding the micromechanical modelling framework, there are two refinements for future perspectives. First one is the general advancement in the input and studied scale and second one is more relevant to the methodology adopted in this study. Since the input comes directly from microstructure modelling a similar scale range issue and possible future improvement is sought

i.e. a multiscale hydration model. Additionally, as an alternative source of information micromechanical modelling can also benefit from advancement in imaging techniques where information can be collected actively and incorporated in such numerical modelling frameworks. Second possible future refinement is on implementation of non-linear constitutive law and possibly inclusion of damage mechanics on microscale simulations in order to gain more insights on macro-mechanical behavior of cementitious materials. Additionally, a focused study on each mechanism resulting shrinkage can bring new insights for instance, the disjoining pressure parameter that was assumed to be unity could also be obtained from molecular dynamics (MD) simulations[168].

The large scale THM analysis discussed in final chapter that employs all the developments in previous chapters can also be improved by adding following experimental components:

- I. Comprehensive measurements on drying and thermal creep
- II. Measurement on drying shrinkage
- III. Measurements on transport properties

From numerical point of view also following steps can help improving the reliability of the design:

- I. A 3D model including randomly distributed mechanical properties in order to achieve a more realistic distribution of damage propagation and cracking
- II. Validation of crack configuration with large scale experiments
- III. A study on the effect of different damage constitutive laws on the predicted crack patterns
- IV. A sensitivity analysis on impactful parameters, material related parameters and boundary conditions

- V. An attempt to model creep behaviour of the material from the mix composition in a predictive framework similar to this thesis which can later on be utilized as an optimization tool.

## 8 References

1. ONDRAF/NIRAS, *Research, Development and Demonstration (RD&D) Plan for the geological disposal of high-level and/or long-lived radioactive waste including irradiated fuel if considered as waste*. 2012, Belgian Agency for Radioactive Waste and Enriched Fissile Materials.
2. Lin Liu, Xuecheng Wang, Huisu Chen, Chaojun Wand, and Mingzhong Zhang, *Numerical modeling of drying shrinkage deformation of cement-based composites by coupling multiscale structure model with 3D lattice analyses*. Computers and Structures 2017. **178**: p. 88–104.
3. Babaei, S., S.C. Seetharam, U. Muehlich, A. Dizier, G. Steenackers, and B. Craeye, *A multiscale framework to estimate water sorption isotherms for OPC-based materials*. Cement and Concrete Composites, 2020. **105**: p. 103415.
4. Craeye, B., *Early-age thermo-mechanical behaviour of concrete Supercontainers for radwaste disposal*. Ghent University. Faculty of Engineering, 2010.
5. Weetjens, E., *Update of the near field temperature evolution calculations for disposal of UNE-55, MOX-50 and vitrified HLW in a supercontainer - based geological repository*. 2009: SCK•CEN.
6. Gawin, D., F. Pesavento, and B.A. Schrefler, *Hygro-thermo-chemo-mechanical modelling of concrete at early ages and beyond. Part I: hydration and hygro-thermal phenomena*. International Journal for Numerical Methods in Engineering, 2006. **67**(3): p. 299-331.
7. Gawin, D., F. Pesavento, and B.A. Schrefler, *Hygro-thermo-chemo-mechanical modelling of concrete at early ages and beyond. Part II: shrinkage and creep of concrete*. International Journal for Numerical Methods in Engineering, 2006. **67**(3): p. 332-363.
8. Gawin, D., M. Koniorczyk, and F. Pesavento, *Modelling of hydro-thermo-chemo-mechanical phenomena in building materials*. Bulletin of the Polish Academy of Sciences: Technical Sciences, 2013. **61**(No 1): p. 51-63.
9. Buffo-Lacarrière, L., A. Sellier, and B. Kolani, *Application of thermo-hydro-chemo-mechanical model for early age behaviour of concrete to experimental massive reinforced structures with strain-restraining system*. European Journal of Environmental and Civil Engineering, 2014. **18**(7): p. 814-827.
10. Benboudjema, F., F. Meftah, and J.M. Torrenti, *Interaction between drying, shrinkage, creep and cracking phenomena in concrete*. Engineering Structures, 2005. **27**(2): p. 239-250.
11. Benboudjema, F. and J.M. Torrenti, *Early-age behaviour of concrete nuclear containments*. Nuclear Engineering and Design, 2008. **238**(10): p. 2495-2506.
12. Bažant, Z.P. and M. Jirásek, *Creep and Hygrothermal Effects in Concrete Structures*. Springer Netherlands, 2018. **Series Volume 225**.

13. Bažant, Z.P. and S. Baweja, *Justification and refinements of model B3 for concrete creep and shrinkage I. statistics and sensitivity*. Materials and Structures, 1995. **28**(7): p. 415-430.
14. Hailong Ye and A. Radlińska, *A Review and Comparative Study of Existing Shrinkage Prediction Models for Portland and Non-Portland Cementitious Materials*. Advances in Materials Science and Engineering, 2016.
15. Benboudjema, F., F. Meftah, and J.M. Torrenti, *A viscoelastic approach for the assessment of the drying shrinkage behaviour of cementitious materials*. Materials and Structures, 2006. **40**(2): p. 163.
16. Zhang, H., Y. Xu, Y. Gan, Z. Chang, E. Schlangen, and B. Šavija, *Microstructure informed micromechanical modelling of hydrated cement paste: Techniques and challenges*. Construction and Building Materials, 2020. **251**: p. 118983.
17. Mazaheripour, H., R. Faria, G. Ye, E. Schlangen, J. Granja, and M. Azenha, *Microstructure-Based Prediction of the Elastic Behaviour of Hydrating Cement Pastes*. Applied Sciences, 2018. **8**(3).
18. Sherzer, G., P. Gao, E. Schlangen, G. Ye, and E. Gal, *Upscaling Cement Paste Microstructure to Obtain the Fracture, Shear, and Elastic Concrete Mechanical LDPM Parameters*. Materials (Basel), 2017. **10**(3).
19. Kinomura, K. and T. Ishida, *Enhanced hydration model of fly ash in blended cement and application of extensive modeling for continuous hydration to pozzolanic micro-pore structures*. Cement and Concrete Composites, 2020: p. 103733.
20. Liu, C., F. Wang, and M. Zhang, *Modelling of 3D microstructure and effective diffusivity of fly ash blended cement paste*. Cement and Concrete Composites, 2020. **110**: p. 103586.
21. Rezvani, M., T. Proske, and C.-A. Graubner, *Modelling the drying shrinkage of concrete made with limestone-rich cements*. Cement and Concrete Research, 2019. **115**: p. 160-175.
22. Pinson, M., *Inferring Pore Size and Network Structure from Sorption Hysteresis*. 2014.
23. Ivan Vlahinic, Hamlin M. Jennings, José E. Andrade, and J.J. Thomas, *A novel and general form of effective stress in a partially saturated porous material: The influence of microstructure*. Mechanics of Materials, 2011. **43**: p. 25-35.
24. Vlahinić Ivan, Jennings Hamlin M., and Thomas Jeffrey J., *A constitutive model for drying of a partially saturated porous material*. Mechanics of Materials, 2009. **41**(3): p. 319-328.
25. Zdeněk P. Bažant, Anders Boe Hauggaard, Sandeep Baweja, and F.-J. Ulm, *Microprestress-Solidification Theory for Concrete Creep. I: Aging and Drying Effects*. Journal of Engineering Mechanics, 1997. **123**(11).
26. Tanabe T., Sakata K., Mihashi H., and Maekawa K., *Creep, Shrinkage and Durability Mechanics of Concrete and Concrete Structures*. (Japan, CRC 2009), 2009. **Vol 1**(1st Edn).
27. Baroghel-Bouny V., *Water vapour sorption experiments on hardened cementitious materials: Part I: Essential tool for analysis of hygral behaviour and its relation to pore structure*. Cement and Concrete Research, 2007(37): p. 414-437.

28. De Burgh J.M. and Foster S.J., *Influence of temperature on water vapour sorption isotherms and kinetics of hardened cement paste and concrete*. Cement and Concrete Research, 2017. **92**: p. 37-55.
29. Zhang Z., Thierry M., and Baroghel-Bouny V., *An equation of drying kinetics for cementitious materials*. Drying Technology, 2017. **36**(12): p. 1-14.
30. Wu M., Johannesson B., and Geiker M., *A study of the water vapor sorption isotherms of hardened cement pastes: Possible pore structure changes at low relative humidity and the impact of temperature on isotherms*. Cement and Concrete Research, 2014. **56**: p. 97-105.
31. Reatto A., *Validity of the Centrifuge Method for Determining the Water Retention Properties of Tropical Soils*. 2008. **72**(6): p. 1547-1553.
32. Reis R.M., *Determination of the Soil-Water Retention Curve and the Hydraulic Conductivity Function Using a Small Centrifuge*. Geotechnical Testing Journal, 2011. **34**(5): p. 457-466.
33. Thomas Rougelot, Frédéric Skoczylas, and Nicolas Burlion, *Water desorption and shrinkage in mortars and cement pastes: Experimental study and poromechanical model*. Cement and Concrete Research, 2009. **39**: p. 36–44.
34. James M. de Burgh, Stephen J. Foster, and H.R. Valipour, *Prediction of water vapour sorption isotherms and microstructure of hardened Portland cement pastes*. Cement and Concrete Research, 2016. **81**(134): p. 134-150.
35. Aditya Kumar, Sabrina Ketel, Kirk Vance, Tandre Oey, Narayanan Neithalath, and G. Sant, *Water Vapor Sorption in Cementitious Materials Measurement, Modeling and Interpretation*. Transport in Porous Media, 2014. **103**(1): p. 69-98.
36. Matthew B. Pinson, Enrico Masoero, and Hamlin M. Jennings, *Hysteresis from Multiscale Porosity: Modeling Water Sorption and Shrinkage in Cement Paste*. American Physical Society, 2015. **3**.
37. Torben C. Hansen, *Physical structure of hardened cement paste. A classical approach*. Materials and Structures, 1986. **19**,(6): p. 423–436.
38. Enrico Masoero, Gianluca Cusatis, and G.D. Luzio, *C–S–H gel densification: The impact of the nanoscale on self-desiccation and sorption isotherms*. Cement and Concrete Research, 2018. **109**: p. 103-119.
39. Mason G., *A model of adsorption-desorption hysteresis in which hysteresis is primarily developed by the interconnections in a network of pores*. Proceedings of the Royal Society of London, 1983. **390**:: p. 47–72.
40. Islahuddin M. and Janssen H., *Hygric property estimation of porous building materials with multiscale pore structures*. Energy Procedia, 2017. **132**: p. 273-278.
41. Constantinides, G. and F.J. Ulm, *The effect of two types of C-S-H on the elasticity of cement-based materials: Results from nanoindentation and micromechanical modeling*. Cement and Concrete Research, 2004. **34**(1): p. 67-80.
42. Fonseca P.C., Jennings H.M., and Andrade J.E., *A nanoscale numerical model of calcium silicate hydrate*. Mechanics of Materials, 2011. **43**: p. 408–419.
43. Jennings, H.M., *A model for the microstructure of calcium silicate hydrate in cement paste*. Cement and Concrete Research, 2000. **30** (1): p. 101-116.

44. Donev A., Cisse I., Sachs D., Variano E.A., Stillinger F.H., Connely R., Torquato S., and Chaikin P.M., *Improving the density of jammed disordered packings using ellipsoids*. Science, 2004. **303**: p. 990-993.
45. Ulm F.J., Constantinides G., and Heukamp F.H., *Is concrete a poromechanics material? – A multiscale investigation of poroelastic properties*. Mater Struct, 2004. **37**: p. 43-58.
46. Jennings H.M., Thomas J.J., Gevrennov J.S., Constantinides G., and Ulm F.J., *A multi-technique investigation of the nanoporosity of cement paste*. Cem Concr Res, 2007. **37**: p. 329-336
  
47. Thomas J.J. and Jennings H.M., *A colloidal interpretation of chemical aging of the C-S-H gel and its effects on the properties of cement paste*. Cem Concr Res, 2006. **36**: p. 30-38.
48. Jaeger H.M. and Nagel S. R., *Physics of granular state*. Science,, 1992. **255**(5051): p. 1523-1531.
49. Sloane N. J. A., *Kepler's conjecture confirmed*. Nature, 1998. **395**: p. 435-436.
50. Georgios Constantinides, *Invariant Mechanical Properties of Calcium-Silicate-Hydrates (C-S-H) in Cement-Based Materials: Instrumented Nanoindentation and Microporomechanical Modeling*. MASSACHUSETTS INSTITUTE OF TECHNOLOGY, 2006.
51. Thomas J.J., Biernacki J.J., Bullard J.W., Bishnoi Sh., Dolado J.S., Scherer G.W., and Luttge A., *Modeling and simulation of cement hydration kinetics and microstructure development*. Cement and Concrete Research, 2011. **41**(12): p. 1257-1278.
52. Bullard J.W., *VCCTL Version 9.5 User Guide*. NIST, 2014.
53. Van Breugel K., *Simulation of hydration and formation of structure in hardening cement-based materials*. TU Delft, 1991.
54. Ye, G., *Experimental Study and Numerical Simulation of the Development of the Microstructure and Permeability of Cementitious Materials*. Delft University of Technology, 2003.
55. Li, K., *Numerical Determination of Permeability in Unsaturated Cementitious Materials*. Delft University of Technology, 2017.
56. Gostick J., Aghighi M., and Hinebaugh J., *OpenPNM: A Pore Network Modeling Package*. Computing in Science & Engineering, 2016. **18**(4): p. 60-74.
57. Raouf A., *PoreFlow: A Complex Pore-Network Model for Simulation of Reactive Transport in Variably Saturated Porous Media*. Computers & Geosciences, 2013. **61**: p. 160-174.
58. Jennings H.M. and Tennis P.D., *A model for the developing microstructure in Portland cement pastes*. frAmer. Ceram. Soc, 1994. **77**(12): p. 3161-3172.
59. P. Kumar Mehta and Paulo J. M. Monteiro, *Concrete: Microstructure, Properties, and Materials*. McGraw Hill Professional, 2013.
60. David Wilkinson and Jorge F Willemsen, *Invasion percolation: a new form of percolation theory*. Journal of Physics A: Mathematical and General, 1983. **16** p. 3365-3376. .

61. MASON G., *A Model of the Pore Space in a Random Packing of Equal Spheres* Journal of Colloid and Interface Science, 1971. **35**(2): p. 279-287.
62. Arne Hillerborg, *A modified absorption theory*. Cement and Concrete Research, 1985. **15**(5): p. 809-816.
63. Baroghel-Bouny V. and Godin J., *Experimental study on drying shrinkage of ordinary and high-performance cementitious materials*. RILEM Conf Shrinkage, 2001. **3**: p. 13-22.
64. Baroghel-Bouny V., Mainguy M., Lassabatere T., and Coussya O., *Characterization and identification of equilibrium and transfer moisture properties for ordinary and high-performance cementitious materials*. Cement and Concrete Research, 1999. **29**: p. 1225–1238.
65. Ranaivomanana H., Verdier J., Sellier A., and Bourbon X., *Toward a better comprehension and modeling of hysteresis cycles in the water sorption–desorption process for cement based materials*. Cement and Concrete Research 2011. **41**: p. 817-827.
66. Galen Egan, Aditya Kumar, Narayanan Neithalath, and G. Sant, *Re-examining the influence of the inclusion characteristics on the drying shrinkage of cementitious composites*. Construction and Building Materials, 2017. **146**: p. 713-722.
67. Baroghel-Bouny V., Mainguy M., Lassabatere T., and Coussy O., *Characterization and identification of equilibrium and transfer moisture properties for ordinary and high-performance cementitious materials*. Cement and Concrete Research 1999. **29** p. 1225–1238.
68. Hughes A. and Grawoig D., *Statistics: A Foundation for Analysis*. Addison-Wesley Educational Publishers Inc, 1971.
69. Maruyama, I. and P. Lura, *Properties of early-age concrete relevant to cracking in massive concrete*. Cement and Concrete Research, 2019. **123**: p. 105770.
70. Craeye, B., G. De Schutter, H. Van Humbeeck, and A. Van Cotthem, *Early age behaviour of concrete supercontainers for radioactive waste disposal*. Nuclear Engineering and Design, 2009. **239**(1): p. 23-35.
71. Craeye, B., G. De Schutter, W. Wacquier, H. Van Humbeeck, A. Van Cotthem, and L. Areias, *Closure of the concrete supercontainer in hot cell under thermal load*. Nuclear Engineering and Design, 2011. **241**(5): p. 1352-1359.
72. J., B. and Bernier F., *Temperature Criterion Related to Clay Based Backfill Materials in the Framework of a Geological Repository of Heat Producing Radioactive Waste (HLW)*. Proc. ICEM'01, The 8th International conference on Environmental Management, Bruges, Sept.30 - Oct.4, 2001.
73. *ACI-209 (2008), Guide for modeling and calculating shrinkage and creep in hardened concrete*. Farmington Hills, American Concrete Institute: p. 48.
74. *EN-1992-1-1 2008, Eurocode 2—design of concrete structures*. Comite Europeen de Normalisation (CEN). Brussels,: p. 259.
75. Coussy, O., P. Dangla, T. Lassabatère, and V. Baroghel-Bouny, *The equivalent pore pressure and the swelling and shrinkage of cement-based materials*. Materials and Structures, 2004. **37**(1): p. 15-20.
76. Xi, Y. and H.M. Jennings, *Shrinkage of cement paste and concrete modelled by a multiscale effective homogeneous theory*. Materials and Structures, 1997. **30**(6): p. 329.

77. Powers, T.C., *Mechanisms of Shrinkage and Reversible Creep of Hardened Cement Paste*. Conference Proceedings The Structure of Concrete, 1965.
78. Brochard, L., M. Vandamme, and R.J.M. Pellenq, *Poromechanics of microporous media*. Journal of the Mechanics and Physics of Solids, 2012. **60**(4): p. 606-622.
79. Vandamme, M., P. Dangla, S. Nikoosokhan, and L. Brochard, *Modeling the Poromechanical Behavior of Microporous and Mesoporous Solids: Application to Coal*, in *Nonlinear Elasticity and Hysteresis*. 2014. p. 105-126.
80. Luan, Y. and T. Ishida, *Enhanced Shrinkage Model Based on Early Age Hydration and Moisture Status in Pore Structure*. Journal of Advanced Concrete Technology, 2013. **11**(12): p. 360-373.
81. Nguyen, H., S. Rahimi-Aghdam, and Z.P. Bažant, *Unsaturated nanoporomechanics*. Proceedings of the National Academy of Sciences, 2020. **117**(7): p. 3440-3445.
82. Bishop, A.W., *The effective stress principle*. Teknisk Ukeblad 39, 1959: p. 859-863.
83. Christensen, R.M., *Mechanics of Composite Materials*. Wiley-Interscience, New York,, 1979.
84. Christensen, R.M. and K.H. Lo, *Solutions for effective shear properties in three phase sphere and cylinder models*. Journal of the Mechanics and Physics of Solids, 1979. **27**(4): p. 315-330.
85. Biot, M.A., *Theory of Elasticity and Consolidation for a Porous Anisotropic Solid*. Journal of Applied Physics, 1955. **26**(2): p. 182-185.
86. Bangham, D.H. and R.I. Razouk, *The wetting of charcoal and the nature of the adsorbed phase formed from saturated vapours*. Transactions of the Faraday Society, 1937. **33**(0): p. 1463-1472.
87. Hashin, Z., *Elastic moduli of heterogeneous materials*. Appl. Mech, 1962. **29**: p. 143–150.
88. Z. Hashin and S. Shtrikman, *A variational approach to the theory of the elastic behavior of multiphase materials*. J. Mech. Phys. Solids 1963. **11** p. 127–140.
89. POWERS, T.C., *The thermodynamics of volume change and creep*. Matériaux et Construction, 1968. **1**(6): p. 487–507.
90. Powers, T.C. and T.L. Brownyard, *Studies of the Physical Properties of Hardened Portland Cement Paste*. ACI Journal Proceedings. **43**(9).
91. Feldman, R.F. and P.J. SEREDA, *Sorption of water on compacts of bottle-hydrated cement. I. The sorption and length-change isotherms*. Journal of Applied Chemistry **14**(2): p. 87 - 93.
92. Feldman, R.F. and P.J. SEREDA, *SORPTION OF WATER ON COMPACTS OF BOTTLE-HYDRATED CEMENT. II\* THERMODYNAMIC CONSIDERATIONS AND THEORY OF VOLUME CHANGE*. Journal of app Chem., February, 1964. **14**(2): p. 93-98.
93. HANSEN, W., *Drying Shrinkage Mechanisms in Portland Cement Paste*. Journal of the American Ceramic Society, 1987. **70**(5): p. 323-328.
94. Churaev, N.V., *The Relation between Colloid Stability and Wetting*. Journal of Colloid and Interface Science, 1995. **172**(2): p. 479-484.
95. Derjaguin, B.V., N.V. Churaev, and V.M. Muller, *Surface Forces*. Springer, Boston, MA, 1987.

96. Biot, M.A., *General Theory of Three-Dimensional Consolidation*. Journal of Applied Physics, 1941. **12**(2): p. 155-164.
97. Jennings, J.E.B. and J.B. Burland, *Limitations to the Use of Effective Stresses in Partly Saturated Soils*. Géotechnique, 1962. **12**(2): p. 125-144.
98. Nuth, M. and L. Laloui, *Effective stress concept in unsaturated soils: Clarification and validation of a unified framework*. International Journal for Numerical and Analytical Methods in Geomechanics, 2008. **32**(7): p. 771-801.
99. Mateusz Wyrzykowski, C.D.B., Pietro Lura, *Prediction of Drying Shrinkage of Cement-Based Mortars with Poroelastic Approaches - A Critical Review* Sixth Biot Conference on Poromechanics, Paris, France 2017. **6**: p. 579-586.
100. Maruyama, I., *Origin of Drying Shrinkage of Hardened Cement Paste: Hydration Pressure*. Journal of Advanced Concrete Technology 2010. **Vol. 8**(2): p. 187-200.
101. Ipppei Maruyama, Yukiko Nishioka, Go Igarashi, and K. Matsui, *Microstructural and bulk property changes in hardened cement paste during the first drying process*. Cement and Concrete Research, 2014. **58**: p. 20–34.
102. Jennings, H.M., *Refinements to colloid model of C-S-H in cement: CM-II*. Cement and Concrete Research, 2008. **38**: p. 275–289.
103. P. Acker, *Micromechanical analysis of creep and shrinkage mechanisms*. Creep, Shrinkage and Durability Mechanics of Concrete and other quasi-brittle Materials, 2001: p. 15-25.
104. Jennings, H.M., *A model for the microstructure of calcium silicate hydrate in cement paste*. Cement and Concrete Research, 2000. **30**: p. 101-116.
105. Hamlin M. Jennings, Aditya Kumar, and GauravSant, *Quantitative discrimination of the nano-pore-structure of cement paste during drying: New insights from water sorption isotherms*. Cement and Concrete Research 2015. **76**: p. 27-36.
106. Ipppei Maruyama, Yukiko Nishioka, Go Igarashi, and Kunio Matsui, *Microstructural and bulk property changes in hardened cement paste during the first drying process*. Cement and Concrete Research, 2014. **58**: p. 20-34.
107. Ipppei Maruyama, Naoki Sakamoto, Kunio Matsui, and Go Igarashid, *Microstructural changes in white Portland cement paste under the first drying process evaluated by WAXS, SAXS, and USAXS*. Cement and Concrete Research, 2017. **91**: p. 24-32.
108. Babaei, S., S. Seetharam, U. Muehlich, L. Areias, G. Steenackers, and B. Craeye, *Modeling of drying shrinkage in concrete : a multiscale poromechanics approach*, in *Symposium on Concrete Modelling : CONMOD2018, 26-29 August, 2018, Delft, the Netherlands*. 2018, RILEM Publications. p. 165-169.
109. Vlahinić, I., H.M. Jennings, J.E. Andrade, and J.J. Thomas, *A novel and general form of effective stress in a partially saturated porous material: The influence of microstructure*. Mechanics of Materials, 2011. **43**(1): p. 25-35.
110. Phung, Q.T., N. Maes, G. De Schutter, D. Jacques, and G. Ye, *Determination of water permeability of cementitious materials using a controlled constant flow method*. Construction and Building Materials, 2013. **47**: p. 1488-1496.
111. Zhang, Z., M. Thiery, and V. Baroghel-Bouny, *Investigation of moisture transport properties of cementitious materials*. Cement and Concrete Research, 2016. **89**: p. 257-268.

112. Kumar, A., S. Ketel, K. Vance, T. Oey, N. Neithalath, and G. Sant, *Water Vapor Sorption in Cementitious Materials—Measurement, Modeling and Interpretation*. *Transport in Porous Media*, 2014. **103**(1): p. 69-98.
113. Xiong, Q., T.G. Baychev, and A.P. Jivkov, *Review of pore network modelling of porous media: Experimental characterisations, network constructions and applications to reactive transport*. *Journal of Contaminant Hydrology*, 2016. **192**: p. 101-117.
114. Zhang, Z. and G. Scherer, *Determination of water permeability for cementitious materials with minimized batch effect*. *Construction and Building Materials*, 2018. **191**: p. 193–205.
115. Kozeny, J., *Über kapillare Leitung des wassers in Böden*. *Sitzungsberichte der Kaiserlichen Akademie der Wissenschaften*, 1927. **136**: p. 271-306.
116. Carman, P.C., *Fluid flow through granular beds*. *Chemical Engineering Research and Design*, 1997. **75**: p. S32-S48.
117. Katz, A.J. and A.H. Thompson, *Quantitative prediction of permeability in porous rock*. *Physical Review B*, 1986. **34**(11): p. 8179-8181.
118. Ye, G., P. Lura, and K. van Breugel, *Modelling of water permeability in cementitious materials*. *Materials and Structures*, 2006. **39**(9): p. 877-885.
119. Zalzale, M., P.J. McDonald, and K.L. Scrivener, *A 3D lattice Boltzmann effective media study: understanding the role of C-S-H and water saturation on the permeability of cement paste*. *Modelling and Simulation in Materials Science and Engineering*, 2013. **21**(8).
120. Li, K., P. Stroeven, and N.L.B. Le, *methodology for porosimetry in virtual cementitious composites to economically and reliably estimate permeability*. *Image Analysis & Stereology; Vol 34, No 2 (2015)*, 2015.
121. Li, K., *Numerical Determination of Permeability in Unsaturated Cementitious Materials*. 2017, TU Delft: TU Delft.
122. Grasley, Z.C., G.W. Scherer, D.A. Lange, and J.J. Valenza, *Dynamic pressurization method for measuring permeability and modulus: II. cementitious materials*. *Materials and Structures*, 2007. **40**(7): p. 711-721.
123. Ai, H., J.F. Young, and G.W. Scherer, *Thermal Expansion Kinetics: Method to Measure Permeability of Cementitious Materials: II, Application to Hardened Cement Pastes*. *Journal of the American Ceramic Society*, 2001. **84**(2): p. 385-91.
124. Ye, G., *Percolation of capillary pores in hardening cement pastes*. *Cement and Concrete Research*, 2005. **35**(1): p. 167-176.
125. Zamani, S., R.M. Kowalczyk, and P.J. McDonald, *The relative humidity dependence of the permeability of cement paste measured using GARField NMR profiling*. *Cement and Concrete Research*, 2014. **57**: p. 88-94.
126. Egan, G., Aditya Kumar, Narayanan Neithalath, and G. Sant, *Re-examining the influence of the inclusion characteristics on the drying shrinkage of cementitious composites*. *Construction and Building Materials*, 2017. **146**: p. 713–722.
127. Akbari, M., D. Sinton, and M. Bahrami, *Viscous flow in variable cross-section microchannels of arbitrary shapes*. *International Journal of Heat and Mass Transfer*, 2011. **54**(17): p. 3970-3978.

128. Goto, S. and D.M. Roy, *The effect of w/c ratio and curing temperature on the permeability of hardened cement paste*. Cement and Concrete Research, 1981. **11**(4): p. 575-579.
129. van Genuchten, M.T., *A Closed-form Equation for Predicting the Hydraulic Conductivity of Unsaturated Soils*. Soil Science Society of America Journal, 1980. **44**(5): p. 892-898.
130. V. Baroghel-Bouny, *Water vapour sorption experiments on hardened cementitious materials: Part I: Essential tool for analysis of hygral behaviour and its relation to pore structure*. Cement and Concrete Research, 2007. **37**(3): p. 414-437.
131. Scrivener, K.L., V.M. John, and E.M. Gartner, *Eco-efficient cements: Potential economically viable solutions for a low-CO2 cement-based materials industry*. Cement and Concrete Research, 2018. **114**: p. 2-26.
132. Wilson, W., L. Sorelli, and A. Tagnit-Hamou, *Unveiling micro-chemo-mechanical properties of C-(A)-S-H and other phases in blended-cement pastes*. Cement and Concrete Research, 2018. **107**: p. 317-336.
133. Smilauer, V. and Z.k. Bittnar, *Microstructure-based micromechanical prediction of elastic properties in hydrating cement paste*. Cement and Concrete Research, 2006. **36**(9): p. 1708-1718.
134. Lin Liu a, b., †, Xuecheng Wang a, Huisu Chen c, Chaojun Wand, *Microstructure-based modelling of drying shrinkage and microcracking of cement paste at high relative humidity*. Construction and Building Materials, 2016.
135. Hain, M. and P. Wriggers, *Computational homogenization of micro-structural damage due to frost in hardened cement paste*. Finite Elements in Analysis and Design, 2008. **44**(5): p. 233-244.
136. Wriggers, P. and M. Hain. *Micro-Meso-Macro Modelling of Composite Materials*. in *III European Conference on Computational Mechanics*. 2006. Dordrecht: Springer Netherlands.
137. Bernard, F., S. Kamali-Bernard, and W. Prince, *3D multi-scale modelling of mechanical behaviour of sound and leached mortar*. Cement and Concrete Research, 2008. **38**(4): p. 449-458.
138. CEA, <http://www-cast3m.cea.fr/>, Cast3M 2019 ©
139. Maruyama, I., A. Teramoto, and G. Igarashi, *Strain and thermal expansion coefficients of various cement pastes during hydration at early ages*. Materials and Structures, 2014. **47**(1): p. 27-37.
140. Maruyama, I. and G. Igarashi, *Cement Reaction and Resultant Physical Properties of Cement Paste*. Journal of Advanced Concrete Technology, 2014. **12**(6): p. 200-213.
141. Zhang, M., *Microstructure-informed modelling of damage evolution in cement paste*. 2014.
142. Michal Hlobil, V.S., Gilles Chanvillard, *Micromechanical multiscale fracture model for compressive strength of blended cement pastes*. Cement and Concrete Research 2016. **83** (2016) p. 188–202.
143. Honorio, T., L. Brochard, and B. Bary, *Statistical variability of mechanical fields in thermo-poro-elasticity: Multiscale analytical estimations applied to*

- cement-based materials at early-age*. Cement and Concrete Research, 2018. **110**: p. 24-41.
144. Pichler, B., C. Hellmich, J. Eberhardsteiner, J. Wasserbauer, P. Termkhajornkit, R. Barbarulo, and G. Chanvillard, *The Counteracting Effects of Capillary Porosity and of Unhydrated Clinker Grains on the Macroscopic Strength of Hydrating Cement Paste*; *A Multiscale Model*, in *Mechanics and Physics of Creep, Shrinkage, and Durability of Concrete*. 2013. p. 40-47.
  145. Ferraris, C.F. and F.H. Wittmann, *Shrinkage mechanisms of hardened cement paste*. Cement and Concrete Research, 1987. **17**(3): p. 453-464.
  146. Bazant, Z.P. and J.C. Chern, *Concrete creep at variable humidity: constitutive law and mechanism*. Materials and Structures, 1985. **18**(1): p. 1.
  147. Němeček, J., V. Králík, V. Šmilauer, L. Polívka, and A. Jäger, *Tensile strength of hydrated cement paste phases assessed by micro-bending tests and nanoindentation*. Cement and Concrete Composites, 2016. **73**: p. 164-173.
  148. Shahrin, R. and C.P. Bobko, *Characterizing Strength and Failure of Calcium Silicate Hydrate Aggregates in Cement Paste under Micropillar Compression*. Journal of Nanomechanics and Micromechanics, 2017. **7**(4): p. 06017002.
  149. Qian, Z., *Multiscale Modeling of Fracture Processes in Cementitious Materials*, in *None (EN)*. 2012, Haveka B.V.
  150. Zhang, M. and A.P. Jivkov, *Microstructure-informed modelling of damage evolution in cement paste*. Construction and Building Materials, 2014. **66**: p. 731-742.
  151. Zhang, M. and A.P. Jivkov, *Micromechanical modelling of deformation and fracture of hydrating cement paste using X-ray computed tomography characterisation*. Composites Part B: Engineering, 2016. **88**: p. 64-72.
  152. Luković, M., E. Schlangen, and G. Ye, *Combined experimental and numerical study of fracture behaviour of cement paste at the microlevel*. Cement and Concrete Research, 2015. **73**: p. 123-135.
  153. Han, T.-S., X. Zhang, J.-S. Kim, S.-Y. Chung, J.-H. Lim, and C. Linder, *Area of lineal-path function for describing the pore microstructures of cement paste and their relations to the mechanical properties simulated from  $\mu$ -CT microstructures*. Cement and Concrete Composites, 2018. **89**: p. 1-17.
  154. Kinet, D., K. Chah, A. Gusarov, A. Faustov, L. Areias, I. Troullinos, P.V. Marcke, B. Craeye, E. Coppens, D. Raymaekers, and P. Mégret, *Proof of Concept for Temperature and Strain Measurements With Fiber Bragg Gratings Embedded in Supercontainers Designed for Nuclear Waste Storage*. IEEE Transactions on Nuclear Science, 2016. **63**(3): p. 1955-1962.
  155. Iliopoulos, S., D.G. Aggelis, L. Pyl, J. Vantomme, P. Van Marcke, E. Coppens, and L. Areias, *Detection and evaluation of cracks in the concrete buffer of the Belgian Nuclear Waste container using combined NDT techniques*. Construction and Building Materials, 2015. **78**: p. 369-378.
  156. Chen, W., *A fully coupled thermo-hydro-mechanical model for unsaturated porous media* 2009.
  157. Gasch, T., *Concrete as a multi-physical material with applications to hydro power facilities*, in *TRITA-BKN. Bulletin*. 2016, KTH Royal Institute of Technology: Stockholm. p. xii, 131.

158. Maekawa, K., T. Ishida, and T. Kishi, *Multi-scale Modeling of Concrete Performance* Journal of Advanced Concrete Technology, 2003. **1**(2): p. 91-126.
159. Maekawa, K., T. Ishida, and T. Kishi, *Multi-Scale Modeling of Structural Concrete*. 2008: Taylor & Francis.
160. Chhun, P., *Modélisation du comportement thermo-hydro-chemo-mécanique des enceintes de confinement nucléaire en béton armé-précontraint*. 2017.
161. Chhun, P., L. Buffo-Lacarrière, and A. Sellier, *Material and Geometric Heterogeneity Consideration for Cracking Risk Prediction of Young Age Behavior of Experimental Massive Reinforced Concrete Structure*. Key Engineering Materials, 2016. **711**: p. 900-907.
162. Craeye, B., G. De Schutter, L. Areias, W. Wacquier, H. Van Humbeeck, and A. Van Cotthem, *Validation of the early-age thermo-mechanical behaviour of SCC Supercontainers for the disposal of High Level radioactive Waste*, X.L. Li, Editor. 2011: United States. p. 851-861.
163. Mazars, J. and G. Pijaudier-Cabot, *Continuum Damage Theory; Application to Concrete*. Journal of Engineering Mechanics, 1989. **115**(2): p. 345-365.
164. Pijaudier-Cabot, G. and J. Mazars, *Damage Models for Concrete*, in *Handbook of Materials Behavior Models*, L. Jean, Editor. 2001, Elsevier. p. 500-512.
165. beton, F.i.d., *Fib Model Code for Concrete Structures 2010*. 2013: Ernst & Sohn, a Wiley brand.
166. Areias, L., T. Geernaert, S. Sulejmani, F. Berghmans, G. Luyckx, K. Chah, I. Troullinos, E. Coppens, P. Van Marcke, D. Raymaekers, and B. Craeye, *Temperature and strain measurements in concrete using micro-structure optical fiber sensors*. International Symposium Non-Destructive Testing in Civil Engineering (NDT-CE), September 15-17, 2015, Berlin, Germany. 2015.
167. Craeye, B., L. Areias, M. Van Geet, and S. Babaei. *Revised Macro-cracking Criterion for Massive Non-reinforced Self-compacting Concrete Structures Under Thermal Load Based on Extensive Experimental Testing and Field Observations*. in *Rheology and Processing of Construction Materials*. 2020. Cham: Springer International Publishing.
168. Roland J.-M. Pellenq, Akihiro Kushima, Rouzbeh Shahsavari, Krystyn J. Van Vliet, Markus J. Buehler, Sidney Yip, and F.-J. Ulm, *A realistic molecular model of cement hydrates*. PNAS, 2009.

The principal objective of this study is to investigate the Thermo-Hydro-Mechanical (THM) behavior of concrete within a multiscale framework. More importantly, to be able to predict fundamental properties of concrete based on its composition to enable optimization of its design. This, however, cannot be achieved without an in-depth study of phenomena and parameters, which are affecting the macro-behavior of the concrete. Since cementitious engineered barriers are exposed to thermal loading, a range of coupled processes usually referred to as THM processes are involved in their performance. Therefore, this thesis proposes a stepwise, multi-component and multiscale framework to model THM behavior of cementitious materials.